Institute for Experimental Medical Research, Oslo University Hospital Ullevål
KG Jebsen Cardiac Research Center, University of Oslo
Center for Heart Failure Research, University of Oslo

Measuring in vivo Regional Myocardial Function Using High-Field MRI

Development and application of high-resolution MR imaging of the beating heart

Emil Knut Stenersen Espe
Dissertation for the degree Philosophiae Doctor (Ph.D.)
University of Oslo
2014

Series of dissertations submitted to the
Faculty of Medicine, University of Oslo
No. 1800

ISBN 978-82-8264-889-9

Cover: Inger Sandved Anfinsen.
Printed in Norway: AIT Oslo AS.

Produced in co-operation with Akademika Publishing.
The thesis is produced by Akademika Publishing merely in connection with the thesis defence. Kindly direct all inquiries regarding the thesis to the copyright holder or the unit which grants the doctorate.

ACKNOWLEDGEMENTS

The work presented in this thesis was done in 2010-2014 at the Institute for Experimental Medical Research (IEMR) at Oslo University Hospital Ullevål and University of Oslo. The work was done in collaboration with Department of Cardiovascular Medicine (University of Oxford, UK), Institutt for kirurgisk forskning (OUS Rikshospitalet), Center for Cardiological Innovation, (OUS/UiO), Department of Cardiology (OUS Rikshospitalet); Bjørknes College and Department of Thoracic Surgery (OUS Ullevål).

First and foremost, I wish to express my deepest gratitude to my main supervisor, Prof. Ivar Sjaastad, and to my co-supervisors PhD Lili Zhang and Prof. Ole M. Sejersted. As my main supervisor, I think it is impossible to overestimate the importance of Ivar's daily guidance during my PhD period. He possesses a vast bank of knowledge, and no matter whether tasks, small or large, are apparently straightforward or seemingly impossible, he never ceases to be positive and constructive. I am fascinated by his energy and ability to stay optimistic and realistic at the same time, and very thankful for the trust he has shown me. Furthermore, without our treasured "MR-wizard" Lili I would be very much lost in the rocky landscape of magnetic resonance (MR). She continues to impress with her deep theoretical and technical understanding of the system, and has been an important guide in the overwhelming scenery that is MR. Also, the overview and long-term guidance provided by Ole has been of great importance in my work. He retains a unique ability to combine his responsibility as head of IEMR with a keen eye for the details in the individual projects and an encouraging spirit. He continues to be an inspiration.

The present work is utterly a result of a combined effort. I am very grateful for the profound contributions from my colleagues at the MR facility; Kristine, Solveig and Vidar. In addition to having provided many interesting and fruitful discussions and important reflections, they generate the nicest social working environment anyone might ask for. Moreover, Magnus has been of great importance to me with both scientifically and socially, and I've enjoyed and learned a lot from our discussions. I am very thankful for all his help, although he continues to beat me at chess…

Overall, the unique working environment at IEMR is recognized by its skillful people with a large variety of backgrounds creating a truly synergic cross-discipline setting. I am very thankful to each and every one of my colleagues for contributing to the including atmosphere that recognizes IEMR. Special thanks to Michael, Bill, Åsmund, Biljana, Vigdis, Tore, Kristin and Guro with whom I've had the pleasure of working especially close with. Furthermore, I've enjoyed sharing offices with Ståle, Mathis, Nils, Pim, Karina, Ravinea, Tandekile, Terje and Jonas over the years, oftentimes resulting in unexpected and important discussions. Lisbeth, Jo-Ann and Ulla are instrumental and do a marvelous work in ensuring that IEMR continues to be a smooth-running machine. Per Andreas and Vidar provides unmatched expertise in making sure that everything communicating with ones and zeroes works properly. How they continue to do that every day, with a smile, is beyond me and nothing short of amazing. Roy's skills in the technical department have also been of great importance to me and I am very thankful for his help.

Without the highly competent staff at the animal care facility, nothing of this work would be possible. I am very thankful for their continuous efforts for providing a safe and well-organized facility.

In the final stages of my PhD period, the crucial contributions of Dr. Morten Eriksen, Prof. Thor Edvardsen and Prof. Otto A. Smiseth at OUS Rikshospitalet have been very much treasured. In the last project, their roles were vital. Especially, my (nearly) daily contact with Morten in this stage has been of great importance to me, and he continues to baffle me with his seemingly never-ending knowledge.

I would also like to emphasize the important contributions from Dr. Jürgen Schneider at the University of Oxford, who is one of the primary authorities in the world on preclinical MR. He has provided insightful and constructive feedback throughout my work with this thesis. I am deeply thankful for his engagement.

Last but not the bit least, I wish to express my gratitude to my friends and family. I am very thankful for the love and support I have received from my parents, Bente and Erik. You have always been there for me! Also, my siblings Morten, Stine and Asbjørn and sister-in-law Ann-Marit, my sweet grandmothers Bjørg and Gudrun, and my family-in-law Maj-Britt, Trond, Elin, Ingrid, Magne and Karl all have stayed supportive and interested. One could not wish for a better family; you all mean a lot to me. On that note, I wish to emphasize the deep imprints on my life made by my late grandfathers, Erling and Ivar. They were always caring, supportive and involved. I miss you both deeply.

Throughout and after my studies at the Department of Physics at UiO, I've treasured my friendship with Erlend. We have shared ups and downs all the way from the somewhat murky Sophus Lie's auditorium to the friendly corridors of the Biophysics group; and continue to share a common fascination for intricate medical equipment. Also, I wish to emphasize my good friend Ole, who has been my closest friend for over 10 years, and with whom I've probably had the most surprising, fascinating and meaningful discussions there ever was. Although there unfortunately can be a while between us seeing each other, I hold our friendship very high.

•

Finally, words cannot describe the importance to me of my lovely wife Sigrun and adorable sons Erlend Markus and Sebastian, who constitute the very fundament of my existence and keep reminding me of what *really* matters in life. For that, I will forever be grateful.

Emil Knut Stenersen Espe,
Ås, May 2014

SUPPORTED BY

Institute for Experimental Medical Research
South-Eastern Norwegian Regional Health Authority
Oslo University Hospital Ullevål
University of Oslo
The Research Council of Norway
KG Jebsen Cardiac Research Center
Center for Heart Failure Research
Anders Jahre's Fund for the Promotion of Science
Familien Blix' fond til fremme av medisinsk forskning

TABLE OF CONTENTS

ABBREVIATIONS

2D-STE	2D speckle-tracking echocardiography
ANOVA	Analysis of variance
BP	Blood pressure
$cRMW_L$	Circumferential regional myocardial work per unit (through-plane/long-axis) length
$cRMW_S$	Circumferential regional myocardial work per unit surface
CT	Computed tomography
DENSE	Displacement encoding with stimulated echos
ECC	Eddy current compensation
ECG	Electrocardiography
ECHO	Echocardiography/Ultrasound
EF	Ejection fraction
HARP	Harmonic phase
HF	Heart failure
LCA	Left coronary artery
LV	Left ventricle
LVP	LV intraventricular pressure
MI	Myocardial infarction
MR	Magnetic resonance
MRI	Magnetic resonance imaging
NA	Number of averages (signal averaging)
PC-MRI	Phase contrast magnetic resonance imaging
PET	Positron emission tomography
RF	Radio frequency
RV	Right ventricle
SA	Short axis
SENC MRI	Strain encoded MRI
SNR	Signal-to-noise ratio
SPECT	Single-photon emission computed tomography
SV	Stroke volume
TDI	Tissue Doppler imaging
TE	MR echo time
TR	MR repetition time
VIPR	Vastly undersampled isotropic-voxel radial projection imaging

1 List of Papers in Thesis

Paper I

Improved MR phase contrast velocimetry utilizing a novel nine-point balanced motion encoding scheme with increased robustness to eddy current effects

Emil K. S. Espe, Jan Magnus Aronsen, Biljana Skrbic, Vidar Magne Skulberg, Jürgen E. Schneider, Ole M. Sejersted, Lili Zhang, Ivar Sjaastad

Magn Res Med 2013;69:48-61

Paper II

Unwrapping eddy current compensation: Improved compensation of eddy current induced baseline shifts in high-resolution phase-contrast MRI at 9.4 T

Emil K. S. Espe, Lili Zhang, Ivar Sjaastad

Magn Res Med (In press; doi: 10.1002/mrm.25023)

Paper III

Novel insight into the detailed myocardial motion and deformation of the rodent heart using high-resolution phase contrast MRI

Emil K. S. Espe, Jan Magnus Aronsen, Kristine Skårdal, Jürgen E. Schneider, Lili Zhang, Ivar Sjaastad

J Cardiovasc Magn Reson 2013;15:82

Paper IV

Assessment of regional myocardial work in rats

Emil K. S. Espe, Jan Magnus Aronsen, Guro Søe Eriksen, Lili Zhang, Otto A. Smiseth, Thor Edvardsen, Ivar Sjaastad, Morten Eriksen

Submitted

2 SUMMARY

Heart failure (HF) is one of the major causes of mortality in the Western world, recognized by a compromised ability of the heart to supply the body with blood. The poor understanding of the disease mechanisms and lack of adequate therapy strategies are reflected in the grim prognosis of HF.

Great research efforts over the last decades have been aimed at revealing the factors responsible for the reduction in function the left ventricle (LV) of the heart. In this, small-animal models of cardiac disease plays an irreplaceable role, enabling isolation and identification of structural and functional alterations on cellular and/or subcellular level. However, to be able to relate findings on the microscopic scale to alterations in cardiac function, there is a great need for methodology, preferably noninvasive, that allows detailed assessment of in vivo regional myocardial function.

The hearts of mice and rats are more than two orders of magnitudes smaller than human hearts by weight, and beats up to ten times faster. Measurement of cardiac function in mice and rats thus understandably requires considerably higher resolution than in humans to offer comparable data yield.

Phase contrast magnetic resonance imaging (PC-MRI) is a well-established and versatile noninvasive imaging technique allowing measurement of time-resolved 3D motion. We have developed an improved PC-MRI technique able to measure myocardial motion in small animals with improved accuracy and resolution compared to earlier approaches (**Paper I**). A major consequence of pushing the limits of achievable spatiotemporal resolution in PC-MRI is increased generation of eddy currents in the systems, which introduces severe baseline shifts in the measured motion that may render the data unusable. This required further development of eddy current correction techniques (**Paper II**). We developed this imaging technique further and introduced and validated a protocol for calculating regional myocardial strain from PC-MRI velocity data. We applied this protocol, as a proof-of-concept, in normal and regionally dysfunctional rat hearts (**Paper III**). Finally, we incorporated a mathematical model allowing calculation of regional myocardial work from PC-MRI data, in combination with identification of the mitral and aortic valve events and a simple measurement of peak blood pressure. This protocol was also demonstrated in normal and dysfunctional rat hearts (**Paper IV**).

The work in this thesis demonstrates that PC-MRI allows noninvasive measurement of regional myocardial motion, strain and work in small-animal models of cardiac disease with high resolution. The results are readily extendable to human applications, ultimately allowing higher sensitivity and/or resolution and extended data yield in functional cardiac MRI.

3 INTRODUCTION

3.1 MYOCARDIAL MECHANICS

The most fundamental task of the heart is to circulate blood throughout the body. This is achieved through regular contraction of its ventricles, which involves a complex combined effort of thickening of the ventricular wall, decrease in circumference, shortening of the ventricles combined with a characteristic twisting motion of the whole organ. Evidently, contraction of the ventricles is a result of an intricate three-dimensional deformation of the muscle (1).

3.1.1 GLOBAL AND REGIONAL MECHANICAL FUNCTION

The mechanical *function* of the myocardium refers to its ability to consistently and properly contract and relax. Its basic mechanical function, both globally and regionally, is reflected in the three-dimensional pattern of ventricular motion and strain (2).

The **global cardiac function** is reflected in parameters like stroke volume (the volume ejected from the ventricle per cardiac cycle) and ejection fraction (the fraction of the total ventricular blood pool ejected per cardiac cycle). On the other hand, **regional myocardial function** involves motion, displacement, stress, strain, and force and energy usage in smaller regions of the myocardium (Figure 3.1). Regional function is determined by numerous factors; including local contractility and material properties as well as global aspects such as intraventricular pressure (3).

3.1.2 MOTION, DEFORMATION AND WORK

The **motion** or **velocity** of the myocardium (displacement per unit time) is a marker for both ventricular contractility and its ability to relax. The difference in displacement between two points represents a local stretch or compression, collectively referred to as **deformation** or **strain**[1] (Figure 3.2).

Even though mechanical parameters such as velocity, displacement or strain do provide important information of cardiac behavior and changes over time, it does not provide an adequate measure of myocardial work or oxygen/energy consumption since these factors are load dependent (4, 5). Methodology able to measure the actual physical **work** performed by the myocardium would thus convey more comprehensive information of myocardial function, as several studies have suggested that analysis of cardiac work provides significant insight into LV remodeling and dysfunction in general (6-8).

3.1.3 THE NORMAL HEART

The heart consists of two main chambers; the ventricles. During the ejection phase, the right and left ventricles contract and eject blood to the pulmonary and systemic circulation, respectively. The right ventricle (RV) pumps deoxygenated blood into the pulmonary circulation through the pulmonary valve, and the LV ejects oxygen-rich blood into the aorta and the systemic circulation through the aortic valve. During the filling phase, the right ventricle is filled with blood from the systemic circulation via

[1] Likewise, spatial difference in velocity represents the *rate* of change in strain, namely **strain rate**.

the right atrium through the tricuspid valve, and the LV receives oxygen-rich blood from the lungs via the left atrium through the mitral valve.

In this work, we will focus on the function of the left ventricle, responsible for providing the body with oxygenated blood.

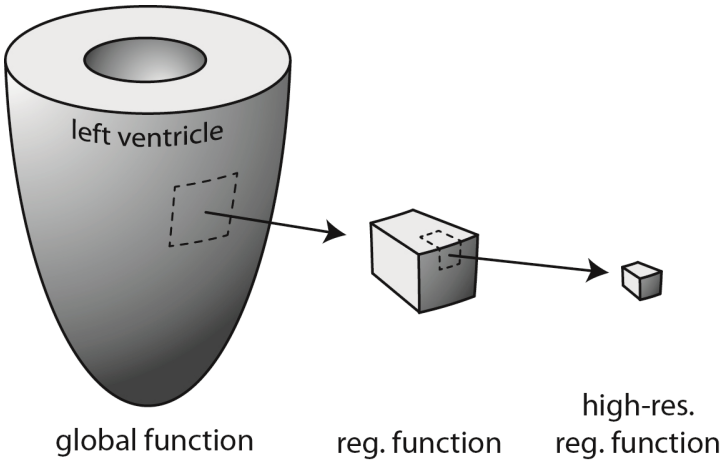

Figure 3.1 Global and regional function of the left ventricle
Global function refers to the properties of the ventricle as a whole. Examples of global functional parameters are stroke volume, stroke work and ejection fraction. **Regional function**, on the other hand, considers the properties of smaller regions of the myocardium with different degree of detail. Examples of regional functional parameters are regional velocity, displacement, deformation and work. While global function reflects the cardiac function as a whole, analysis of regional function has the ability to reveal for instance small-scale contractile dysfunction that might be masked on a global scale due to compensatory mechanisms.

The Cardiac Cycle

Shortly after its electrical activation (measureable by electrocardiography, ECG), the left ventricle starts to contract and the mitral valve closes (which creates the first acoustic heart tone). At this time, the pressure in the LV (LVP) is lower than the pressure in the aorta, both valves are closed and no blood leaves or enters the ventricle. This is the **isovolumic contraction phase**. As soon as the contraction of the LV has increased LVP to be higher than the pressure in the aorta, the aortic valve opens and blood flows from the LV into the aorta. This is the **ejection phase**. As the blood is ejected, the volume of the LV decreases and contraction completes, and LVP ultimately decreases. This causes the aortic valve to close (this creates the second heart tone), and the ventricle enters the **isovolumic relaxation phase**. As LVP falls below the atrial pressure, the mitral valve opens and blood flows from the left atrium to the LV. This is the **filling phase**.

There are different definitions of systole and diastole, but for our purposes, we shall define systole as the time between mitral valve closure and aortic valve closure (isovolumic contraction + ejection phase), and diastole as the time between aortic valve closure and mitral valve closure (isovolumic relaxation + filling phase).

Normal Cardiac Mechanics

On the cellular level, a fine-tuned process (in which Ca^{2+} ions plays a central role) converts an electrical depolarization of the cellular membrane to contraction of the cell. Regional function is related to the functionality of the cardiomyocytes in a limited region. A sophisticated network of conductive fibers throughout the heart ensures, under normal circumstances, optimal distribution of the electrical activation resulting in a well-synchronized contraction of the ventricles.

A healthy LV ejects about 60% of its content during each heartbeat. Although the whole LV myocardium contributes to the contraction, even healthy hearts exhibit regional heterogeneity in contraction (2, 9-13). Therefore, to be able to detect and quantify local perturbation in function in a given heart, it must be compared with the normal range of that region (2, 12).

The pumping performance of the ventricles are affected by, among other factors, the mechanical properties of the myocardium (14). The pronounced deformation of the heart during the cardiac cycle is due to active contraction of the cardiomyocytes along muscle fibers, and their relaxation (15). In the human heart, the ejection of blood is primarily achieved by radial inward motion and a descend of the base towards the apex (2). Contraction is typically greatest in the anterior and lateral walls (2, 13), is increasing towards the base (13), and has been shown to have been shown to decrease with age (1). Peak velocity in the endocardium exceeds the velocities in the epicardium, creating a transmural velocity gradient (1).

In this thesis, the hearts of mice and rats will serve as models for human cardiac disease. Despite considerable difference in dimensions and beating frequency, the hearts of small animals share many fundamental cardiac mechanical properties with their human counterpart, and the models have distinct transferrable value to human conditions (17). Several studies have evaluated LV function in small animals and found that the hearts in humans, rat and mice share many of the same properties, such as EF, intramyocardial strain and twist (18-20).

3.2 HEART FAILURE

Disruption in contractile function of the heart does, as expected, quickly evoke a serious problem. In heart failure, the ability of the heart to pump blood is compromised. HF is one of the major causes of death in the western world (21); no cure exists, and half of all patients die within 4 years of diagnosis (22). Its prevalence is increasing, and despite recent advances in HF therapy, mortality rate remains high.

In the last decades, a large research effort has been aiming at revealing the mechanisms responsible for reducing the contractility of the LV. While there is a general agreement that alterations on a sub-cellular level contribute to reduced pumping ability, the precise mechanisms for development of HF has yet to be described. The poor understanding of these mechanisms and lack of adequate therapies is reflected in the high morbidity and mortality.

Setting the tone for this thesis, there is a dire need for methodology able to increase the knowledge of disease mechanisms, as a better understanding of disease progression and the underlying driving factors could make HF a more manageable disease.

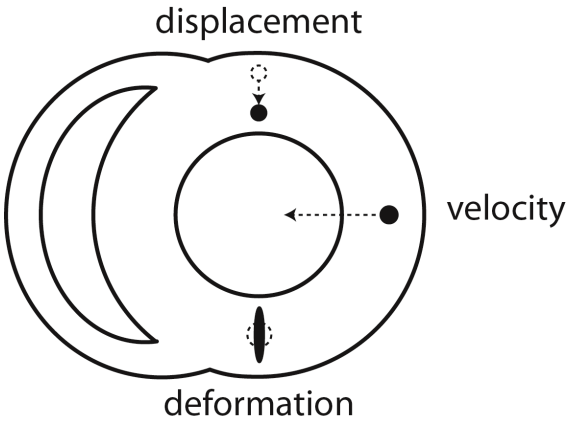

Figure 3.2 Three views on regional myocardial mechanics
Displacement is the distance travelled by individual material points over a certain time. **Velocity** is the rate of change in displacement, while **deformation** (strain) is identified as the spatial variation in displacement. See Figure 3.6 for the relationship between the formalisms. While mechanics and function oftentimes are equated, the notion that mechanical properties are load dependent and therefore does not reflect actual oxygen and energy consumption directly, is important. This cartoon is inspired by (16).

3.2.1 Evaluating Myocardial Function in Heart Failure

Research on HF may be done on several levels. Evaluation of **whole-heart (global) function** through classical parameters such as stroke volume (SV), myocardial mass and ejection fraction (EF) are widely acknowledged. However, although very well-established, the prognosis-predicting value of for instance EF in development of cardiovascular events has been disputed (23-25). Particularly, apparently normal properties on the whole-heart scale may mask early markers of cardiac pathology, such as alterations in **regional function**. Detailed knowledge of the complex motion of the healthy and diseased heart may lead to better understanding of disease progression and pathogenesis (21, 23). In ischemic heart disease, for example, even a small imbalance in oxygen supply leads to contractile dysfunction in the affected regions (26). On an even smaller scale, advanced **cellular techniques** allow comprehensive assessment of intracellular structure and function (e.g. t-tubules (27), Ca^{2+} homeostasis (28) and cellular contraction (29)).

By comparing findings on different levels, such as how localized cellular alterations manifest in regional and global function, novel insight into the mechanisms of HF may be gained. The work in this thesis focuses on methodology for evaluating

regional myocardial function, constituting the bridge between cellular and global function.

3.2.2 Animal Models in Heart Failure Research

For several decades, mice and rats have been a backbone of basal cardiovascular research (30), and are commonly used to study pathological processes on a structural, functional, metabolic and molecular level.

Rodents are attractive for comparative biomedical research due to small size, affordability and easier handling than larger animals (such as pigs) and its ability to model complex cardiac disorders. Advanced surgery techniques allow the creation of models representing for instance hypertension, aortic stenosis and myocardial infarction, and potential consequential heart failure (31-35). For example, the rat model on myocardial infarction (MI) has been shown to provide predictive value for cardiac remodeling after MI in humans (36, 37), and allows detailed monitoring of changes due to therapy or interventions (38).

Transgenic and knockout techniques models also provide a matchless opportunity to isolate the roles of individual components in cardiovascular development and cardiac disease (39-46). These approaches have advanced the understanding of the roles of individual genes and proteins considerably, both in normal cardiovascular development and in cardiac disease.

However, the vast majority of basal cardiovascular research relies on in vitro or invasive in vivo methods for phenotypic assessment (19). The accessibility of reliable, versatile noninvasive methods for quantification of in vivo physiology in experimental animals, such as regional myocardial mechanics and function (Figure 3.2), is therefore of great importance.

3.3 Methodology for Assessing Myocardial Function

A large library of techniques and protocols optimized for assessing global and regional myocardial function has been made available over the years. Continuous efforts are pushing the limits of available resolution, applicability, robustness, accuracy and availability.

There are two main approaches to assessing cardiac function. Evaluation of **global cardiac function** through parameters such as stroke volume and ejection fraction is the most widely used clinical evaluation tool for assessing cardiac health. These well-established parameters are well-standardized, known to have prognosis-predicting value and are relatively easily acquired. Assessing **regional myocardial function** refers to the evaluation of local properties of the myocardium, such as regional velocities, stretch, compression and energy usage. As noted above, the detection and quantification of disrupted regional function relies on comparison to the normal range of that region (2, 12).

Selected Methodology

Here, we present a selection of techniques allowing evaluation of myocardial function, culminating in comprehensive presentations of the two most widely applied

methods for noninvasive evaluation of cardiac function, both in clinically and in preclinical research; namely magnetic resonance imaging and echocardiography. A visual comparison of the techniques treated here is found in Figure 3.3.

Magnetic resonance imaging (MRI) is widely considered the gold standard for assessing cardiac morphology and physiology (23, 47-55). MRI is a noninvasive non-ionizing imaging modality; it relies solely on magnetic fields and radio waves, and the intrinsic properties of protons[2] experiencing a magnetic field. Protons are highly abundant in living tissue due to being the core of the hydrogen atom, which makes up 2/3 of a water molecule.

Echocardiography (ECHO), or ultrasound, is extensively used for assessing myocardial function due to its efficiency, availability and portability, as well as relatively low cost. ECHO provides 2D or 3D real-time imaging and data evaluation, and is able to do measurements with very high temporal resolution.

Sonomicrometry refers to a technique where the relative displacement between two physical crystals is measured. By implanting ultrasonic crystals in the myocardium, local one-dimensional strain is readily measured by connecting the crystals to a sonomicrometer (56). While this is a very robust and sensitive technique, it is invasive and only provides strain in one direction in a predefined region.

Cardiac **computed tomography (CT)** is an x-rays based technique with very good spatial resolution (57), especially advantageous in evaluating structural abnormalities contributing to the development of HF. Recent advances have enabled analysis of myocardial function (23, 58). A drawback of CT is the usage of ionizing radiation.

Single-photon emission computed tomography (SPECT) and positron emission tomography (PET) are **nuclear imaging techniques** where regional metabolism can be imaged, and may be employed to detect myocardial ischemia and viability. In patients with HF, myocardial perfusion imaging, evaluation of sympathetic innervations and characterization of molecular processes are the main clinical applications (57). Nuclear imaging techniques provide little anatomic information, and are therefore routinely combined with a supplemental imaging technique, such as CT or MRI.

[2] There are rare exceptions where nuclides other than the proton are measured in MRI, but the vast majority of applications involve the proton. For magnetic resonance *spectroscopy* (MRS), however, a wide selection of nuclides may be (and are) studied.

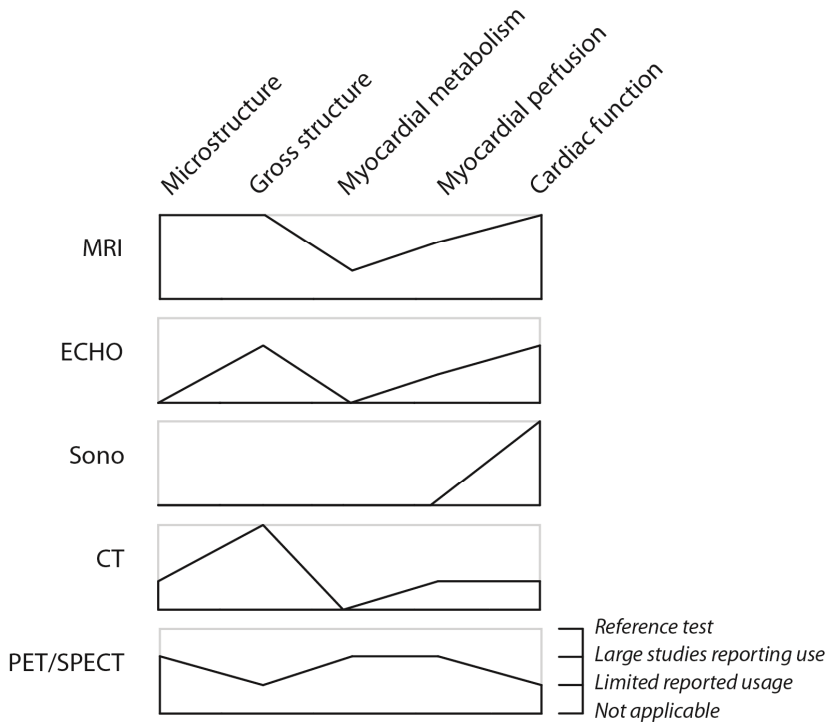

Figure 3.3 Comparison of relative characteristics between methods evaluating HF

Gross structure refers to cardiac volumes and major vessels. *Myocardial microstructure* includes evaluations of infarct, fibrosis and edema. *Sono* = sonomicrometry. This figure is inspired by (59) with data from (57)

3.3.1 ECHOCARDIOGRAPHY

Echocardiography is a quick, affordable and available technique frequently used to characterize cardiac function in small animals. However, it suffers from relatively low reproducibility since it oftentimes relies on geometric assumptions to do volume calculations (60). Also, high spatial resolution may be difficult to achieve, and the shadowing by the sternum in transthoracic ECHO limits the geometric views available to the operator (60).

ECHO is able to evaluate global cardiac function through e.g. 2D imaging allowing determination of cardiac dimensions and EF, and blood flow Doppler.

Regional myocardial function can be evaluated employing **Tissue Doppler imaging (TDI)** which relies, not surprisingly, on the Doppler Effect, in that the frequency of a reflected wave is modulated depending on the motion of the reflective substance. Consequently, the frequency shift in the reflected ECHO signal allows determination of the instantaneous motion of the tissue that reflected it. TDI has potentially very high temporal resolution, allows calculation of strain from the velocity data, and has been validated by sonomicrometry (5). However, measurements may have low spatial resolution and are limited to retrieve velocity information only in the

direction towards or away from the transducer (61, 62), and have been accused of being somewhat unreliable (63).

Two-dimensional Speckle Tracking Echocardiography (2D-STE) is another ECHO method (64) able to quantify regional myocardial deformation by tracking the displacement of the characteristic speckles in the images (due to interference in the myocardium) over time. 2D strain maps can be found from displacement analysis. 2D-STE has been validated by several methods (65, 66). It is widely available and used method, and speckle tracking has been applied, for instance, in demonstrating alterations after MI (67).

3.3.2 MAGNETIC RESONANCE IMAGING

MRI is intrinsically a multifaceted modality for imaging of the heart, allowing evaluation of regional myocardial function in areas from the entire heart, with practically no limitation in geometry (23). Implementation and modification of different MR imaging protocols renders an MRI system exceptionally and incomparably versatile, able to measure a wide array of different biological properties (50). The reader is referred to the Theory section for details on the principles of MRI.

A Selection of Techniques for Measuring Cardiac Function

Cine MRI is arguably the most fundamental MRI tool for studying the beating heart in vivo. In this technique, a series of images in is acquired rapid succession, allowing creation of "videos" of the beating heart. It is widely used clinically due to high soft-tissue contrast, and is the gold standard for noninvasive quantification of cavity volumes, ejection fraction, cardiac output and myocardial thickening, volume and mass (3, 30, 68-71). Although technological advances in the recent years have allowed quantification of myocardial dyssynchrony from cine images (72-74), cine MRI is in general not suitable for complex deformation analysis since the myocardium appears near-homogenous in the images. It is thus suboptimal to evaluate wall motion abnormalities compared to dedicated strain analysis (75).

MRI tagging was introduced in the late 80's (76, 77), and is an intuitive and robust technique for evaluating myocardial deformation. In tagging, patterns of dark bands are magnetically (and thus noninvasively) "carved" in the myocardium prior to a cine MRI acquisition, allowing tracking and time-resolved analysis of tissue displacement. This way, tagging overcomes the challenge in cine MRI of the myocardium appearing near-homogenously. Parameters such as twist, strain and strain rate can be derived (3, 18). Over the years, tagging and its derivatives (see below) have become the go-to technique for MRI-based quantification of myocardial deformation (21).

However, it suffers from low spatial resolution, suboptimal coverage of the cardiac cycle due to fading of the magnetization-induced patterns (typically affecting late diastole), and time-consuming data analysis. Furthermore, it only tracks in-plane deformation, limiting analysis to 2D tracking.

Harmonic phase (HARP) analysis is a technique allowing more rapid evaluation of tagged images (78), where the strain is calculated directly from the local spatial frequency of the tag lines. Clinically, HARP is the most widely used tool for measur-

ing regional myocardial mechanics, and has been developed to potentially reach very high spatial resolution (79).

Displacement encoded MRI with stimulated echoes (DENSE) (80) encodes tissue displacement over a certain time. DENSE involves a "spin prepping" step, typically applied immediately after the registration of an ECG trigger. A readout module is applied at a later time point, typically at end systole (81, 82). The tissue displacement between these events manifests as a phase shift in the readout signal. Multiphase DENSE refers to techniques where the displacement is measured at more than one time point throughout the cardiac cycle (83).

Strain encoded (SENC) MRI tags planes parallel to the imaging plane (84) as opposed to conventional tagging. Strain is calculated from images with different frequency modulation in the slice-selection direction. Thus, short-axis images deliver info on long-axis strain. SENC images are visually appealing and straightforwardly analyzed, as pixel intensity is directly related to strain. Integrating SENC with HARP (85) or DENSE (9) can produce 3D strain.

Despite their different historical origins and appearance; HARP, DENSE and SENC are mathematically very similar and in essence different implementations of the same principle of *phase displacement encoding* (3, 21, 86).

In **phase contrast MRI (PC-MRI)**, the motion of tissue or blood is systematically encoded into the signal phase, which becomes proportional to the velocity (87-89). PC-MRI is also called **velocity-encoded MRI** or, when used on tissue, **tissue phase mapping**. Compared to other phase displacement techniques, PC-MRI offers superior temporal resolution since the two displacement encoding events are executed back-to-back rather than at different time points within the cardiac cycle. This allows superior peak detection and sensitivity (90), and the ability to quantify subtle dyssynchrony. In addition, temporal integration of the velocity allows tissue tracking and analysis of displacement (90-95) and deformation (14, 88, 90, 96, 97) of the myocardium. PC-MRI therefore allows motion mapping with the same resolution as the underlying data matrix, and allows quantification of velocity, displacement and strain from the same raw data.

Other MR techniques with reported cardiac applications include *arterial spin labeling* for measurement of myocardial perfusion, *contrast-enhanced imaging* for MI quantification, and hydrogen and phosphorus *MR spectroscopy* for metabolism (19).

Comparison of MRI Techniques

The raw MRI signal is complex, in that it consists of both a magnitude and a phase component. In addition to superior spatial resolution, an advantage of PC-MRI over tagging is that the former encodes motion into the phase of the signal, leaving the magnitude images more or less undisturbed. Tagging, on the other hand, also disturbs the magnitude images.

DENSE and PC-MRI both use bipolar magnetic gradients (see Theory) that encode spin displacement into the phase of the signal; DENSE encode displacement over a long time (and uses multiple radio-wave (RF) excitations to circumvent T2* decay[3]), while PC over a very short, typically a few hundred μs. Both methods have

[3] T2* decay refers, in short, to the decay of measurable signal after an RF-excitation.

sufficient spatial resolution to measure transmural variation (21), but only PC-MRI can characterize the transmural variation of velocity (68). While recent developments of multiframe DENSE provide time-resolved displacement data, its temporal resolution is still inferior to PC-MRI (68). DENSE also requires suppression of unwanted signals due multiple RF excitations, which leads to increased acquisition time (81, 98, 99). On the other hand, DENSE avoids potential integration errors when large displacements are to be measured, and uses weaker gradients which reduces the generation of detrimental eddy currents. DENSE has intrinsically low signal-to-noise ratio (SNR) due to being based on stimulated echo, causing loss of 50% of the signal (3). Both HARP, DENSE and SENC are limited by T1 relaxation (21) which may render analysis of the whole cardiac cycle challenging. PC-MRI is not affected by this.

Very nice reviews by Tee et al. (23), Simpson et al. (21) and Wang et al. (3) treats all major MRI techniques for assessment of regional myocardial function.

MRI vs. ECHO Velocimetry

MRI and ECHO are fundamentally different techniques for evaluating myocardial function; each provides a bouquet of advantages and disadvantages compared to the other. The most commonly stated differences, although somewhat crude, are found in Figure 3.3.

ECHO is the go-to standard for fast, robust and high-temporal resolution assessment of in vivo cardiac function in small animals, including measurement of blood and myocardial motion, with minimal post-processing effort. However, high spatial resolution may be difficult to achieve, and it suffers from limitations due to restriction in available projections (acoustic windows) and difficulties in standardization of the geometry, which is an absolute requirement when assessing detailed function over time, for instance when evaluating disease progression. Moreover, ECHO exhibits a considerable inter-observer variability (23, 100), and current state-of-the-art ECHO machines for rodents cannot produce 3D velocity maps.

High-resolution ECHO Doppler velocimetry can only measure motion parallel to the ultrasound beam, thus angle correction must be incorporated if oblique motion is to be evaluated, which may reduce reproducibility and possible under-/ and overestimations of the motion. Blood flow measurements from PC-MRI are on several occasions found to be systematically higher than velocities measured using ECHO Doppler; this difference could be due to angle dependency in ECHO measurements (21, 101).

Jung et al. (102) compared TDI with myocardial PC-MRI in a single, precisely defined volume in the posterior wall, and the techniques demonstrate good correlation. However, the authors note that it is not obvious if good correlation would be found for the rest of the ventricle or in diseased hearts. Nowosielski et al. (103) concluded that MR was superior to ECHO in assessing myocardial function in the acute stages of MI. Also, some studies have suggested that the timing of radial and circumferential shortening may be more sensitive than longitudinal identifying dysfunction; however TDI is usually restricted to measuring the long-axis motion near the base for the ventricle (104). Still, long-axis motion correlates well between MR and TDI (61). In addition, MRI can not only measure global and regional cardiac function, it also allows evaluation of intramural motion patterns (105), which plays a key role in several diseases, for instance MI and cardiomyopathies.

MRI overcomes the geometrical limitations of ECHO, however at a cost of increased acquisition time and more cumbersome data analysis. But recent advances in real-time phase contrast MRI address this issue, with very interesting potentials (106, 107). Also, parallel imaging has been shown to reduce MRI acquisition times greatly without loss of accuracy (30, 108, 109).

Applications of Myocardial MRI: Humans

Myocardial MRI techniques can provide measurement of strain, strain-rate, torsion, twist and velocity, and have been shown to have potential clinical applications in e.g. coronary artery disease (110), MI (111), dilated cardiomyopathy (112, 113), hypertension (114), hypertrophic cardiomyopathy (115), LV hypertrophy (116), ventricular dyssynchrony (51) and diastolic dysfunction (117). One of the most important clinical applications of regional functional analysis is evaluation of reversibly injured yet viable myocardium in ischemic heart disease (118).

The application of myocardial PC-MRI has so far been limited mostly to research (basal and clinical), and has yet to enter the turf as a major player in clinical routine (119). Nevertheless, PC-MRI has been shown to be useful in several applications; including studies on normal heart motion (2, 101, 119-123), the effects on myocardial mechanics of age and gender (1, 124), MI (75, 90, 125, 126), heart failure (104), LV hypertrophy (127), ventricular dyssynchrony (104), hypertension, dilated cardiomyopathy and left bundle branch block (128, 129).

Applications of Myocardial MRI: Small Animals

The mice and rat hearts are two orders of magnitudes smaller than human hearts by weight (30, 130), and exhibit a resting heart rate up to ten times faster. Cardiac MRI in mice and rats thus understandably requires considerably higher resolution than in humans to offer comparable data yield; so high spatial and temporal resolution is of the essence when detailed regional myocardial function is to be evaluated (93, 105, 131-134). While field strengths of 1.5 or 3.0 T are most common in MR systems for human application, the majority of studies on small animals have been performed on higher-field systems, ranging from 4.7-17.6 T (19, 135). It is worth to note that successful small-animal experiments also have been performed on 1.5T, where loss of signal is to some extent compensated by dedicated coils (136, 137).

The myocardial mass of mice has been shown to be accurately determined by cine MRI (138-140). Cine MRI has been used for e.g. evaluating LV remodeling after MI (141) and the role of creatine in the heart (44). With ultra-high spatial resolution, myocardial fiber structure has been measured in isolated rat hearts (142-144).

MRI tagging has been used not only to investigate normal function in mice (69, 79), but also the roles of e.g. genes encoding for nitric oxide synthases in myocardial mechanics (145, 146) as well as altered contractile function after MI (147) and reperfused MI (148). Transmural myocardial strain has been calculated using HARP (79), as has 3D wall strain in mouse model of dilated cardiomyopathy (149). 2D multiframe DENSE has been employed in mice for the purpose of investigating the role of neuronal nitric oxide synthase in EC-coupling (150) and for evaluation of functional changes following MI (81, 82).

PC-MRI has been employed in normal mice (17), and in mice with mitochondrial and cytosolic creatine kinase knockout (151), with MI (105, 131, 132), and have been used to characterize transmural variation of motion after ischemia-reperfusion in mice (68).

Limitations with PC-MRI

PC-MRI has been designated to represent a unique asset of cardiovascular MRI (152). As already mentioned, it combines into one protocol the geometrical advantages of MRI with velocity, displacement and strain measurements. However, two of the main concerns with PC-MRI are 1) the need for optimal temporal resolution to ensure sufficient accuracy in detection of peak velocities, and 2) the challenge with eddy current induced baseline shifts. As we will see, these two issues are closely related.

In human applications, it has been recommended to cover the cardiac cycle with at least 60 frames (that is, 60 frames per cycle) to being able to accurately derive strain from velocity data or analyze strain-rate (25, 153). Detailed analysis of myocardial motion in humans with PC-MRI has been done at a temporal resolution 13.8 ms, corresponding to 60-70 frames per cycle, depending on heart rate (101). Accordingly, in small animal research, high spatiotemporal resolution is of the essence. Suboptimal temporal resolution attenuates high-frequency components of the velocity data, compromising for instance measurement of peak motion and displacement assessment from velocity data.

The first publication on myocardial PC-MRI in rodents was in 2003 (131), nearly 20 years after the method's first description, and the research on optimization of preclinical PC-MRI has been limited since. At present, the highest temporal resolution in myocardial PC-MRI published in animal applications acquired just below 30 frames per cycle (17, 68). This challenge is reflected in the overarching theme of this thesis; namely to further develop myocardial PC-MRI, of which a central task is to improve temporal resolution, towards being a robust and versatile tool in cardiovascular research.

3.4 THEORY

A majority of the results in this thesis is related to the optimization of phase contrast MRI for small-animal research. In this section, a short summary of the theory behind PC-MRI will be provided, along with its primary challenges and data yield.

Section 3.4.1 provides a rough qualitative description of MRI in general and PC-MRI in particular, as well as central applications. Section 3.4.2 is a tad more theoretical and introduces the central principles governing PC-MRI and provides the formal backdrop for the aims and results of the papers. The remaining sections treat the formalities behind some of the challenges and applications of PC-MRI; leading up to the main aims of this thesis in Section 4.

3.4.1 PHASE CONTRAST MRI: A PRIMER

MR: The Tango of Magnetism and Radio Waves

Magnetic resonance (MR) is the umbrella term for a large collection of techniques relying on the quantum mechanical property of an atom known as *spin,* a directional quantity. Nuclides (atoms) that have an odd number of core particles (that is, protons and neutrons) are MR-active and may be studied using MR. Examples of such nuclides are isotopes of hydrogen (^{1}H), carbon (^{13}C), sodium (^{23}Na), fluorine (^{19}F) and phosphorus (^{31}P). In MR imaging, the vastly most studied nuclide is ^{1}H, whose core consists of a single proton. The present work focuses solely on hydrogen.

In the presence of a magnetic field (strong or weak), MR-active nuclides (hereby referred to as *spins*) find themselves in their most stable state by aligning their spins parallel with the magnetic field. Unfortunately, spins of interest are generally not at absolute zero temperature, which means that thermic energy persistently and vigorously shakes them around. This energy, dictated by Boltzmann's law, is far stronger than the energy each spin "saves" by aligning themselves along with the magnetic field[4]. As a crude analogy, we may consider a bunch of compasses, which tend to point to north, but find themselves in a tumble dryer (154). If we were to observe a single compass, it would indeed *not* point to north most of the time. However, if we found some way to measure the orientation of a *huge* number of compasses, we would indeed expect to find a small tendency among them pointing towards north. Luckily, our bodies contain roughly 50.000.000.000.000.000.000.000 "compasses" per cubic centimeter (I never counted), which makes is possible to detect this tendency of pointing towards "north".

The fundamentals of MR are oftentimes taken to be abstract and not easily accessible where one needs quantum mechanics to understand what happens. However, according to Hanson (154), MR experiments actually do *not* force the individual spins into their eigenstates—therefore single-particle quantum mechanics analysis is neither necessary nor appropriate. We may therefore consider instead how a bunch of spins behaves. Much like a spinning top will exhibit a precession when spinning in a gravity field (precession = the slow rotation of the rotation axis itself around the gravitational field lines); the spins will also show a similar behavior. Now, we are at the core of MR techniques, as described in a legendary paper from 1938 by Isidor Rabi et al (155). An MR-active nuclide will precess at a frequency proportional to the strength of the magnetic field it experiences, and it will be able to absorb and emit energy at the corresponding wavelength. Consequently, by imparting energy to the spins at just the right wavelength (this is known as RF excitation), they become excited and will soon reemit that energy in form of detectable radiation. This is the signal that is measured and used in MR.

Magnetic Resonance Imaging

Spatially encoded magnetic resonance applied for imaging is, to no surprise, termed magnetic resonance imaging (MRI). Spatial encoding is simply done by altering the magnetic field a tad (this is done by applying a magnetic *gradient*), which makes the

[4] In fact, for a 9.4 T MR system in room temperature, there is on average about 32 spin per million that contribute to the MR signal.

resonance frequency a function of position. By measuring the frequency of the MR signal we can determine where the signal originates.

All radiation in MR is in the range of radio signals, and is thus non-ionizing[5]. In a 9.4 T MR system, which has been used in the work in the present thesis, the radiation associated with protein/hydrogen imaging is about 400 MHz.

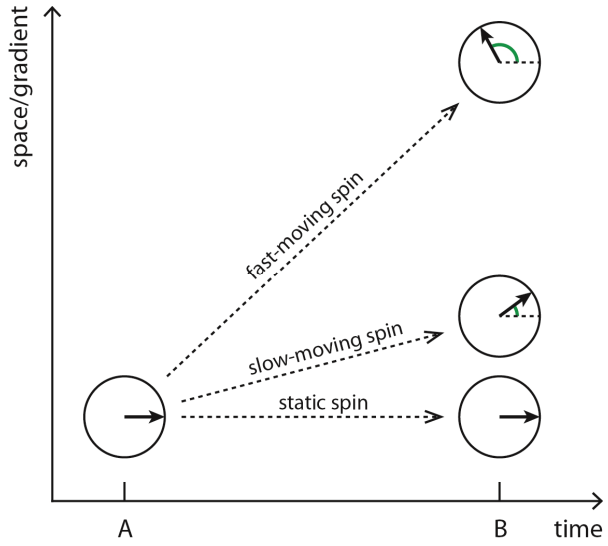

Figure 3.4 Simplified concept of phase contrast MRI

In PC-MRI, a given spin accumulate a phase (green arc) proportional to its velocity, that is, the distance it moves along the velocity-encoding gradient over a well-defined time (here, from A to B). This illustration is somewhat simplified; in that static spins in reality does *not* have zero phase over time (in a 9.4 T MR system, spins finish about 400.000 complete rotations per millisecond). In addition, even a minor variation in the magnetic field would affect the rotation speed, and thus phase accumulation, greatly. This is why PC-MRI requires several acquisitions with slightly different settings of the velocity encoding gradients, which are subtracted to remove the contribution of unknown/uncontrollable magnetic field inhomogenieties.

Phase Contrast MRI

Since we are talking about rotating spins with a *direction*, we can not only measure their abundance (magnitude of the MR signal), but also their orientation (phase of the MR signal). In other words, MR is, as opposed to i.e. CT, a phase sensitive technique (156). Yet, in the majority of clinical applications of MRI, the phase component is discarded and only the magnitude component is visualized and analyzed. The phase, however, can provide very useful information; such as magnetic field inhomogeneity or spin motion. In PC-MRI, the motion of the spins is systematically encoded into the phase of the MR data, in addition to the magnitude component that offers information on signal strength (which, again, is a function of spin density among other effects).

[5] Non-ionizing radiation is traditionally used to denote electromagnetic radiation with energy (the inverse of wavelength) sufficient to damage DNA. Examples of non-ionizing radiation are radio waves, microwaves and visible light. Examples of ionizing radiation are x-rays and gamma rays.

As mentioned, spins in MR precess with a frequency proportional to the magnetic field at their location. In summary, PC-MRI encodes the average motion within a given volume into the MR signal of that particular volume in two steps; first, a magnetic gradient with a certain direction is applied over a short period to alter the precession frequency slightly as a function of position. After this gradient is turned off, the spins will have had a different precession frequency for a short time, and thus accumulated different phase which is dependent on their position. Then, a second gradient is applied with opposite polarity, rewinding the phase dispersion caused by the first gradient. A stationary spin will then experience two consecutive alterations in its local magnetic field, exactly cancelling each other out, and be left with zero net change in phase. However, if the position of a spin *changes* between the two gradients, the phase effects of the two gradients will *not* cancel, and the spin is left with a net accumulated phase. The accumulated phase is proportional to component of the distance travelled by the spin that is parallel to the direction of the gradients. As the time between the gradient is known to the operator, the average velocity in that time period is readily calculated. This concept (although simplified) is illustrated in Figure 3.4.

Stronger motion encoding gradients results in a larger accumulated phase for a given displacement, and therefore yields better sensitivity to low velocities. Since the phase can be unambiguously interpreted only within a $360^{o}/2\pi$ window, the maximum velocity that can be measured (the venc) is simultaneously lowered.

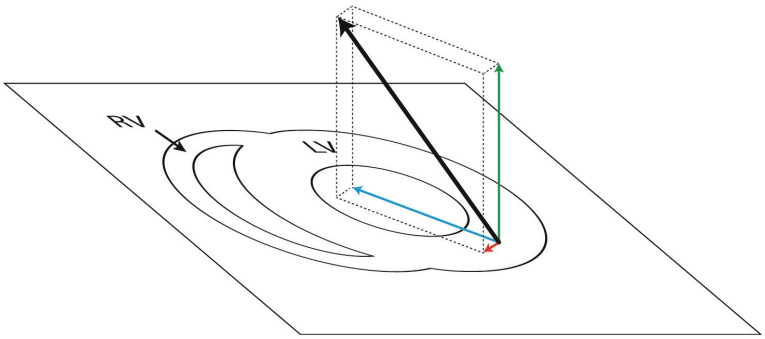

Figure 3.5 Phase contrast MRI velocity

Using three-directional PC-MRI, a 3D velocity vector (black) can be reconstructed in each pixel for each time point. This vector can subsequently be decomposed into a coordinate system defined by the in-slice center-of-mass of the left ventricle; with its radial (blue), tangential (red) and longitudinal (green) components. LV = left ventricular myocardium, RV = right ventricular myocardium.

PC-MRI Data Yield

The primary output data from a PC-MRI dataset are near-instantaneous pixel-wise time-resolved velocities (Figure 3.5). This allows evaluation of for instance peak motion, time-to-peak, myocardial twist directly. Furthermore, temporal integration of the velocity allows calculation of displacement (94, 95), which again can be spatially differentiated to find strain (90, 96, 97, 122). Analogously, the spatial differential of

velocity is the strain rate (88, 125). The mathematical relationships between motion, position, strain rate and strain are illustrated in Figure 3.6.

PC-MRI was first described in papers nearly as old as the author of this thesis (157, 158), and has since been developed to be a widely available standard sequence in clinical MR systems. In research, it is extensively used for blood flow analysis (87, 134, 159-173), but has in the last decade been revealed as a potent and versatile tool for assessing myocardial motion (1, 13, 14, 17, 68, 75, 90, 101, 102, 104, 105, 112, 114, 119-121, 124-129, 131, 134, 174). The latter is in general more challenging than the former, since 1) the signal intensity from the myocardium is typically lower than the signal from blood and 2) the velocity of the myocardium is substantially lower than that of blood, so higher velocity sensitivity is required. Nevertheless, intra- and interobserver variability in myocardial PC-MRI have been shown to be low (119).

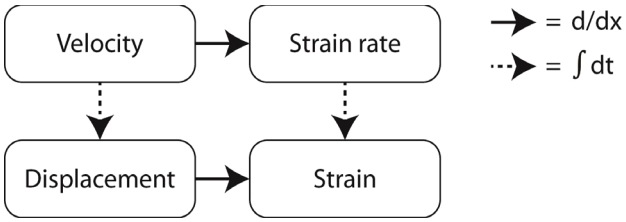

Figure 3.6 The relationships between time- and spatially resolved position data

Displacement and strain rate are the temporal integral and spatial derivative of the velocity, respectively. The spatial derivative of the temporal integral (or the temporal integral of the spatial derivative) of velocity is strain. All arrows can be inverted, then representing the inverse operation (integration becomes differentiation and vice versa).

3.4.2 PC-MRI Signal Generation

The Larmor Equation

The precession frequency of an MR-active spin in a magnetic field B is governed by the Larmor equation:

$$\omega = \gamma B \qquad [3.1]$$

where γ is the gyromagnetic constant. In general, B, and therefore ω, are functions of time and position. By integrating the Larmor equation, the accumulated phase after a time t at position $\vec{x}$ can be determined:

$$\phi(\vec{x}, \mathrm{t}) = \int_0^t \omega(\vec{x}, \tau)\, d\tau = \gamma \int_0^t B(\vec{x}, \tau)\, d\tau. \qquad [3.2]$$

A linear gradient $\vec{G}$ yields a local magnetic field at position $\vec{x}$ equal to $\vec{G} \cdot \vec{x}$. The contribution to the phase due to such a gradient is therefore

$$\phi(\vec{x},t) = \gamma \int_0^t \vec{G}(\tau)\cdot\vec{x}(\tau)\,d\tau. \qquad [3.3]$$

Expanding $\vec{x}(t)$ around some time $t = 0$ yields

$$\vec{x}(t) = x_0 + v_0 t + \frac{1}{2}a_0 t^2 + \cdots. \qquad [3.4]$$

By combining Eqs. 3.3 and 3.4, we can find the total accumulated phase of a voxel whose spins have position $\vec{x}_0$ and velocity $\vec{v}_0$:

$$\phi = \vec{x}_0 \cdot \gamma\vec{M}_0 + \vec{v}_0 \cdot \gamma\vec{M}_1 + \phi_{\text{other}} \qquad [3.5]$$

where $\vec{M}_0$ is the *zeroth gradient moment* ($\vec{M}_0 = \int_0^t \vec{G}(\tau)\,d\tau$), $\vec{M}_1$ is the *first gradient moment* ($\vec{M}_1 = \int_0^t \vec{G}(\tau)\,\tau\,d\tau$), and ϕ_{other} is the phase from other contributors, including acceleration and the main magnetic field.

The Math of Phase Contrast

A very nice overview of the theoretical foundation of PC-MRI is found in Chapter 9.2 in Bernstein's *Handbook of MRI Pulse Sequences* (156). Here, we provide a short outline.

The concept behind phase contrast MRI is to employ a gradient complex whose zeroth moment is zero ($\vec{M}_0 = 0$ in Eq. 3.5; the time-amplitude area), but first moment ($\vec{M}_1$) is nonzero. The simplest example of this is a bipolar gradient (Figure 3.7). The velocity is determined from Eq. 3.5 by acquiring several datasets with different first moments, but all other imaging parameters are kept unchanged (175). Since $\vec{M}_0 = 0$ and assuming that ϕ_{other} is independent on $\vec{M}_1$, the difference in phase ($\Delta\varphi$) between two such data sets is found simply from Eq. 3.5:

$$\Delta\varphi = \gamma\Delta\vec{M}_1 \cdot \vec{v}_0 \qquad [3.6a]$$

where $\Delta\vec{M}_1$ is the difference in first gradient moment between the datasets. Eq. 3.6a is the fundamental equation in phase contrast MRI. Note that the phase is proportional to the component of the velocity vector parallel to the direction of the encoding gradient. In this, the contribution to the phase of acceleration and higher-order terms of motion is neglected; which is not obviously correct, but has been shown to be a reasonable assumption in myocardial PC-MRI (105, 131, 176).

The velocity is reconstructed from this phase difference by reconfiguration of Eq. 3.6a:

$$v_0 = \frac{\Delta\varphi}{\gamma \Delta M_1}. \qquad [3.6b]$$

Since the encoded phase in Eq. 3.6a is proportional to the component of $\vec{v}_0$ parallel to the encoding gradient, v_0 in Eq 3.6b is the reconstruction of this component. Accordingly, 3D velocity may be measured by acquiring several datasets where the direction of $\vec{M}_1$ is varied. In general, the encoding (Eq. 3.6a) and reconstruction (Eq. 3.6b) can be written on matrix forms

$$\overrightarrow{\Delta\varphi} = \mathbf{A} \cdot \vec{v} \qquad [3.7]$$

and

$$\vec{v} = \mathbf{A}^{+} \cdot \overrightarrow{\Delta\varphi} \ . \qquad [3.8]$$

Here, $\mathbf{A}$ is the *acquisition matrix;* it contains the values of $\gamma \Delta \vec{M}_1$ used. $\mathbf{A}^{+}$ is the Moore-Penrose pseudoinverse of $\mathbf{A}$ (177, 178).

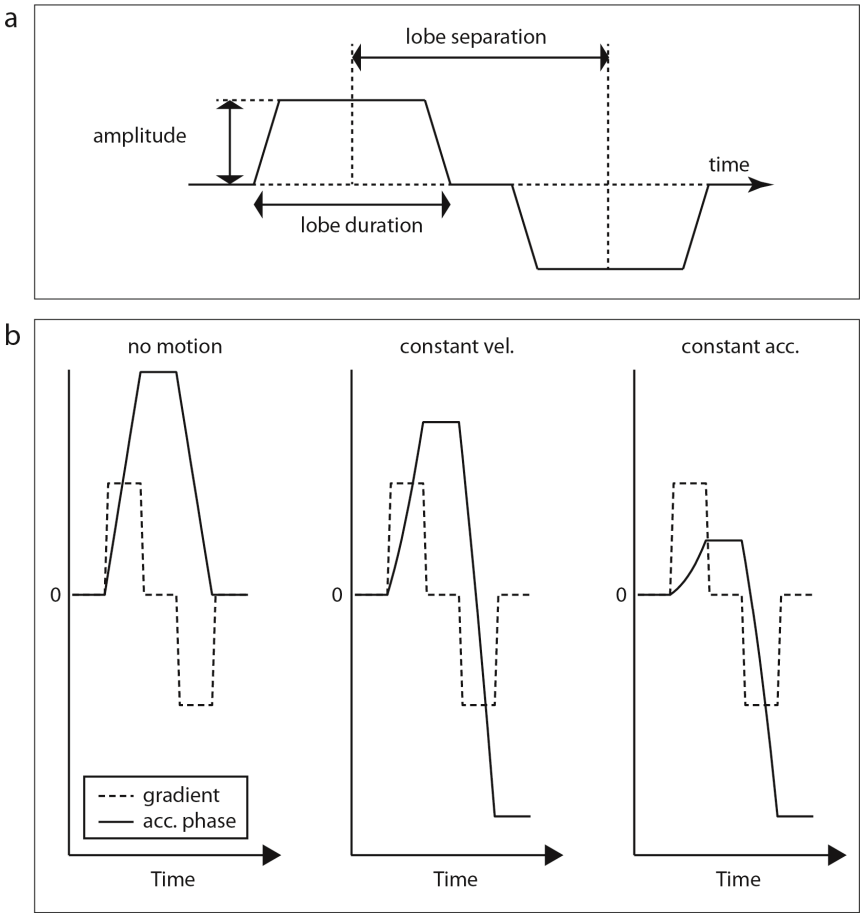

Figure 3.7 Bipolar gradient

a) A bipolar gradient with equal positive and negative lobes, as illustrated here, has zero 0^{th} gradient moment but non-zero 1^{st} gradient moment. Since the net area under the lobes is zero, the first moment is simply AT (independent of temporal origin), where A is the time-amplitude area of a single gradient lobe and T is the lobe separation. The reader is referred to Chapter 10.4, *Gradient Moment Nulling*, in Ref. (156) for more details.

b) The effect of a bipolar gradient (dashed line) on the accumulated phase of a spin (solid line), following Eq. 3.5; under no motion, constant velocity and constant acceleration. The unit on the y-axes is arbitrary. Here, ϕ_{other} is defined to be zero.

PC-MRI Encoding Strategies: The Architecture of the Acquisition Matrix

There are several approaches to recording 3D motion. They are described in Paper I and in Refs. (175, 177), and a short overview is provided here.

- **Six-point** method uses three pairs of gradients, each pair measuring the three Cartesian velocity components.
- **Referenced four-point** method utilized a common reference scan and three orthogonal encoded scans.
- **Balanced four-point** method utilizes four encoded scans, where the first moments are altered in pairs. Compared to referenced four-point, the variance is reduced at the cost of increased intricacy of dynamic range.
- **Balanced five-point** method utilized the same four encoded scans as balanced four-point, but adds a fifth reference scan. This ensures improved velocity-to-noise efficiency with less than 1% increase in scan time, as the resolution of the reference scan can be heavily reduced.

Perhaps the most intuitive way of recording three directional velocity is the referenced four-point method, where four datasets are acquired; in which three $\gamma\vec{M}_1$ is oriented in mutually orthogonal directions and a fourth dataset in which $\vec{M}_1 = 0$. In this case, $\gamma\Delta\vec{M}_1 = \gamma\vec{M}_1$ and the acquisition matrix and its pseudoinverse become

$$\mathbf{A} = \begin{bmatrix} 1 & 0 & 0 \\ 0 & 1 & 0 \\ 0 & 0 & 1 \end{bmatrix} \cdot \gamma\vec{M}_1 \qquad [3.9a]$$

$$\mathbf{A}^{+} = \begin{bmatrix} 1 & 0 & 0 \\ 0 & 1 & 0 \\ 0 & 0 & 1 \end{bmatrix} \cdot \left(\gamma\vec{M}_1\right)^{-1}. \qquad [3.9b]$$

The Venc

Phase information is only uniquely defined in the interval $(-\pi\,, \pi)$, and aliasing will occur if the acquisition generates data outside this range. The highest (positive or negative) velocity that can be measured without aliasing to occur, referred to as the *venc*, is found from Eq. 3.6b:

$$venc = \frac{\pi}{\gamma\Delta\vec{M}_1}. \qquad [3.10]$$

The venc is an important quantity in PC-MRI, as it defines the upper threshold for unambiguous velocity quantification, as well as the sensitivity of the protocol to low velocities (Figure 3.8a). Specifically, myocardial PC-MRI demands lower venc values, typically by a factor of ten, than blood flow PC-MRI. From Eq. 3.10, we can see that this requires ten times higher values for $\Delta\vec{M}_1$.

3.4.3 EDDY CURRENTS

Whenever a magnetic field **B** changes in time, eddy currents build in nearby conductors. This is dictated by Faraday's law:

$$\mathcal{E} = -\frac{\partial \Phi}{\partial t} \qquad [3.11]$$

where $\mathcal{E}$ is the electromotive force (basically a source of voltage) and Φ is the magnetic flux (**B** per unit surface).

Nature loves symmetry, and Maxwell's equations, that govern classical electrodynamics, has got a lot of it. So, just as a time-varying magnetic field creates a current, a time-varying current will create a magnetic field. Thus, the currents generated according to Eq. 3.11 will create new magnetic fields in addition to the original field, but with opposite sign (in accordance with Lenz's law; hence the minus sign the equation). As magnetic resonance techniques relies on a fine-tuned and well-behaved magnetic environment, any perturbing magnetic fields will cause trouble (179).

To enhance SNR, reduce susceptibility artifacts and improve temporal resolution (105), short pulse sequences are desirable. On the other hand, to achieve high spatial resolution and velocity sensitivity, strong gradients are desirable. In sum, this requires stronger and/or more rapid gradients. Since the rate of buildup of eddy current is proportional to the slew rate of the magnetic gradients, stronger gradients creates stronger eddy currents (156). This renders high-field and high-resolution MRI particularly prone to eddy current induced artifacts.

Eddy Current Effects in PC-MRI

It is not an exaggeration to state that eddy currents plague the world of phase-based imaging (except, perhaps, for its ability to produce PhD theses). They are hardware-specific and practically impossible to predict (152, 180). Eddy current induced errors tend to increase with the distance from the center of the magnet, and may vary unpredictable with slice orientation and position as well as any other parameter that affect gradient waveforms and their timings. They generally vary with position, but are relatively stable in time if proper gating is employed (91, 165).

Being a phase-sensitive technique employing strong gradients, PC-MRI is particularly sensitive to artifacts originating from eddy current generated in the system.

Any eddy currents in the system will create perturbing magnetic fields, entering as a contributor to ϕ_{other} in Eq. 3.5. However, the eddy currents are in general *not* independent of gradient activity, and thus not constant under altered $\vec{M}_1$. Consequently, eddy current effects are not eliminated by the phase contrast calculation (156, 181), and will constitute a phase offset in the velocity-encoded datasets. This inevitably introduces spatially varying errors in velocity measurement (94, 162, 179, 182, 183) that must be corrected.

Another consequence of eddy current induced offsets in the baseline phase is alteration in the venc, that is, the highest velocity that can be measured unambiguously in the 2π window (see Figure 3.8a). In the presence of a shift in the baseline, the phase headroom in a given pixel will be altered, and become dependent on the

direction of the velocity (Figure 3.8b). However, the *range* of the "allowed" velocities within that pixel is unaffected (green arrows in Figure 3.8b), as the phase is readily windowed into the [-π,π] range after phase correction (Figure 3.8c).

Eddy current induced errors enter Eq. 3.7 as a perturbing contributor:

$$\overrightarrow{\Delta\varphi} = \mathbf{A} \cdot \vec{v} + \vec{\varphi}_{EC} \ . \qquad [3.12]$$

Eddy Current Compensation

As the name suggests, eddy current compensation (ECC) techniques aim to reduce the effect of eddy currents. Hardware ECC includes active gradient shielding and replacement to components with non-conductive materials (152). The adverse effects of eddy currents at signal readout can also be reduced by introducing a short delay (~200 μs) between the encoding gradients and the readout module (131), to allow for some decay of the currents. However, this does not reduce the effect of eddy currents produced at the time of flow encoding on the encoding itself.

Thus, ECC might, and in many cases must, also to be incorporated in post-processing of the PC-MRI data. These errors are not readily predicted analytically and thus not easy to correct by other means then numerical approaches (165, 181-184). A number of techniques have been described aiming to reduce the impact of eddy current induced errors in PC-MRI, most are based on the identification and removal of non-zero phase in static regions (in which the phase *should* be zero). This includes for instance placing a phantom within the FOV to measure static-region phase (68), or performing a separate scan of a large static phantom with identical acquisition parameters (162, 184). The drawbacks of these two methods are limited spatial information of the baseline shift (152) and increased acquisition time, respectively. Another approach circumvents these shortcomings through exploiting static tissue already present in the FOV (179), which in cardiac imaging typically is the chest wall.

Pixel-by-pixel windowing of the phase after any adaptation of ECC prior to velocity reconstruction is critical to avoid alterations in the venc. In post-processing, implementation of an ECC technique modifies Eq. 3.12 to

$$\overrightarrow{\Delta\varphi} = \mathbf{A} \cdot \vec{v} + \vec{\varphi}_{EC} - \varphi_{ECC} = \mathbf{A} \cdot \vec{v} + \vec{\epsilon} \qquad [3.13]$$

where $\vec{\epsilon}$ is the residual phase error, also referred to as fitting residual. These residuals originate from the inability of ECC to produce perfect correction maps, since EC-induced baseline shift maps typically have intricate spatial variance. The fitting residuals are scattered around zero if proper fitting is employed (185). In theory, increasing the number of encoding steps (that is, the rows of **A**) is expected to reduce the error in the reconstructed velocity following the concept of signal averaging. This led to the first aim of this thesis, namely to explore the impact of increasing the number of encoding steps in PC-MRI.

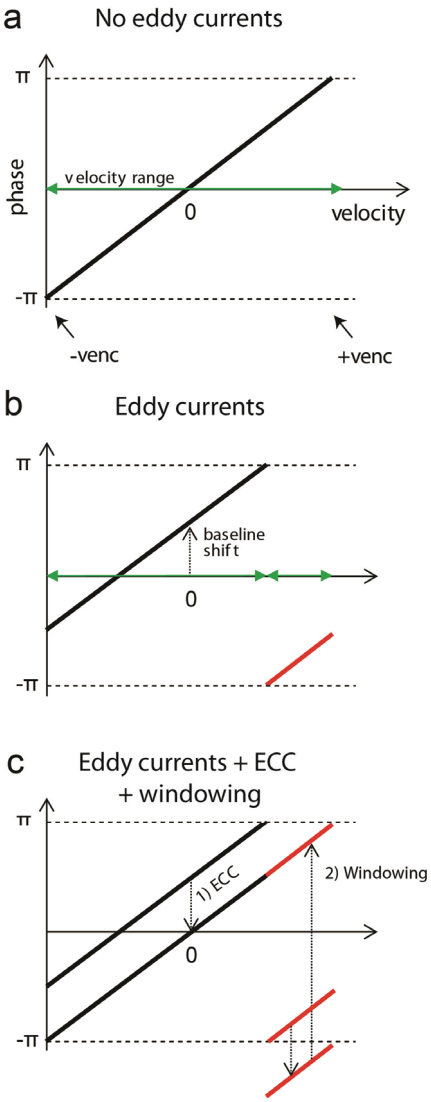

Figure 3.8 Alterations in venc due to baseline shift

If the baseline is shifted, the venc is scewed. The maximum and minimum velocities that can be measured without phase aliasing (**a**) is altered if the baseline of the phase is shifted (**b**). However, the *range* of velocities are unaffected, as the data is readily windowed into the [-π,π] range after ECC (**c**).

Challenge with Conventional ECC

Whenever ECC exploits spatially-resolved static-region phase (being a phantom or static tissue within the imaging subject), baseline phase shifts are corrected by subtraction of a map determined by fitting a surface to the phase in static regions. In this, an assumption is made that the baseline shift is spatially continuous.

However, since phase is only defined in a 2π range, sufficiently strong eddy currents will cause the baseline phase shift to "wrap". Since, in general, the shift in the baseline is spatially heterogeneous, this wrapping will cause discontinuities of 2π within static regions and cause the surface fitting to produce erroneous results. In this case, conventional ECC is insufficient. This motivated the second aim of this thesis, namely to develop an improved ECC technique able to handle wrapping in the baseline phase.

3.4.4 Flow Artifacts and Gradient Moment Nulling

Artifacts in the myocardium due to blood flow pose a problem since it greatly reduce the reproducibility of motion trajectories calculated from PC-MRI data (186). In general, flow artifacts originate from any uncorrected phase shifts due to motion (187, 188). If time-varying motion (periodic or non-periodic) occurs in the imaging volume (such as intraventricular blood motion), standard (Cartesian) MRI encoding will suffer from more or less detrimental displacement artifacts or ghosting with a particular directionally dependency[6] (156, 189, 190).

As noted above, a spin experiencing a gradient accumulates a certain phase. If the spin is moving, its phase is a function of its motion, the gradient design and time. **Gradient moment nulling** refers to the design of a gradient complex (and its gradient moments) to ensure no net phase shift.

- Zeroth-order nulling ($\vec{M}_0 = 0$) ensures that static spins are properly rephased, and is used in virtually all MRI pulse sequence designs. A bipolar gradient (Figure 3.7) may easily be designed to be zeroth-order nulled by keeping the net time-amplitude area zero.
- First-order nulling ($\vec{M}_1 = 0$) ensures that spins in constant motion are rephased; and is referred to as *velocity compensation*. It can be constructed from a minimum of three gradient lobes.
- Second-order nulling ensures that spins in constant acceleration are rephased; and is referred to as *acceleration compensation*. It can be constructed from a minimum of four gradient lobes.

And so the story goes. As the keen reader may have noticed, a PC-MRI sequence is necessary *non*-velocity compensated, since it deliberately imposes a phase shift to moving spins (i.e. not first-order nulled). Thus, PC-MRI is particularly sensitive to motion-related artifacts (94, 191). Since these artifacts manifest in a certain direction, we are left with a major challenge when regional analysis is to be performed.

[6] That is, in the phase-encoding direction

The major remedy to reduce this problem in PC-MRI is to reduce the blood signal by use of a black-blood technique (68, 186, 192). However, complete elimination of the blood signal is nearly impossible, rendering flow-related artifacts a challenge in myocardial PC-MRI, particularly in regional analysis. This challenge is an important part of the third aim of this thesis, concerning the establishment of an optimal acquisition protocol and dedicated post-processing tools for measuring and parameterizing regional myocardial motion.

3.4.5 MYOCARDIAL STRAIN

Strain represents relative deformation, and is defined as the fractional change in length of an object relative to its original length. An advantage of analyzing strain compared to motion is that the former is independent on bulk organ translation and rotation (14).

There are several ways to calculate myocardial strain from velocity or displacement data. Generalized one-dimensional Lagrangian strain, also known as *material strain*, is defined as

$$\varepsilon_L(t) = \frac{L(t) - L(0)}{L(0)} \qquad [3.14]$$

where L(t) is the length of the object at time t, and L(0) is trivially constant over time. Lagrangian strain follows the tissue over time, i.e. it uses the myocardium itself as a reference system/coordinate system.

An alternative to the Lagrangian strain is the Eulerian strain, also known as *natural strain*. It is defined as

$$\varepsilon_E(t) = \int_0^t \frac{L(\tau + d\tau) - L(\tau)}{L(\tau)} d\tau. \qquad [3.15]$$

Eulerian strain describes the tissue strain at fixed points in space/the laboratory system.

In practice, this means that a positive Eulerian strain will be smaller than the Lagrangian equivalent, and a negative Eulerian strain will be larger than the Lagrangian equivalent. Comparing different techniques, it is important to assure that the strains compared are measured in the same coordinate system.

MR tagging is intrinsically a Lagrangian modality, while SENC is Eulerian. HARP, DENSE and PC-MRI can provide strain in both formalisms (21, 81, 193).

The Strain Tensor

Strain is in reality a 3D property. In a cardiopolar coordinate system, consisting of radial, circumferential and longitudinal components (defined in Section 5.3.3; see Figure 3.5), the myocardial strain tensor can be defined as (21)

$$strain\ tensor = \begin{pmatrix} \varepsilon_{RR} & \varepsilon_{RC} & \varepsilon_{RL} \\ \varepsilon_{CR} & \varepsilon_{CC} & \varepsilon_{CL} \\ \varepsilon_{LR} & \varepsilon_{LC} & \varepsilon_{LL} \end{pmatrix}. \quad [3.16]$$

The entries along the diagonal are referred to as *normal* strains. These are the parameters most commonly referred to; ε_{RR} (radial thickening), ε_{CC} (circumferential shortening) and ε_{LL} (longitudinal shortening). The strain tensor allows determination of principal axis of strain without any assumption on cardiac structure or direction of myocardial motion (14).

Oftentimes, one-dimensional strain, represented by a single entry in the strain matrix, is assessed and reported. The most straightforward measure of one-dimensional strain is myocardial thickening relative end-diastolic wall thickness, constituting an estimate of ε_{RR}. In general, however, measurements of ε_{RR} is more prone to noise than ε_{CC} due to limited number of transmural data points. Consequently, many studies have focused on circumferential strain (85, 147, 194-197).

PC-MRI Strain

To the best of our knowledge, no study has evaluated myocardial strain in small animals using PC-MRI. This led to another important component of the third aim of this thesis; namely to calculate and parameterize regional myocardial strain in the rodent heart.

Though, as mentioned earlier, purely mechanical parameters (Figure 3.2) do not reflect oxygen/energy consumption which conveys more comprehensive information of myocardial function (4-8). No study has, to our awareness, evaluated in vivo regional work in the hearts of small animals. The fourth (and last) aim of this thesis was therefore to evaluate PC-MRI based assessment of regional work in the rodent heart.

4 MAIN AIMS

The overarching aim of this thesis is the following:

To develop, optimize and apply high-resolution MRI and analysis tools allowing assessment of regionally resolved in vivo myocardial motion, deformation and work in healthy and diseased small-animal hearts

We have divided this into four sub aims:

1. PC-MRI allows noninvasive time-resolved assessment of 3D in vivo motion. However, to evaluate global and regional function with high sensitivity and spatiotemporal resolution, strong motion encoding gradients are required. This renders this methodology particularly prone to artifacts induced by eddy currents. The first aim in this thesis was therefore **to develop an optimized encoding strategy for PC-MRI, designed to be more accurate in the presence of strong and rapidly changing magnetic gradients, allowing measurements of myocardial motion with high resolution and sensitivity.**

2. When the limits of the achievable resolution are further pushed, eddy currents generated in the system during acquisition may be sufficiently large to cause wrapping in the baseline phase. This renders conventional approaches to eddy current correction in post-processing inadequate. The second aim was therefore **to develop an improved eddy current compensation technique able to handle wrapping in the baseline phase.**

3. Possessing technology able to measure 3D motion with high resolution, optimal imaging parameters and post-processing tools are essential to gain novel insight into the complex motion and deformation of the rodent myocardium. The third aim in this thesis was therefore **to establish optimal acquisition parameters for assessing the function of the rat myocardium, and develop suitable post-processing tools for analyzing PC-MRI data, including calculation of myocardial strain and parameterization of the regional function of LV.**

4. Myocardial motion and strain are load dependent, and does therefore not represent the actual work done by the cardiomyocytes. The fourth aim in this thesis was therefore **to implement a mathematical model allowing calculating of regional myocardial work based on noninvasive cine and PC-MRI data in combination with simple measurement of peak systemic blood pressure.**

5 METHODS

This section presents the different methods used in the papers. For further details on the methods, the reader is referred to the individual papers.

5.1 EXPERIMENTAL MODELS

5.1.1 MODELS EMPLOYED IN THIS WORK

All animal experiments were performed according to National Institutes of Health guidelines (NIH publication no 85-23, revised 1996) and approved by the Norwegian National Animal Research Authority. In Paper I, C57BL/6 wild-type mice were imaged to demonstrate the improved efficiency of the proposed acquisition scheme in vivo. In Paper II-IV, male Wistar rats (~300 g) with and without coronary artery ligation were used to demonstrate improved eddy current compensation (Paper II; only sham-operated animals), calculation of regional strain (Paper III) and calculation of regional work (Paper IV).

Naturally, care was taken to honor the three R's of animal experiments conduct; namely to reduce, replace and refine the usage of experimental animals.

As noted in the Introduction, the detection and quantification of disrupted regional function relies on comparison to the normal range of that region (2, 12). This stressed the need for control groups of normal animals representing baseline function.

5.1.2 EXTRAPOLATING PRECLINICAL FINDINGS TO HUMANS

The use of small animal models in cardiac research relies on assumptions that cardiac mechanics are comparable across spices, and that the disease models have distinct transferrable value to human conditions.

Most will appreciate the obvious phenotype differences between rodents and humans, such as fur, tail, ears, and size. The human LV is over 100 times the weight of the rat LV (130), and 200 times the weight of the mouse LV (30). Also, there are basic physiological differences, such as heart rate (5-10 times the heart rate of humans). Despite these distinctive differences, similarities in anatomy and fiber architecture suggest that fundamental cardiac mechanics may be similar between species.

Over the later years, a number of studies have evaluated regional and global LV function in small animals and found that the hearts in humans, rat and mice share many of the same systolic and diastolic properties, including EF, intramyocardial strain and twist (although myocardial *torsion* is very different, defined as twist per unit length, due to different heart lengths) (18-20). Although there are differences in e.g. regional motion patterns, cardiomyocyte properties (including force-frequency relationship) and resting heart rate between species that render findings in small animals in general not one-to-one transferable to human conditions (17), it is well-established that results from small-animal research can increase understanding of cardiac disease in humans. Also, the three species share homologs for the majority of their genes.

5.1.3 ANESTHESIA, PREPARATION AND MONITORING

Induction of Myocardial Infarction

To induce MI, the rats were anesthetized in an anesthesia chamber (64% N_2O, 32% O_2 and 4% isoflurane), and subsequently ventilated on a Zoovent ventilator through endotracheal intubation. Anesthesia was maintained by 65% N_2O, 32% O_2 and 2-3% isoflurane. Myocardial infarction was induced by left hemithoracotomy and ligation of the left coronary artery (LCA) by a 5.0 silk suture. The chest was closed and buprenorphine was given as postoperative analgesia. Sham operated rats underwent the same procedure except LCA-ligation.

ECHO and MRI Imaging

The animal preparation and monitoring procedures were the same in mice and rats during imaging. Anesthesia was induced in a chamber (ECHO: 64% N_2O, 32% O_2 and 4% isoflurane; MRI: 96% O_2 and 4% isoflurane), and maintained during imaging at 1-2% isoflurane in freely breathing animals.

During echocardiography, ECG was measured by electrodes embedded in the examination table. During MRI, ECG was monitored by subcutaneous electrodes in the front legs (rats) or in one front and one hind leg (mice). This signal was also used for triggering of the MRI acquisition.

Monitoring During MRI Examination

Since the animals were out-of-view for the operator during MRI experiments, **respiration** was monitored by placing an air pillow on the animal thorax (this was also used for gating of the acquisition to avoid respiration artifacts (198)). Also, **temperature** was monitored by a rectal probe, and body temperature was maintained by heated air using an automated feedback system.

Throughout all MRI experiments, these parameters were carefully monitored to ensure animal safety and depth of anesthesia. Due to lack of the opportunity for visual evaluation of animal welfare, this monitoring constituted a vital part of experimental procedure.

5.1.4 LIMITATIONS OF THE ANIMAL MODELS

Effect of Anesthesia

Animals were anesthetized during examination, using a mixture of oxygen and isoflurane in freely breathing animals. The level of isoflurane should always be carefully monitored and adjusted to provide an optimal depth of anesthesia. A standardized level of anesthesia is essential to reduce inter-animal variation that could otherwise mask important differences.

Light isoflurane anesthesia has been shown to provide stable sleep with minimal impact on cardiac function (199-202). However, during MRI experiments, which tended to be quite long-lasting, the potential cardiodepressive effect of isoflurane must be taken into account when analyzing results. As noted in the papers, the level of anesthesia was subject to small adjustment throughout experiments to keep the heart rate as constant as practically possible.

Anesthetized mice and rats rapidly lose body heat; and hypothermia compromises cardiac function. During MRI experiments, animal temperature was maintained using hot air, whose effect was controlled by a feedback system with a rectal probe measuring animal temperature. Nevertheless, during extended MRI acquisition there will be a pronounced variation in temperature, especially the first parts of acquisition until the body heat lost during preparation has been regained.

Other Limitations

In Paper III and IV, a rat model of MI was used. There are several limitations with this model:

- In the rats, coronary artery occlusion was performed in healthy young individuals, though in humans MI usually occurs in the elder.
- In the rats, the pericardium is compromised after surgery, causing a majority of the hearts to "stick" to the inside of the chest wall. Typically, this affects mainly the infarcted areas. If such an adhesion takes place, this inevitably alters the regional properties of the myocardium. Although this phenomenon also might occur in humans, it may limit the translational value of this model to the human condition of MI. This also highlights the importance of using control groups, which also have opened pericardium.
- The resulting infarct sizes vary and are difficult to predict, and increases intragroup variability.

Regardless of these limitations, however, important knowledge on the development of cardiac disease may still be gained from these models by carefully considering the implications of the above factors.

5.2 Magnetic Resonance Imaging

5.2.1 MRI Hardware and Software

All MRI experiments in this thesis was done on a 9.4T horizontal bore magnet (Agilent Technologies, Inc., USA) employing high-performance actively shielded gradient coils with optimized hardware eddy current compensation.

The MR system employed in the work with this thesis was very customizable. That is, the operator had little limits with respect to modification of the pulse sequences. In reality, this could be done by modifying the bread-and-butter sequences bundled with the MR system to accommodate the wishes and requirements defined by the operator.

5.2.2 ECG and Respiratory Gating

In cardiac MRI, synchronization of data acquisition to cardiac motion is essential (198). In all studies in this thesis, prospective cardiac triggering with respiration gating was employed. The R-peak of the ECG signal served as trigger for acquisition.

Respiratory gating was achieved by only allowing data acquired *between* respiration events to be recorded. Typically, respiratory motion occupied about 20-40% of the time available for acquisition, leading to an equivalent increase in experiment time.

5.2.3 CINE MRI

In Paper IV, LV volumes, infarct size and timing of valve events were quantified by use of cine MRI loops. The protocol used to acquire the data was identical to the PC-MRI protocol with the motion encoding gradients turned off, and with all gradient complexes first order nulled at the time of the readout echo (i.e. the sequence was flow compensated). Since the gradient requirement was less great than the equivalent motion encoded scans, the temporal resolution could be increased.

A stack of back-to-back slices were acquired covered the LV from base to apex. In post-processing, the LV endo- and epicardial borders were manually drawn in each slice at end systole and end diastole. LV intraventricular volumes at end diastole and end systole calculated from the epicardial masks and slice thickness. Likewise, LV myocardial volumes were found from endo- and epicardial masks.

An additional cine slice was oriented to visualize the mitral and aortic valve, allowing determination of the timing of their opening and closing relative the trigger signal.

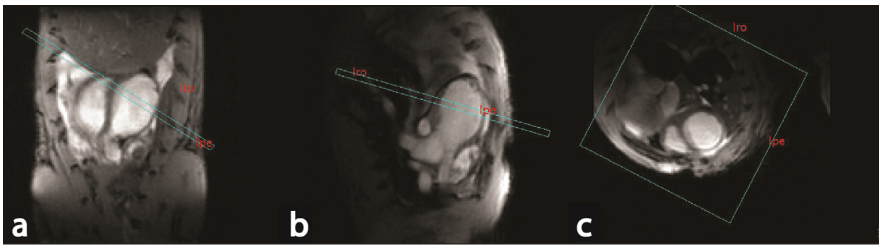

Figure 5.1 Planning of short-axis slices

This displays a screenshot from the MRI acquisition software, during a planning protocol (following the procedure described by Schneider et al. (60)). As seen here, MRI provides complete freedom in planning the acquisition. This illustrates an infarcted heart.

(**a**) The left and right ventricle is visible, and thinning due to the infarction is visible in the lateral wall of the LV.

(**b**) A slice normal to **a**, where the LV with both its atrium and aortic outflow tract are visible. In addition to being a scouting scan, this is an example of an orientation allowing evaluation of the timing of LV valve events.

(**c**) The mid-ventricular short-axis slice planned from **a** and **b**. The characteristic doughnut shape of the LV, along with the half-moon RV is visible. Myocardial thinning due to the infarction is evident in the anterolateral wall of the LV.

Note that these images are not "black-blood" prepared, resulting in bright blood signal.

5.3 PHASE CONTRAST MRI

5.3.1 PC-MRI PLANNING AND ACQUISITION

After animal preparation and placement in the isocenter of the scanner, the RF system had to be tuned and matched. For details on this, the reader is referred to Ref. (156). To improve field homogeneity, e.g. to reduce susceptibility artifacts, every MRI session included a comprehensive, fully automated shimming procedure (105) prior to data acquisition.

In all studies in this thesis, one (Paper I, II and III) or three (Paper IV) short-axis slices were acquired. For details on planning slices for assessment for cardiac

function in mice (and rats), the reader is referred to Schneider et al. (60). A screenshot of a planning situation is illustrated in Figure 5.1, clearly illustrating the inherent and appealing 3D nature of MRI.

The number of cine frames to be acquired after a trigger signal was detected was set by the operator, being a function of TR, heart rate and required cycle coverage.

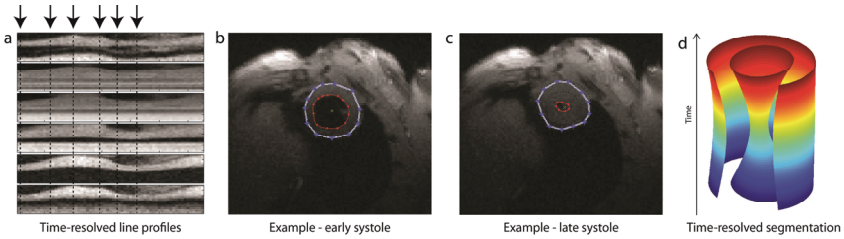

Figure 5.2 Segmentation of PC-MRI data

The segmentation of PC-MRI data in the present works is done the following way: Fist, the approximate center of the LV is marked by the operator in a short-axis image (not shown here). Then, a spatiotemporal map is generated (**a**), showing the line intensity profiles of a number of radial "spikes" from the LV center; this allows the operator to identify key time points in the cardiac cycle (arrows, dashed lines). This also provided the operator with a first impression of the quality of the data. After selection of a few time points, the endo- and epicardial borders are manually segmented at those times (**b**,**c**), and the masks are interpolated in the time domain to determine in-between frames (**d**). Note that a chunk of epicard has been removed in the last panel allowing visualization of the time-resolved endocardial mask.

5.3.2 Segmentation

Semi-automated segmentation of the PC-MRI data is illustrated in Figure 5.2, and described in detail in the papers.

Suboptimal segmentation would affect the data greatly; this would either exclude important data points (if the masks were too conservative) or include highly disturbing blood flow signal (if the masks were too liberal). While black-blood preparation reduced the impact of flow artifacts overlapping regions of interest, the reduction of signal magnitude in blood (seen in Fig 5.2a-c, compared to Figure 5.1) does *not* reduce the phase. This is an intrinsic property of phase-based imaging; as the signal magnitude in a pixel drops to zero, its phase becomes uniformly distributed noise in the interval $[-\pi,\pi]$ (see Figure 5.3).

5.3.3 Reconstruction of Myocardial Velocities

In each pixel, the Cartesian components of the velocity were reconstructed as described by Eq. 3.8, producing a 3D velocity vector. Motion due to bulk heart movement was removed by subtraction of the mean myocardial velocity in the two orthogonal in-plane directions. The velocity was subsequently decomposed into the cardiopolar coordinate system, constituting of a radial (in-plane; towards the in-slice center-of-mass of the LV), a circumferential (in-plane; normal to the radial) and a longitudinal component (through-plane), see Figure 3.5.

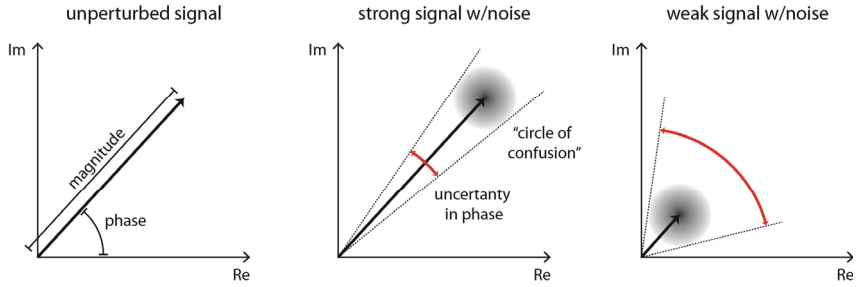

Figure 5.3 Effect of signal strength on phase noise
The MR signal is complex, and consists of a real (Re) and imaginary (Im) component. Random noise in complex MR imaging occurs independently in the two dimensions (203). This results in a "circle of confusion" surrounding the unperturbed signal, whose angular extent is dependent on signal magnitude. For the same noise properties, a strong signal results in a smaller uncertainty in the phase (red arc) than a weak signal. In the extreme case where the signal is zero (not shown), a unique phase cannot be defined and will be uniformly distributed in the whole range [-π,π].

5.3.4 MYOCARDIAL WORK

Paper IV involves calculation of myocardial work. The physical unit **work** is measured in Joules (J), and represents the transfer of mechanical energy from the muscle to the blood. Conversely, energy is the capacity for doing work. Physically, work is the product of force (newton) and distance (meter)[7], hence the unit[8].

Global myocardial work, also referred to as stroke work, may be calculated from the area of the LV pressure-volume loop, which reflects total myocardial oxygen consumption (204, 205). Accordingly, **regional myocardial work** is reflected by the force-segment length loop (206). Unfortunately, measurement of myocardial force is challenging, but LVP has been shown to be a suitable substitute for force, and the area of the LVP-dimension loop thus provides an index of regional myocardial work (56). This index, however, does not take into account the effects of the variable local curvature of the myocardium, and is thus not suitable for comparison within non-circular hearts (such as post-infarction) or between hearts of different size.

Work per Unit Surface

Recently, an approach of noninvasive measurement of regional myocardial work was described which allows calculation of regional myocardial work from myocardial strain, local curvature and LVP (6). By approximating the myocardium as a thin membrane, the surface tension at time *t* in a given region of LV could be estimated from the Young-Laplace equation, which accounts for curvature:

[7] Strictly speaking, the work is the product of the force and the distance acting in that very distance. So, if a force on an object is perpendicular to its motion, no work is done. For example, when you carry a heavy object horizontally at a constant speed, you actually do zero work on that object. If the motion and the force take place in opposite directions, the work is negative, such as when Superman stops a speeding subway train.
[8] Note that even if the unit of work, J, is indistinguishable from Nm, this is not used since Nm (newton-meter) is reserved for torque, where the *perpendicular* components of force and distance is multiplied. For work, the *parallel* components are multiplied.

$$\gamma(t) = \frac{LVP(t)}{\kappa(t)} \qquad [5.1]$$

where LVP(t) is the intraventricular pressure (in units Pa) in LV and κ(t) is the myocardial curvature (in units m^{-1}; the reciprocal of the often-cited *radius of curvature*) in the region in question, both at time *t*. Note that Eq 5.1 only accounts for curvature in one direction, i.e. it assumes a cylindical geometry; a simplification mirrored in Paper IV where only *circumferential* deformation is treated. In Ref. (6), LVP was found noninvasively by scaling a species-specific standard LVP curve to peak systemic pressure and the timing of the mitral and aortic valve events. Circumferential regional myocardial work per unit myocardial surface (in units J/m^2) could then be found from the area of the surface tension-strain loop.

Work per Unit Length and Volume

However, to compare the work done in regions within or between hearts with different sizes and geometries (such as the MI hearts), it is necessary to account for differences in surface area between regions of interest. This was achieved by multiplying the regional arc length at end-diastole[9] with circumferential regional work per unit surface, $cRMW_S$. Total work per unit length (where *length* refers to the through-plane/long-axis direction), labeled $cRMW_L$, could now be found. $cRMW_L$ equals the area of the surface tension-segment length loop. By summing $cRMW_L$ over well-defined anatomical regions in a given slice (such as the septum or the lateral wall), the work done per unit length could be compared between hearts.

Incorporating myocardial arc lengths allowed comparison of regional work between the MI hearts, whose geometry was very altered, with control animals.

Limitations in Work Calculation

The work calculated in Paper IV only incorporates circumferential strain and curvature, and includes thus no contributions from long-axis (through-plane) contraction or curvature.

The method is made potentially noninvasive by the usage of standard LVP curves. However, this curve does not incorporate variation following compromised hemodynamics, and will introduce uncertainties, especially in diastole, where LVP typically is affected significantly.

Moreover, the usage of the Young-Laplace equation (Eq. 5.1) poses several limitations. Importantly, it approximates the myocardium as an infinite thin membrane without inner forces, and assumes that there are no external forces that act on the myocardium. This may be problematic when the pericardium is opened after sham- and MI surgery; a majority of the hearts seemed to "stick" to the inside of the chest wall and experience constrictions in motion, and they are thus exposed to external

[9] The reason for multiplying with *end-diastolic* arc length rather than *time-resolved* arc length was that the temporal change in circumferential dimension already was accounted for by the inclusion of strain; i.e. end-diastolic arc length is the reference length for strain calculation. Thus, the difference becomes that $cRMW_S$ equals the surface tension-strain loop area, while $cRMW_L$ equals the surface tension-segment length loop area.

forces in certain regions. However, if regions subject to such "sticking" coincide with the infarction, the regional work done can be assumed to be zero, and thus allows such regions to be excluded from analysis. Another issue with the estimation of surface tension is that if the curvature approaches zero, which might happen e.g. in the septum in hemodynamically compromised hearts, the surface tension goes to infinity. So care must be taken if regions affected by these issues are to be analyzed.

Finally, valvular event timing, strain assessment and peak blood pressure measurements were done at different times (but within a few days). This is a potential major limitation with the study design employed; ideally all three recordings should have been collected concurrently. The consequence of this is two-fold:

- Any mismatch between valve and strain data due to variation in heart rate would potentially have large implications in work analysis since the timing of the valvular events was used to temporally normalize the standard LVP curve. Since LVP exhibits rapid variation in time, especially during isovolumic phases, a small offset of only a few milliseconds could create large errors in estimation of LVP. However, this error would only be in effect over a very short duration, and its overall impact is therefore expected to be small over the temporal integration. Nevertheless, as noted in the paper, an attempt to correct this was done by temporally fitting the datasets to exactly match the duration of the R-R-interval.
- The measurement of peak blood pressure is used for scaling the standard LVP curve, and mismatch here would over- or underestimate myocardial work.

5.3.5 Summary of Limitations and Challenges with PC-MRI

While PC-MRI might be a powerful and versatile technique, it is also shadowed by a bouquet of challenges, some of whom are already mentioned. We here provide a short summary.

Eddy current induced offsets in the phase pose a major challenge in phase-based imaging, with PC-MRI as no exception. The severity of their presence increases with field strength and spatiotemporal resolution. Paper I and II in this thesis focuses on the handling of eddy current induced errors. With the appropriate compensation techniques, these errors may be nearly completely eliminated.

Susceptibility artifacts such as loss of information in apex present another well-known issue in cardiac MRI. Due to abrupt change in magnetic susceptibility between the heart muscle and air, the local magnetic field is distorted which may lead to displacement artifacts or signal loss (90). Shimming and shorter pulse sequences reduces these artifacts (105).

Lengthy **acquisition time** is another concern in MRI. Compared to other imaging modalities like CT and echocardiography, MRI is very time-consuming. This limits the data yield obtainable during a single session, which in turn may limit the engagement of advanced MRI protocols in clinical routine due to the ever-present demand of high throughput. Additionally, since the acquisition of a given single dataset lasted for several minutes, variation in heart rate in the animals pose a problem, and is expected to cause artifacts in the images and low-pass filtering of the data. The

heart rate was continuously monitored, and level of anesthesia was subject to small adjustment throughout experiments to keep the heart rate as constant as practically possible. In practice, this was done with reasonable success; the intraanimal standard deviation in heart rate during the quite lengthy experiments in Paper III was less than 10 bpm. Slightly different R-R-duration between acquisitions in the same animal could be corrected by temporal normalization of the datasets in post-processing.

Flow artifacts may appear in several different ways. In myocardial PC-MRI, ghosting due to blood flow limits the reproducibility of myocardial velocities (68). The impact of this artefact may be reduced by using black-blood preparation (68, 186, 192) and/or, as presented in Paper III, a rotating FOV.

Suboptimal temporal resolution causes **low pass filtering** of the measured signal, attenuating high-frequency components of the velocity data. This is especially important when measurement of peak motion is to be done, and when the velocity fields are integrated to calculate displacement fields. In human applications, it has been recommended to cover the cardiac cycle with at least 60-70 frames to be able to accurately derive strain from velocity data or analyze strain-rate (25, 153). Until now, the highest temporal resolution in myocardial PC-MRI published in animal applications acquires about 25 frames per cycle. However, by incorporating the Fourier tracking technique, the effect of velocity low-pass filtering is greatly reduced in calculating tissue trajectories (92).

The quality of the PC-MRI data relies on **precise and reproducible segmentation**, which was done semi-automatically (Section 5.3.2). Care was taken when the endo- and epicardium were delineated, to not include blood or air pixels into the myocardial mask, and still include in the mask an as-large-as-possible fraction of myocardial pixels. To reduce possible blood signal contamination, an automated blood-signal suppression protocol was employed during post-processing. Here, the epi- and endocardial border zone pixels of the myocardial mask were analyzed one by one, and the pixel was removed from the myocardial mask (i.e. it was rebranded as non-myocardial) if its velocity deviated from the median of its myocardial neighbors by a user-set threshold. This was repeated iteratively until no more pixels were removed.

5.4 COMPUTER SIMULATIONS

In Paper I and II in this thesis, PC-MRI experiments of phantoms were simulated on a computer, using custom-written Matlab software (versions R2009b-R2012b). It served the purpose of demonstrating the theoretical foundation of the expected improvements presented in the two papers under idealized circumstances. It thus allowed examination of the impact of isolated factors on simulated PC-MRI acquisitions.

In both experiments, MRI acquisitions of phantoms were simulated (static cylinder in Paper I, rotating disk with static rim in Paper II). Also, eddy current induced baseline shifts played an important role in both simulations. An crude simplification in both these experiments was that this shift maps were randomly generated, obviously not corresponding to the actual situation, in which these maps are non-random functions of the gradient activity. However, we argued that the random maps fulfilled their purpose in 1) shifting the baseline phase with spatial heterogeneity (Paper I and

II), 2) being unique for each velocity encoding step (Paper I) and 3) producing fitting residuals after ECC (Paper I).

Nonetheless, computer simulations will always be a simplification of actual real-world experiments, so caution must be shown when interpreting results from such idealizations of the real world.

5.5 ECHOCARDIOGRAPHY AND CATHETERIZATION

5.5.1 ECHOCARDIOGRAPHY

Echocardiography also played a vital role in the studies in this thesis. It was used to stratify the animals prior to MRI examination (31), and served as a method (namely 2D speckle-tracking) for validation of the PC-MRI-derived strain in Paper III.

Standardized recordings, as well as skilled and unbiased operators, are critical factors to achieve high data quality in ECHO. All ECHO recordings in this thesis were performed by highly skilled operators with extensive experience on a Vevo 2100 (Visual Sonics, Canada) preclinical scanner with a 24 MHz transducer. General advantages and challenges of ECHO are discussed in more detail in Section 3.3.

5.5.2 BLOOD PRESSURE MEASUREMENT

In all animals included in Paper IV, intraventricular and aortic blood pressures (BP) were measured. For the cohort of animals also examined by MRI, these measurements were done within a few days after imaging.

Anesthesia was induced in an anesthesia chamber (64% N_2O, 32% O_2 and 4% isoflurane), and subsequently mask ventilated by a mixture of 98.5% O_2 and 1.5% isoflurane. A 1.4F Millar catheter was inserted retrogradely into the right common carotid artery and the LV cavity. Hemodynamic recordings of aortic and LV pressures were recorded at 1 kHz sampling rate. At a heart rate of 400 bpm, this resulted in about 150 data points covering the cardiac cycle.

Concurrent Valve Event and BP Assessment

In Paper IV, a standard LVP curve normalized to the length of the isovolumic phases was created through concurrent measurement of LVP and the timing of mitral and aortic valve events. Echocardiography combined with hemodynamic evaluation was performed six weeks after ligation of the left coronary artery. Concurrent with pressure readings, blood flow through the mitral and aortic valve was obtained by Doppler measurement. Aligned hemodynamic data, ECG and Doppler recordings were analyzed off-line.

Challenges with BP Measurements

The catheterization method may be subject to drift during experiment. Therefore, the baseline pressure was measured both prior to and after each recording, to assess potential drift during the session. Care was taken to minimize effects of temperature and depth of anesthesia (see also Section 5.1.4)

5.6 STATISTICS

In all four papers, either parametric (Student's t-test, one-way ANOVA) or non-parametric (Mann-Whitney U-test) tests were used to describe differences between groups. In Paper I, improvement in accuracy of the proposed PC-MRI encoding strategy was compared to two existing techniques, by evaluating results from computer simulations, phantom experiments and in vivo data from mice hearts. In Paper II, the performance of conventional and improved eddy current compensation was compared. In Paper III and IV, physiological and functional parameters of rats with MI were compared to sham-operated controls.

6 BRIEF SUMMARY OF MAIN RESULTS

This section briefly presents the main results of the individual papers, and that are important for the following discussion. The reader is referred to the individual papers for detailed results.

Paper I

Improved MR phase contrast velocimetry utilizing a novel nine-point balanced motion-encoding scheme with increased robustness to eddy current effects

The study reported in Paper I concerned the development of a novel approach to PC-MRI that allowed pushing the limits of achievable resolution in high-field MRI. The study proposed a new encoding strategy, labeled *nine-point balanced* encoding, designed to be more accurate than conventional methods in the presence of strong and rapidly changing magnetic gradients.

Computer simulations, phantom measurements and in vivo experiments demonstrated a significant improvement compared to conventional approaches in high-resolution application in mouse hearts. This study concluded that the nine-point balanced PC-MRI encoding strategy offers higher accuracy in velocity measurements due to increased robustness to eddy current effects, making it useful for settings where high spatiotemporal resolution is required.

Paper II

Unwrapping eddy current compensation: Improved compensation of eddy current induced baseline shifts in high-resolution phase-contrast MRI at 9.4 T

Paper II reports the second study in this thesis, and introduces an improved PC-MRI post-processing technique. When the gradient strengths are pushed to achieve optimal spatial and temporal resolution, eddy current generation can be so strong that the resulting phase shifts causes wrapping in the static-tissue (baseline) phase. Rendering conventional eddy current compensation inadequate, this study introduces an unwrapping ECC technique able to handle baseline phase discontinuities.

In high-resolution high-field PC-MRI, the presence of phase wrapping in static regions was demonstrated. Increasing the temporal resolution increased the presence of wrapping. The proposed unwrapping ECC technique was compared to conventional ECC, and performed significantly better by successfully eliminating phase discontinuities.

Paper III

Novel insight into the detailed myocardial motion and deformation of the rodent heart using high-resolution phase contrast MRI

In the third study in this thesis, reported in Paper III, the methodology presented in Paper I and Paper II is further developed and, as a proof-of-concept, applied in

normal and infarcted rat hearts. This study introduces the concept of a rotating field-of-view to reduce the impact of geometrically systematic artifacts.

Distinct alterations in global and regional function were demonstrated in the dysfunctional hearts, compared to control. This included reduced systolic peak motion, reduced global circumferential strain and increased heterogeneity in function as well as increased dyssynchrony. Intra- and interstudy variability were evaluated, and was low for both velocity and strain measurements (limits-of-agreement, radial motion: 0.01±0.32 cm/s and -0.06±0.75 cm/s; circumferential strain: -0.16±0.89 % strain and -0.71±1.67 % strain, for intra- and interstudy, respectively). Furthermore, strain derived from the PC-MRI data was validated against speckle tracking echocardiography, and found to be in excellent agreement ($r=0.95$, $p<0.001$; limits-of-agreement -0.02±3.92 % strain).

This study presents for the first time that PC-MRI enables high-resolution evaluation of in vivo myocardial strain in addition to myocardial motion and displacement in the rat heart.

Paper IV

Assessment of regional myocardial work in rats

In this fourth and last study of this thesis, a method for calculation of regional myocardial work, previously explored in large animals and humans using echocardiography, was adapted for use in small-animal research using MRI. In summary, measuring peak blood pressure and valvular events allows estimation of time-resolved LV pressure from a species-specific standard pressure curve, which again enables calculation of myocardial work from MRI-derived strain using the Young-Laplace equation. This study first establishes a standard LVP curve in rats, and subsequently applies the method to study alterations in circumferential regional myocardial work in the infarcted rat heart.

Myocardial work in infarcted regions was zero, as expected. However, stroke volume and stroke work was not decreased in the MI hearts. This suggested a compensatory increase in work performed by the viable myocardium. In the septum, work per unit length in the long-axis direction was indeed increased in MI animals compared to control (249.8 (46.7) vs 137.9 (14.3) mJ per unit long-axis length in a mid-ventricular slice; $p<0.001$). Work per unit mass was not different, so the increase in septal work was attributted to increased septal mass. Eccentric myocardial work during systole and isovolumic relaxation was also increased in the MI animals.

Paper IV demonstrated that PC-MRI constitutes, in combination with measurement of valvular events and peak blood pressure, a readily noninvasive technique for estimation of regional myocardial work.

7 RESULTS AND DISCUSSION

The availability of preclinical high-field MRI systems is in continuous growth, and will undeniably be a major contributor in studies employing e.g. small animal models of heart disease. Animal research provides matchless possibilities in studying the development and mechanisms of cardiac diseases, and techniques allowing reliable measurement of in vivo cardiac and regional myocardial function play a vital role. PC-MRI is thoroughly validated as a technique accurately measuring velocity, displacement and deformation of the myocardium, and offers a unique combination of the unrestricted geometry intrinsic to MRI and true 3D motion mapping. However, it might be challenging to achieve the optimal resolution required to capture the fine details of cardiac mechanics in small animals.

An overarching theme of this thesis was therefore to establish approaches allowing pushing the limits of the achievable resolution, both spatially and temporally, in PC-MRI imaging. Increased spatial and/or temporal resolution in MRI is accomplished by altering the gradient amplitudes and durations; higher spatial resolution requires *stronger* gradient, and higher temporal resolution requires *shorter* gradients. Unfortunately, stronger and more rapid gradients generate stronger eddy currents that inflict detrimental alterations in the measurements.

Paper I and II concern the pervasive challenge of eddy current induced artifacts in PC-MRI, and introduces approaches reducing the impact of these artifacts, ultimately allowing the employment of stronger gradients and therefore higher resolution than before. Paper III and IV investigate the ability of improved myocardial PC-MRI to assess regional motion/strain and work, respectively, in the rodent heart.

A rough overview of PC-MRI data acquisition and post-processing is illustrated in Figure 7.1, along with where the different papers in this thesis belong.

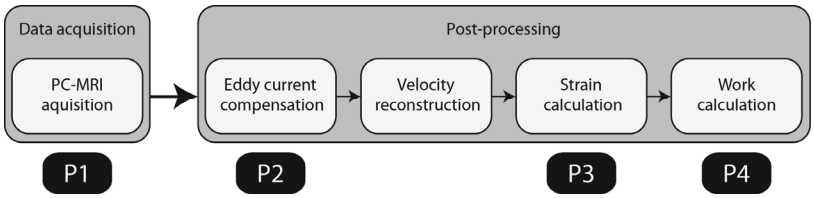

Figure 7.1 PC-MRI workflow overview
Rough overview of the workflow of a PC-MRI experiment, with markings denoting where the individual papers in this thesis belong. P1 = Paper I, and so on.

7.1 APPLICATION OF PRECLINICAL MYOCARDIAL PC-MRI

Although PC-MRI has been shown to be powerful and versatile in several research applications in humans (1, 90, 101, 104, 120, 121, 126, 127), to the best of our knowledge only two other groups have reported the use of myocardial PC-MRI in

small-animal research; Würsburg, Germany (105, 131, 132, 151) and Oxford, United Kingdom (17, 68)[10].

Using a 7T-system, **Streif et al.** (131) investigated the in-plane motion in a midventricular slice in normal and infarcted mouse hearts. **Weissman et al.** published a case report (132) also comparing healthy and infarcted mouse hearts using the same approach. **Nahrendorf et al.** (151) used the technique to investigate the altered myocardial velocities of a creatine kinase-deficient mouse.

Herold et al. (105) acquired three-directional motion in three short-axis slices in mice with (so far) unmatched spatial resolution using a 17.6 T system: 98 μm/pixel in-plane resolution and 0.6 mm slice thickness.

The most recent study, **Dall'Armellina et al.** (68) used a 9.4 T MR system equivalent to the system used in this thesis. They measured three-dimensional motion of mouse hearts in three LV levels with improved spatiotemporal resolution (200 μm/pixel, 4.6 ms per frame) which allowed detailed description of the waveform of the motion and transmural variation; using a ischemia-reperfusion model as a proof-of-principle application. This study is so far the only study reporting transmural variation in motion in small animals using PC-MRI. In addition, they were the first to employ black-blood contrast in preclinical myocardial PC-MRI, and documented the significance of suppressing blood flow to reduce flow artifacts.

Jung, Odening and Dall'Armellina et al. (17) compared the regional myocardial motion in mice (with data from study (68)), rabbits and humans (with data from study (1)), and revealed and described the different motion patterns between the species.

Three of the papers in this thesis reports parameters from myocardial PC-MRI in mice and rats, offering improved temporal resolution as well as a higher number of circumferential segments compared to previous work.

A quick comparison of principal sequence parameters is found in Table 7.1.

Table 7.1 Comparison of applications of myocardial PC-MRI in mice and rats
To date, only three groups (Würsburg (105, 131, 132, 151), Oxford (17, 68) and Oslo (93, 130)) have published studies on applications of myocardial PC-MRI in mice or rats.
*: This assumes 450 bpm in mice and 350 bpm in rats. SA = short axis.

Work	MR field (T)	Species	Spat.res (μm)	SA sectors	Temp.res (ms)	Frames/ cycle*
Streif et al. (131)	7.05	Mouse	234	4	~10	~13
Wiesmann et al. (132)	7.05	Mouse	234	-	~10	~13
Herold et al. (105)	17.6	Mouse	98	4	6	~22
Nahrendorf et al. (151)	7.05	Mouse	234	1	~10	~13
Dall'Armellina et al. (68)	9.4	Mouse	200	6/24	4.6	~29
Jung et al. (17)	9.4	Mouse	200	6/24	4.6	~29
Paper I (93)	**9.4**	**Mouse**	**200**	**32**	**3.5**	**~38**
Paper III (130)	**9.4**	**Rat**	**390**	**32**	**3.2**	**~54**
Paper IV (subm)	**9.4**	**Rat**	**390**	**32**	**2.9-3.2**	**~54-59**

[10] One of the studies was a collaborative effort between Freiburg, Germany and Oxford, UK. However, the mouse imaging was performed by the Oxford Group.

7.2 Optimizing PC-MRI Acquisition for Small Animal Applications

At the heart of optimizing myocardial PC-MRI for small animals is the aim to optimize spatial and temporal resolution; to be able to study both the intricate motion of the healthy heart and the complex and possibly subtle alterations in diseased hearts. Improved temporal resolution allows better peak detection due to reduced low-pass filtering and better evaluation of regional dyssynchrony (207). As mentioned in the Methods, a temporal resolution of 60-70 frames per cardiac cycle is recommended in humans to accurately being able to capture the fine motion of the heart (25, 153). So far, the data with highest resolution published in mice is less than half of this. In addition, optimized spatial resolution ensures the ability to discriminate function in different regions, and better opportunity to follow regional changes in function over time.

High-resolution myocardial PC-MRI will also potentially be of value in studies on e.g. spread of dysfunction after MI and regional function vs. local degree of fibrosis.

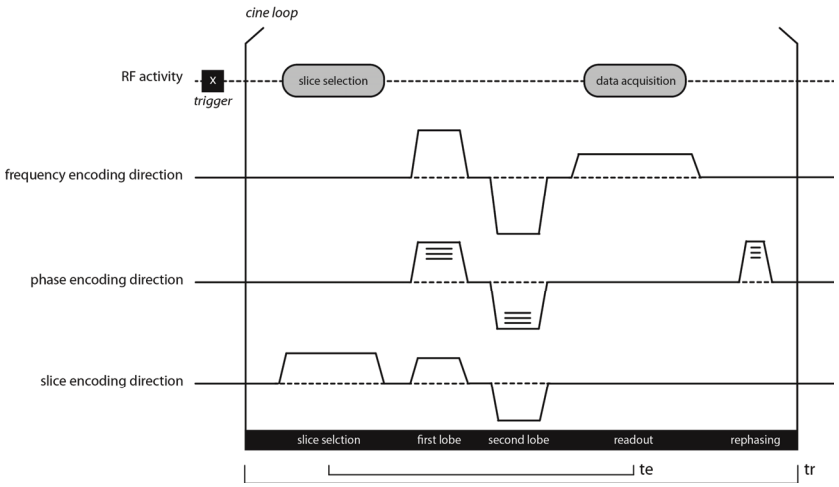

Figure 7.2 PC-MRI pulse sequence

Cartoon of the phase contrast MRI sequence. The first and second lobes in each encoding direction are sums of the spatial encoding (inherent of the gradient echo imaging sequence) and motion encoding (bipolar components). Amplitudes and timings are not exactly to scale. In the implementation of PC-MRI in this work, the spatial encoding could be first-order nulled (flow compensated) at the request of the operator. Echo and repetition times (TE/TR) are marked in the figure; note how TR equals the temporal resolution of the cine loop.

7.2.1 Development of PC-MRI Protocol

The pulse sequence employed in this thesis, with operator-selectable motion encoding and –compensation, was developed in-house based on a gradient echo cine sequence bundled with the system. Bipolar flow-encoding gradient were incorporated into the RF-spoiled gradient echo cine sequence, using a minimum-TE approach (208). Motion encoding could be turned off by the operator, and spatial-encoding

gradient complexes in all directions could be first moment-nulled (flow compensated) at echo time at the request of the operator. If the motion encoding gradients were turned off, the PC-MRI sequence essentially became a motion-compensated gradient echo cine sequence, which was used for all cine MRI in the work with the current thesis. The pulse sequence is illustrated in Figure 7.2.

The gradient waveforms and exact duration[11] were automatically calculated from four PC-MRI related inputs from the operator: venc, lobe duration, intergradient delays and encoding direction. Additional delays could also be prescribed by the operator, e.g. to allow some decay of eddy currents in the system after spatial and velocity encoding, before readout.

Since the whole trustworthiness of the measurements relied on precise calculation of gradients, care was taken to ensure the mathematics was correct, and that the prescribed gradients (specifically, their time-amplitude area and timing) were accurately carried out by the hardware. This was done on several levels;

1. The area of the calculated gradients were printed by the protocol on-screen during preparation of experiments, as they were dependent on a wide range of parameters
2. The actual gradient activity was measured using a four-channel digital oscilloscope, which allowed monitoring and quantification of the activity in the gradient hardware system
3. The resulting velocity measured was verified by use of a rotating phantom (Paper I)

7.2.2 INCREASING THE RESOLUTION

A well-established approach to accomplish high temporal resolution is to employ non-interleaved scans (209). This renders temporal resolution is simply equal to TR, and improving temporal resolution essentially becomes an issue of reducing TR. Striving to improve the spatiotemporal resolution of preclinical PC-MRI, an essential task therefore becomes to employ as strong and rapid gradients as possible, since (as described in the Theory section) resolution is directly related to the strength and duration of the magnetic gradients applied (105, 156).

- Optimal spatial resolution and velocity sensitivity is achieved by ensuring high time-amplitude areas of the encoding gradients.
- Increased temporal resolution demands shorter gradients, calling for even stronger gradients to achieve the same time-amplitude area.

Hardware Aspects

Progress in MR technology over the years has allowed the application of advanced protocols in small-animal research.

There is, as would be expected, an upper limit in the gradient system for how strong the gradients can be, and how quickly they can reach their maximum value. Another limiting factor is the gradient duty cycle, a limiting parameter related to the

[11] The actual durations of the gradients could only take certain values depending on its amplitude; thus it would differ ever so slightly (in the order of a few microseconds) to the user-prescribed duration. Since the first moment of the gradients, and thus velocity encoding, was directly a function of gradient timing, care had to be taken to ensure precise velocity encoding.

fraction of the time the gradients may be active without overheating. Together, these factors define the boundaries of how high resolution that is theoretically obtainable in a given system.

In the current thesis, no modifications in the actual hardware were done, so the work was not intended to extend the operating limits of the apparatus. Rather, we sought to find ways to be able to push the system towards it operating limits—and handle the consequences of this.

Resulting Resolution

The spatial resolution of the raw MRI data in the mice experiments in this thesis (Paper I) were not higher than previously published studies by Herold et al. (105) and Dall'Armellina et al. (68). The papers in the thesis demonstrate, however, improved temporal resolution without compromised spatial resolution in mice (Table 7.1). In addition, the studies in this thesis performed analysis on smaller regions than before, so the actual spatial resolution in the data reported was improved.

No other studies have, to our knowledge, applied myocardial PC-MRI in rats (as were done in Paper III and IV), so no study can serve as a comparison. But since rat hearts generally are larger and their beating frequency lower than mouse hearts, e.g. the number of frames per cycle (last column, Table 7.1) is considerably higher than previously reported in rodents.

7.2.3 Eddy Currents: Facing the Consequences of Improved Resolution

As mentioned in the Theory section, stronger and quicker gradients cause stronger eddy currents, which may results in severe baseline phase shifts (156). This renders the generation of eddy currents one of the most pressing challenges in high-resolution PC-MRI, since they have highly detrimental effects on the measurements. A predominant theme for Paper I and Paper II was thus to manage the increased presence of eddy current induced errors in the baseline phase following the considerably higher gradient activity that accompanies increased resolution (162, 165, 179, 180, 182, 183).

In all the papers in this thesis, a semi-automated spatially-specific ECC method without the need for additional scans was incorporated, described in details in Ref. (179). In short, it relies on the identification of static tissue from the temporal standard deviation of image pixels, and subsequent calculation and subtraction of a best-fit correction map. In this work, ECC was done after Fourier transforming (210) and multicoil reconstruction (211), but prior to velocity reconstruction.

Improved Efficiency of ECC

Paper I uses the conventional ECC approach (179). It demonstrates that increasing the number of encoding directions, i.e. the number of unique acquisitions of the motion, offers improved correction of baseline errors. The balanced nine-point encoding strategy, as was applied throughout all studies in this thesis, is an extension of the balanced five-point scheme where *eight* encoded scans plus a reference scan are acquired, spanning the corners of a cube. The dynamic range between the methods is identical. The balanced nine-point method offers improved accuracy compared to

previous approaches (175, 177) in measuring myocardial motion in mice. In Paper I, we argue that this is due to improved efficiency of the eddy current compensation. This allows the employment of stronger and more rapid gradients, ultimately increasing the spatiotemporal resolution (105).

Improved ECC

However, the conventional ECC is inadequate if the eddy currents are sufficiently strong to produce discontinuities in the baseline phase due to phase wrapping; this is reflected by the aim for the second study in this thesis. Paper II introduces a new preconditioning step to ECC, resulting in unwrapping ECC. This improved version of ECC was applied in Paper III and IV.

The challenge of baseline phase wrapping (i.e. discontinuities) due to severe eddy current induced baseline shifts is first introduced in Paper II, along with a technique to handle it. No study has previously, to our knowledge, reported such wrapping in the baseline phase in PC-MRI. There are probably two reasons for this. First, the majority of applications of PC-MRI have been developed to evaluate blood flow. As mentioned, this requires weaker gradients and consequently induces less eddy currents. Second, we have pushed the temporal resolution without compromised spatial resolution and thereby employed stronger and more rapid gradients than any other study (see Table 7.1).

The methodology presented in Paper I and II were shown to provide improved accuracy in the presence of strong eddy currents compared to conventional approaches, thus allowing further improvement of the resolution in future applications.

7.2.4 Rotating FOV: Reducing Impact of Flow Artifacts

Beat-to-beat variations in blood flow generates ghosting in the phase encoding direction, causing errors that are spatially dependent in the velocity measurements in the myocardium (21) and has been shown to affect the measurements of absolute myocardial velocities (68). Black blood contrast has been demonstrated to be beneficial in myocardial PC-MRI, both in humans (186, 192) and in mice (68), as well as when using MR tagging in mouse hearts (212). However, we demonstrate in Paper III that even after black-blood preparation, some residual artifacts might still remain in the phase-encoding direction (Figure 1, Paper III). The rotating FOV presented in this paper reduces the impact of such errors in regional analysis through averaging multiple acquisitions where the orientation of the phase-encoding direction is varied. As noted in Paper III, this only applies to Cartesian imaging. Other acquisition strategies, such as spiral acquisition (207), are faced with other manifestations of motion artifacts not addressed in this thesis.

A challenge with black-blood preparation is that it occupies valuable time in the sequence. In small-animal applications, a black-blood preparation complex occupies 10-20 ms of the cycle and thus either reduces cycle coverage (68) or leads to a doubling of the experiment time (130).

7.2.5 Additional Optimization

Overshoot

In all PC-MRI experiments in this thesis, as well as the valve cine data, more than 100% of the cardiac cycle was covered (151). This is referred to as overshoot, and was achieved by prescribing a cine train whose duration exceeded the R-R-interval. This was a necessary and rewarding in that it 1) guaranteed complete coverage of the whole cardiac cycle in combination with prospective gating and black-blood preparation, 2) allowed some decay of the currents in the ECG wires, thus improved the reliability of R-peak detection and 3) it allowed retrospective calculation of the mean heart rate at the time of experiment.

Improved Respiration Gating

Since prospective ECG-triggering with respiration gating (198) was used, a subtle (but important) optimization step was implemented: a limit was applied to how large fraction of the time between respiration events that were actually accepted for acquisition. This improved data quality substantially, since it avoided the situation where a trigger signal would be transmitted to the acquisition system immediately before a respiration event occurs, thus "allowing" acquisition during respiration.

7.2.6 The Cost of Increasing Resolution

One of the unavoidable trade-offs in MR is between data quality and acquisition time. As discussed in Paper I, the nine-point obviously increases scan time compared to four- or five-point encoding. However, achieving satisfactory SNR in small-animal applications renders employment of signal averaging (NA>1) necessary (that is, multiple acquisition of the same signal to improve signal-to-noise ratio). In Paper I, we demonstrate that the nine-point scheme with NA=n offers a decrease in scan time but still improves measurement accuracy compared to the five-point scheme with NA=2n and the four-point scheme with NA=3n. Thus, in comparison to earlier implementations of murine myocardial PC-MRI where NA>2 is used (105, 131, 151), the nine-point approach would actually be beneficial with respect to acquisition time. This is not the case in the latest application of myocardial PC-MRI in mice (68), whose four-point encoding with NA=2 renders the acquisition time about 11% lower than would have been possible with nine-point.

Although no myocardial PC-MRI studies on the rat have been published, the acquisition time in Paper III was comparable to previously reports on MR-based strain measurement (81, 213).

Another factor increasing acquisition time is the choice of "overshooting" the cardiac cycle, in that the PC-MRI cine train covered more than 100% of the R-R-interval. However, as discussed in the papers, this allowed complete coverage of the whole phase (including diastole) in combination with black-blood preparation, and improved the reliability of ECG-triggering by allowing decay of currents induced in the ECG wires by gradient activity.

Nevertheless, all MR examinations reported in this thesis were considerably more time-consuming than similar echocardiography examinations, although the data yield would be different. Depending on study design and experimental needs, the

trade-off between data yield and acquisition time must be considered. In this parallel imaging was not employed, which potentially reduces the acquisition time considerably (30, 108, 109).

7.3 Optimized Analysis of Regional Myocardial Function

In this section, some of the aspects of optimizing post-processing are discussed.

7.3.1 Velocity

In this thesis, the myocardial PC-MRI protocol was applied in mice (Paper I) and rats (Paper III and IV), and revealed that peak radial motion was about half in mice compared to rats. The waveforms of radial motion in normal humans, rats and mice are very similar with easily discernible systolic, isovolumic relaxation and diastolic phases (68, 101, 130), although the peak velocities are different (Table 7.2). The short but distinct biphasic radial motion pattern in early diastole has previously been emphasized as an example of a brief complex motion pattern in humans that requires high-temporal resolution to capture (101). This pattern is easily discernible in myocardial PC-MRI data in both mice (Paper I) and rats (Paper III), indicating that the temporal resolution employed is sufficient to capture very fine details of cardiac motion.

7.3.2 Displacement

Temporal integration of velocity, having units distance per time, results in a measure of displacement. Integration of velocity plays an important role in Paper I, III and IV; however it serves very different purposes.

In Paper I, it was used at a tool for evaluating the accuracy of the proposed nine-point method. Here, no extra steps were taken to improve trajectory calculation since we intended to examine the presence of errors in the velocity data.

In Paper III and IV, however, velocity integration played a fundamental role in calculation of myocardial strain. In these papers, the trajectory of each myocardial pixel was calculated using a Fourier corrected forward-backward motion tracking technique (91, 92, 95), providing accurate assessment of displacement from velocity data. Since the imaging volume was static in the laboratory system, slightly different parts of the myocardium was included in end-diastole and end-systole. This motivated our choice of extending the motion tracking technique to include end-systole as a temporal origin, in addition to end-diastole. This provided two unique representations of the displacement field, and analysis revealed that the intra- and interstudy limits-of-agreements were improved when this approach was employed.

7.3.3 Strain

In Paper III and IV, the Lagrangian strain in the circumferential direction (ε_{CC}) was calculated by comparing the position of neighboring regions over time (Eq. 3.14). As noted in Paper III, our method of calculating strain is rather simple compared to more advanced approaches such as a spline-based deformation analysis (214). However, validation, analysis of inter- and intrastudy variability and excellent agreement

with the literature of the results advocates our approach as suitable for calculating circumferential strain.

The work in this thesis have, as many previous studies (85, 147, 194-197), focused on circumferential strain. A limitation of solely focusing on the circumferential component of strain is that it does not enable calculation of the strain tensor, and relies on precise definition of cardiac geometry prior to strain calculation (14).

Validation of PC-MRI Strain

PC-MRI itself has been validated to accurately measure velocity (90), displacement (94, 95) and deformation (96) of the myocardium. It has been used to calculate myocardial strain in dogs (90) and humans (97) and compared theoretically to MR tagging (215).

However, the work in Paper III and IV was, to our knowledge, the first studies employing high-resolution velocity data to calculate myocardial strain in rodents. We therefore needed to validate this to a well-established method, and our choice fell on speckle-tracking echocardiography (2D-STE), which itself has been validated against tagging MRI, sonomicrometry and tissue Doppler echocardiography (216) and compared to displacement-encoded MRI in mice (217, 218). We found that strain derived from PC-MRI and 2D-STE agreed excellently. PC-MRI-derived strain also had low inter- and intrastudy variability.

When validating the strain calculation from PC-MRI with 2D-STE, we found it appropriate to compare temporally-resolved global values rather than regional values. The reason for this was that since our object was to reveal any possible systematic difference between the modalities, we wanted the variability within each method to be as optimal as possible. If we were to use regional strain from speckle-tracking and compare it to corresponding regions in MRI, we believe that the increased uncertainty in the measurements due to differences in segmentation would possibly reduce the power of the validation in detecting possible systematic differences between echo- and MRI-derived strain.

Consistency with Literature

As described in Paper III, our findings on circumferential strain in rat hearts agreed well with other studies employing MR tagging (20, 219, 220) and HARP (213), however Paper III had considerably higher temporal resolution (>50 temporal frames per cycle vs. 12-25). All studies report maximum circumferential strain at the mid-ventricular level to be 19-23% (Table 7.2).

We found, initially somewhat surprisingly, a quite prominent heterogeneity in regional circumferential strain in sham-operated hearts. However, we soon found that this has also been documented earlier in a study employing 2D-STE (67). There might be several reasons for this;

- The sham-operated animals have had the pericardium opened. This can cause the epicardium to "stick" to the inside of the chest wall, which will provide an external force restricting the intrinsic freedom of the cardiac motion.
- The zones in the LV myocardium where the RV is attached experiences additional forces due to contraction and passive forces in the RV myocardium and lumen.

Similarly, it has been shown in human hearts that circumferential strain is indeed not completely homogenous around the circumference; it is greater in anterior and lateral regions than in posterior regions at all levels in the heart (48, 221).

Table 7.2 Comparison of peak radial velocities and circumferential strain between species

Velocity measured by PC-MRI at a mid-ventricular level in normal subjects. From (1, 68, 93, 101, 119, 130, 207). Circumferential strain measured by MRI at a mid-ventricular level. From (16, 19, 20, 69, 81, 213, 219, 220, 222, 223).

Species	Peak systole (cm/s)	Peak diastole (cm/s)	Circ. strain (%)
Humans	2.4-3.5	3.6-5.1	20-23
Rats	2.2	2.7	19-23
Mice	0.8-1.3	1.6-1.8	15-17

7.3.4 WORK

In Paper IV, the regional work in MI hearts was compared to sham-operated controls. Performed work was, as expected, reduced in the lateral wall of the MI hearts (containing both viable and infarcted tissue); and work done in the infarcted regions alone was zero. The total work done by the entire septum, however, was *increased* in the MI hearts. Moreover, stroke volume and estimated stroke work (from mean work per unit length in each heart multiplied with the heart length) was preserved in the MI hearts, and this agreed well with the finding of increased work in the viable myocardium in infarcted hearts. Thus, we were able to detect a compensatory increase in work in the viable myocardium by use of PC-MRI in combination with measurement of peak systemic pressure.

The stroke work done in the septum *per unit myocardial mass* was found to be not different between groups, but the septal volume was increased, consistent with our finding on increased work done by this region.

As discussed in the paper, we found work per unit myocardial mass in rats to be higher than previously reported values in larger animals (56, 224). However, our finding was consistent between the two different approaches for calculating stroke work per volume; using data from either cine MRI or PC-MRI. On that note; somewhat surprisingly, however, was the fact that total stroke work calculated from circumferential strain only (mean PC-MRI derived work per unit length multiplied with heart length) was more or less equal to work form dimension-independent data (mean systolic LVP multiplied with cine MRI-derived stroke volume). An explanation of this is that the consequence of ignoring both long-axis strain and –curvature is expected to contribute in opposite directions, i.e. this simplification concurrently both over- and underestimate the actual work and ultimately the error is reduced.

7.4 APPLICABILITY OF THE PRESENT RESULTS TO CLINICAL USAGE

Although the work in this thesis is motivated by the need for improved resolution in small-animal imaging, there are no fundamentally technical differences between pre-

clinical and clinical MRI; and the methodological results in this thesis is in principle applicable to human MRI usage. Paper I and II presents improved handling of eddy current artifacts, which might allow improved resolution and/or sensitivity in also in human applications. Paper III and IV present the methods for calculation of myocardial strain and work, respectively, from PC-MRI data, both completely independent on species.

Still, there are other important issues that must be concidered when translating MRI methodology from preclinical to human applications; including achieving acceptable acquisition times and acceptable exposure to gradient- and RF activity.

7.5 THE FUTURE IS THREE-DIMENSIONAL

The work in this thesis concerns the acquisition and analysis of three-directional velocity on a 2D grid (a slice). There are several limitations by doing this; first and foremost we are not able to accurately capture the complex three-directional motion and create true 3D motion paths (225). Second, the slices are stationary in the laboratory system meaning that slightly different parts of the myocardium are included at different phases in the cardiac cycle. Third, the slices are defined in the acquisition process, and the data relies on

A natural extension of the work in this thesis is to develop a sequence able to capture true 3D data, that is, three-directional three-dimensional motion. While flow-quantification PC-MRI has seen a rapid development over the years towards fast, comprehensive acquisition of true 3D data (172, 173, 226, 227), 3D myocardial PC-MRI has to the author's knowledge only been used once by Kvitting et al. (13), in a human study.

When established, it is likely that 3D PC-MRI using acceleration methods such as *vastly undersampled isotropic-voxel radial projection imaging* (VIPR) (172, 226) or spiral acquisition (167) will come to play important roles in the study of the healthy and diseased myocardium.

The nine-point encoding scheme introduced in Paper I and the unwrapping ECC technique presented in Paper II are readily applied to 3D acquisitions; both conventional and accelerated approaches. The myocardial strain and work calculation from Papers III-IV are extendable to 3D data with only minor modifications.

8 CONCLUSIONS

The main conclusion of this thesis is the following:

PC-MRI is a versatile and accurate method able to describe regional motion, deformation and work of the myocardium in small animals with high spatio-temporal resolution.

Reflecting the four aims and papers in this thesis, the sub conclusions are the following:

1. Employing nine-point balanced PC-MRI encoding strategy offers higher accuracy in velocity measurements due to increased robustness to eddy current effects through improved efficiency of eddy current compensation.

2. Baseline wrapping occurs in high-field, high-resolution PC-MRI if the resolution is pushed, and conventional ECC fails to properly correct such errors. An improved unwrapping ECC technique significantly improves correction of eddy current induced errors in phase contrast MRI.

3. Through a combination of optimized slice planning, acquisition parameters and post-processing, exploration of the complex spatiotemporal pattern of in vivo motion and circumferential strain in the healthy and dysfunctional rat heart is feasible.

4. PC-MRI strain in combination with peak blood pressure and LV valve event quantification allows calculation of regional myocardial work in the rat heart, constituting a potentially noninvasive technique for evaluation of regional myocardial work in rodent hearts.

9 REFERENCES

1. Foll D, Jung B, Schilli E et al. **Magnetic resonance tissue phase mapping of myocardial motion: new insight in age and gender**. Circ Cardiovasc Imaging 2010;3:54-64.

2. Moore CC, McVeigh ER, Zerhouni EA. **Quantitative tagged magnetic resonance imaging of the normal human left ventricle**. Top Magn Reson Imaging 2000;11:359-371.

3. Wang H, Amini AA. **Cardiac motion and deformation recovery from MRI: a review**. IEEE Trans Med Imaging 2012;31:487-503.

4. Quinones MA, Gaasch WH, Alexander JK. **Influence of acute changes in preload, afterload, contractile state and heart rate on ejection and isovolumic indices of myocardial contractility in man**. Circulation 1976;53:293-302.

5. Urheim S, Edvardsen T, Torp H, Angelsen B, Smiseth OA. **Myocardial strain by Doppler echocardiography. Validation of a new method to quantify regional myocardial function**. Circulation 2000;102:1158-1164.

6. Russell K, Eriksen M, Aaberge L et al. **A novel clinical method for quantification of regional left ventricular pressure-strain loop area: a non-invasive index of myocardial work**. Eur Heart J 2012;33:724-733.

7. Prinzen FW, Hunter WC, Wyman BT, McVeigh ER. **Mapping of regional myocardial strain and work during ventricular pacing: experimental study using magnetic resonance imaging tagging**. J Am Coll Cardiol 1999;33:1735-1742.

8. van Oosterhout MF, Prinzen FW, Arts T et al. **Asynchronous electrical activation induces asymmetrical hypertrophy of the left ventricular wall**. Circulation 1998;98:588-595.

9. Hess AT, Zhong X, Spottiswoode BS, Epstein FH, Meintjes EM. **Myocardial 3D strain calculation by combining cine displacement encoding with stimulated echoes (DENSE) and cine strain encoding (SENC) imaging**. Magn Reson Med 2009;62:77-84.

10. Dalen H, Thorstensen A, Aase SA et al. **Segmental and global longitudinal strain and strain rate based on echocardiography of 1266 healthy individuals: the HUNT study in Norway**. Eur J Echocardiogr 2010;11:176-183.

11. Moore CC, Lugo-Olivieri CH, McVeigh ER, Zerhouni EA. **Three-dimensional systolic strain patterns in the normal human left ventricle: characterization with tagged MR imaging**. Radiology 2000;214:453-466.

12. Cupps BP, Bree DR, Wollmuth JR et al. **Myocardial viability mapping by magnetic resonance-based multiparametric systolic strain analysis**. Ann Thorac Surg 2008;86:1546-1553.

13. Kvitting JP, Ebbers T, Engvall J, Sutherland GR, Wranne B, Wigstrom L. **Three-directional myocardial motion assessed using 3D phase contrast MRI**. J Cardiovasc Magn Reson 2004;6:627-636.

14. Selskog P, Heiberg E, Ebbers T, Wigstrom L, Karlsson M. **Kinematics of the heart: strain-rate imaging from time-resolved three-dimensional phase contrast MRI**. IEEE Trans Med Imaging 2002;21:1105-1109.

15. McCulloch A, Waldman L, Rogers J, Guccione J. **Large-scale finite element analysis of the beating heart**. Crit Rev Biomed Eng 1992;20:427-449.

16. Epstein FH. **MRI of left ventricular function**. J Nucl Cardiol 2007;14:729-744.

17. Jung B, Odening KE, Dall'armellina E et al. **A quantitative comparison of regional myocardial motion in mice, rabbits and humans using in-vivo phase contrast CMR**. J Cardiovasc Magn Reson 2012;14:87.

18. Henson RE, Song SK, Pastorek JS, Ackerman JJ, Lorenz CH. **Left ventricular torsion is equal in mice and humans**. Am J Physiol Heart Circ Physiol 2000;278:H1117-H1123.

19. Epstein FH. **MR in mouse models of cardiac disease**. NMR Biomed 2007;20:238-255.

20. Liu W, Ashford MW, Chen J et al. **MR tagging demonstrates quantitative differences in regional ventricular wall motion in mice, rats, and men**. Am J Physiol Heart Circ Physiol 2006;291:H2515-H2521.

21. Simpson RM, Keegan J, Firmin DN. **MR assessment of regional myocardial mechanics**. J Magn Reson Imaging 2012.

22. Dickstein K, Cohen-Solal A, Filippatos G et al. **ESC guidelines for the diagnosis and treatment of acute and chronic heart failure 2008: the Task Force for the diagnosis and treatment of acute and chronic heart failure 2008 of the European Society of Cardiology. Developed in collaboration with the Heart Failure Association of the ESC (HFA) and endorsed by the European Society of Intensive Care Medicine (ESICM)**. Eur J Heart Fail 2008;10:933-989.

23. Tee M, Noble JA, Bluemke DA. **Imaging techniques for cardiac strain and deformation: comparison of echocardiography, cardiac magnetic resonance and cardiac computed tomography**. Expert Rev Cardiovasc Ther 2013;11:221-231.

24. Bild DE, Bluemke DA, Burke GL et al. **Multi-ethnic study of atherosclerosis: objectives and design**. Am J Epidemiol 2002;156:871-881.

25. D'hooge J, Heimdal A, Jamal F et al. **Regional strain and strain rate measurements by cardiac ultrasound: principles, implementation and limitations**. Eur J Echocardiogr 2000;1:154-170.

26. Ross J, Jr. **Regional myocardial function and microvascular dysfunction. Does the alternate cascade represent ischemia?** Cardiologia 1999;44:797-799.

27. Swift F, Franzini-Armstrong C, Oyehaug L et al. **Extreme sarcoplasmic reticulum volume loss and compensatory T-tubule remodeling after Serca2 knockout**. Proc Natl Acad Sci U S A 2012;109:3997-4001.

28. Swift F, Birkeland JA, Tovsrud N et al. **Altered Na+/Ca2+-exchanger activity due to downregulation of Na+/K+-ATPase alpha2-isoform in heart failure**. Cardiovasc Res 2008;78:71-78.

29. Mork HK, Sjaastad I, Sejersted OM, Louch WE. **Slowing of cardiomyocyte Ca2+ release and contraction during heart failure progression in postinfarction mice**. Am J Physiol Heart Circ Physiol 2009;296:H1069-H1079.

30. Schneider JE, Lanz T, Barnes H et al. **Ultra-fast and accurate assessment of cardiac function in rats using accelerated MRI at 9.4 Tesla**. Magn Reson Med 2008;59:636-641.

31. Sjaastad I, Sejersted OM, Ilebekk A, Bjornerheim R. **Echocardiographic criteria for detection of postinfarction congestive heart failure in rats**. J Appl Physiol 2000;89:1445-1454.

32. Finsen AV, Christensen G, Sjaastad I. **Echocardiographic parameters discriminating myocardial infarction with pulmonary congestion from myocardial infarction without congestion in the mouse**. J Appl Physiol 2005;98:680-689.

33. Sjaastad I, Birkeland JA, Ferrier G et al. **Defective excitation-contraction coupling in hearts of rats with congestive heart failure**. Acta Physiol Scand 2005;184:45-58.

34. Brattelid T, Qvigstad E, Birkeland JA et al. **Serotonin responsiveness through 5-HT2A and 5-HT4 receptors is differentially regulated in hypertrophic and failing rat cardiac ventricle**. J Mol Cell Cardiol 2007;43:767-779.

35. Vistnes M, Waehre A, Nygard S et al. **Circulating cytokine levels in mice with heart failure are etiology-dependent**. J Appl Physiol 2010.

36. Pfeffer JM, Pfeffer MA, Braunwald E. **Influence of chronic captopril therapy on the infarcted left ventricle of the rat**. Circ Res 1985;57:84-95.

37. Pfeffer MA, Pfeffer JM, Fishbein MC et al. **Myocardial infarct size and ventricular function in rats**. Circ Res 1979;44:503-512.

38. Nahrendorf M, Hiller KH, Hu K, Ertl G, Haase A, Bauer WR. **Cardiac magnetic resonance imaging in small animal models of human heart failure**. Med Image Anal 2003;7:369-375.

39. Land S, Niederer SA, Aronsen JM et al. **An analysis of deformation-dependent electromechanical coupling in the mouse heart**. J Physiol 2012;590:4553-4569.

40. Hougen K, Aronsen JM, Stokke MK et al. **Cre-loxP DNA recombination is possible with only minimal unspecific transcriptional changes and without cardiomyopathy in Tg(alphaMHC-MerCreMer) mice**. Am J Physiol Heart Circ Physiol 2010;299:H1671-H1678.

41. Carmeliet P, Collen D. **Transgenic mouse models in angiogenesis and cardiovascular disease**. J Pathol 2000;190:387-405.

42. Smits BM, Mudde JB, van de Belt J et al. **Generation of gene knockouts and mutant models in the laboratory rat by ENU-driven target-selected mutagenesis**. Pharmacogenet Genomics 2006;16:159-169.

43. Hamra FK, Gatlin J, Chapman KM et al. **Production of transgenic rats by lentiviral transduction of male germ-line stem cells**. Proc Natl Acad Sci U S A 2002;99:14931-14936.

44. Schneider JE, Stork LA, Bell JT et al. **Cardiac structure and function during ageing in energetically compromised Guanidinoacetate N-methyltransferase (GAMT)-knockout mice - a one year longitudinal MRI study**. J Cardiovasc Magn Reson 2008;10:9.

45. Schneider JE, Bose J, Bamforth SD et al. **Identification of cardiac malformations in mice lacking Ptdsr using a novel high-throughput magnetic resonance imaging technique**. BMC Dev Biol 2004;4:16.

46. Schneider JE, McAteer MA, Tyler DJ et al. **High-resolution, multicontrast three-dimensional-MRI characterizes atherosclerotic plaque composition in ApoE-/- mice ex vivo**. J Magn Reson Imaging 2004;20:981-989.

47. Karamitsos TD, Francis JM, Myerson S, Selvanayagam JB, Neubauer S. **The role of cardiovascular magnetic resonance imaging in heart failure**. J Am Coll Cardiol 2009;54:1407-1424.

48. Shehata ML, Cheng S, Osman NF, Bluemke DA, Lima JA. **Myocardial tissue tagging with cardiovascular magnetic resonance**. J Cardiovasc Magn Reson 2009;11:55.

49. Helm RH, Leclercq C, Faris OP et al. **Cardiac dyssynchrony analysis using circumferential versus longitudinal strain: implications for assessing cardiac resynchronization**. Circulation 2005;111:2760-2767.

50. Shah DJ, Judd RM, Kim RJ. **Technology insight: MRI of the myocardium**. Nat Clin Pract Cardiovasc Med 2005;2:597-605.

51. Bilchick KC, Dimaano V, Wu KC et al. **Cardiac magnetic resonance assessment of dyssynchrony and myocardial scar predicts function class improvement following cardiac resynchronization therapy**. JACC Cardiovasc Imaging 2008;1:561-568.

52. Reichek N. **MRI myocardial tagging**. J Magn Reson Imaging 1999;10:609-616.

53. Gorcsan J, III. **Is the magnet a better crystal ball for predicting response to cardiac resynchronization therapy?** JACC Cardiovasc Imaging 2008;1:569-571.

54. Oyenuga OA, Onishi T, Gorcsan J, III. **A practical approach to imaging dyssynchrony for cardiac resynchronization therapy**. Heart Fail Rev 2011;16:397-410.

55. De Filippo M, Julsrud P, Araoz P et al. **MRI evaluation of myocardial viability**. Radiol Med 2006;111:1035-1053.

56. Urheim S, Rabben SI, Skulstad H, Lyseggen E, Ihlen H, Smiseth OA. **Regional myocardial work by strain Doppler echocardiography and LV pressure: a new method for quantifying myocardial function**. Am J Physiol Heart Circ Physiol 2005;288:H2375-H2380.

57. Paterson I, Mielniczuk LM, O'Meara E, So A, White JA. **Imaging heart failure: current and future applications**. Can J Cardiol 2013;29:317-328.

58. Helle-Valle TM, Yu WC, Fernandes VR, Rosen BD, Lima JA. **Usefulness of radial strain mapping by multidetector computer tomography to quantify regional**

myocardial function in patients with healed myocardial infarction. Am J Cardiol 2010;106:483-491.

59. Friedrich MG. **Tissue characterization of acute myocardial infarction and myocarditis by cardiac magnetic resonance**. JACC Cardiovasc Imaging 2008;1:652-662.

60. Schneider JE, Wiesmann F, Lygate CA, Neubauer S. **How to perform an accurate assessment of cardiac function in mice using high-resolution magnetic resonance imaging**. J Cardiovasc Magn Reson 2006;8:693-701.

61. Delfino JG, Bhasin M, Cole R et al. **Comparison of myocardial velocities obtained with magnetic resonance phase velocity mapping and tissue Doppler imaging in normal subjects and patients with left ventricular dyssynchrony**. J Magn Reson Imaging 2006;24:304-311.

62. Uematsu M, Miyatake K, Tanaka N et al. **Myocardial velocity gradient as a new indicator of regional left ventricular contraction: detection by a two-dimensional tissue Doppler imaging technique**. J Am Coll Cardiol 1995;26:217-223.

63. De Boeck BW, Cramer MJ, Oh JK, van der Aa RP, Jaarsma W. **Spectral pulsed tissue Doppler imaging in diastole: a tool to increase our insight in and assessment of diastolic relaxation of the left ventricle**. Am Heart J 2003;146:411-419.

64. Bauer M, Cheng S, Jain M et al. **Echocardiographic speckle-tracking based strain imaging for rapid cardiovascular phenotyping in mice**. Circ Res 2011;108:908-916.

65. Amundsen BH, Helle-Valle T, Edvardsen T et al. **Noninvasive myocardial strain measurement by speckle tracking echocardiography: validation against sonomicrometry and tagged magnetic resonance imaging**. J Am Coll Cardiol 2006;47:789-793.

66. Korinek J, Wang J, Sengupta PP et al. **Two-dimensional strain--a Doppler-independent ultrasound method for quantitation of regional deformation: validation in vitro and in vivo**. J Am Soc Echocardiogr 2005;18:1247-1253.

67. Popovic ZB, Benejam C, Bian J et al. **Speckle-tracking echocardiography correctly identifies segmental left ventricular dysfunction induced by scarring in a rat model of myocardial infarction**. Am J Physiol Heart Circ Physiol 2007;292:H2809-H2816.

68. Dall'armellina E, Jung BA, Lygate CA, Neubauer S, Markl M, Schneider JE. **Improved method for quantification of regional cardiac function in mice using phase-contrast MRI**. Magn Reson Med 2012;67:541-551.

69. Zhou R, Pickup S, Glickson JD, Scott CH, Ferrari VA. **Assessment of global and regional myocardial function in the mouse using cine and tagged MRI**. Magn Reson Med 2003;49:760-764.

70. Schneider JE, Cassidy PJ, Lygate C et al. **Fast, high-resolution in vivo cine magnetic resonance imaging in normal and failing mouse hearts on a vertical 11.7 T system**. J Magn Reson Imaging 2003;18:691-701.

71. Schneider JE. **Assessment of global cardiac function**. Methods Mol Biol 2011;771:387-405.

72. Chalil S, Stegemann B, Muhyaldeen S et al. **Intraventricular dyssynchrony predicts mortality and morbidity after cardiac resynchronization therapy: a study using cardiovascular magnetic resonance tissue synchronization imaging**. J Am Coll Cardiol 2007;50:243-252.

73. Foley PW, Khadjooi K, Ward JA et al. **Radial dyssynchrony assessed by cardiovascular magnetic resonance in relation to left ventricular function, myocardial scarring and QRS duration in patients with heart failure**. J Cardiovasc Magn Reson 2009;11:50.

74. Hor KN, Wansapura JP, Al-Khalidi HR et al. **Presence of mechanical dyssynchrony in Duchenne muscular dystrophy**. J Cardiovasc Magn Reson 2011;13:12.

75. Gotte MJ, van Rossum AC, Twisk JWR, Kuijer JPA, Marcus JT, Visser CA. **Quantification of regional contractile function after infarction: strain analysis superior to wall thickening analysis in discriminating infarct from remote myocardium**. J Am Coll Cardiol 2001;37:808-817.

76. Zerhouni EA, Parish DM, Rogers WJ, Yang A, Shapiro EP. **Human heart: tagging with MR imaging--a method for noninvasive assessment of myocardial motion**. Radiology 1988;169:59-63.

77. Axel L, Dougherty L. **MR imaging of motion with spatial modulation of magnetization**. Radiology 1989;171:841-845.

78. Osman NF, McVeigh ER, Prince JL. **Imaging heart motion using harmonic phase MRI**. IEEE Trans Med Imaging 2000;19:186-202.

79. Zhong J, Liu W, Yu X. **Transmural myocardial strain in mouse: quantification of high-resolution MR tagging using harmonic phase (HARP) analysis**. Magn Reson Med 2009;61:1368-1373.

80. Aletras AH, Ding S, Balaban RS, Wen H. **DENSE: displacement encoding with stimulated echoes in cardiac functional MRI**. J Magn Reson 1999;137:247-252.

81. Gilson WD, Yang Z, French BA, Epstein FH. **Complementary displacement-encoded MRI for contrast-enhanced infarct detection and quantification of myocardial function in mice**. Magn Reson Med 2004;51:744-752.

82. Gilson WD, Yang Z, French BA, Epstein FH. **Measurement of myocardial mechanics in mice before and after infarction using multislice displacement-encoded MRI with 3D motion encoding**. Am J Physiol Heart Circ Physiol 2005;288:H1491-H1497.

83. Zhong X, Gibberman LB, Spottiswoode BS et al. **Comprehensive cardiovascular magnetic resonance of myocardial mechanics in mice using three-dimensional cine DENSE**. J Cardiovasc Magn Reson 2011;13:83.

84. Osman NF, Sampath S, Atalar E, Prince JL. **Imaging longitudinal cardiac strain on short-axis images using strain-encoded MRI**. Magn Reson Med 2001;46:324-334.

85. Sampath S, Osman NF, Prince JL. **A combined harmonic phase and strain-encoded pulse sequence for measuring three-dimensional strain**. Magn Reson Imaging 2009;27:55-61.

86. Kuijer JP, Hofman MB, Zwanenburg JJ, Marcus JT, van Rossum AC, Heethaar RM. **DENSE and HARP: two views on the same technique of phase-based strain imaging**. J Magn Reson Imaging 2006;24:1432-1438.

87. Pelc NJ, Sommer FG, Li KC, Brosnan TJ, Herfkens RJ, Enzmann DR. **Quantitative magnetic resonance flow imaging**. Magn Reson Q 1994;10:125-147.

88. Wedeen VJ. **Magnetic resonance imaging of myocardial kinematics. Technique to detect, localize, and quantify the strain rates of the active human myocardium**. Magn Reson Med 1992;27:52-67.

89. Constable RT, Rath KM, Sinusas AJ, Gore JC. **Development and evaluation of tracking algorithms for cardiac wall motion analysis using phase velocity MR imaging**. Magn Reson Med 1994;32:33-42.

90. Arai AE, Gaither CC, III, Epstein FH, Balaban RS, Wolff SD. **Myocardial velocity gradient imaging by phase contrast MRI with application to regional function in myocardial ischemia**. Magn Reson Med 1999;42:98-109.

91. Pelc NJ, Drangova M, Pelc LR et al. **Tracking of cyclic motion with phase-contrast cine MR velocity data**. J Magn Reson Imaging 1995;5:339-345.

92. Zhu Y, Drangova M, Pelc NJ. **Fourier tracking of myocardial motion using cine-PC data**. Magn Reson Med 1996;35:471-480.

93. Espe EK, Aronsen JM, Skrbic B et al. **Improved MR phase-contrast velocimetry using a novel nine-point balanced motion-encoding scheme with increased robustness to eddy current effects**. Magn Reson Med 2013;69:48-61.

94. Lingamneni A, Hardy PA, Powell KA, Pelc NJ, White RD. **Validation of cine phase-contrast MR imaging for motion analysis**. J Magn Reson Imaging 1995;5:331-338.

95. Drangova M, Zhu Y, Bowman B, Pelc NJ. **In vitro verification of myocardial motion tracking from phase-contrast velocity data**. Magn Reson Imaging 1998;16:863-870.

96. Zhu Y, Drangova M, Pelc NJ. **Estimation of deformation gradient and strain from cine-PC velocity data**. IEEE Trans Med Imaging 1997;16:840-851.

97. Delfino JG, Fornwalt BK, Eisner RL, Leon AR, Oshinski JN. **Determination of transmural, endocardial, and epicardial radial strain and strain rate from phase contrast MR velocity data**. J Magn Reson Imaging 2008;27:522-528.

98. Aletras AH, Wen H. **Mixed echo train acquisition displacement encoding with stimulated echoes: an optimized DENSE method for in vivo functional imaging of the human heart**. Magn Reson Med 2001;46:523-534.

99. Epstein FH, Gilson WD. **Displacement-encoded cardiac MRI using cosine and sine modulation to eliminate (CANSEL) artifact-generating echoes**. Magn Reson Med 2004;52:774-781.

100. Picano E, Lattanzi F, Orlandini A, Marini C, L'Abbate A. **Stress echocardiography and the human factor: the importance of being expert**. J Am Coll Cardiol 1991;17:666-669.

101. Jung B, Foll D, Bottler P, Petersen S, Hennig J, Markl M. **Detailed analysis of myocardial motion in volunteers and patients using high-temporal-resolution MR tissue phase mapping**. J Magn Reson Imaging 2006;24:1033-1039.

102. Jung B, Schneider B, Markl M, Saurbier B, Geibel A, Hennig J. **Measurement of left ventricular velocities: phase contrast MRI velocity mapping versus tissue-doppler-ultrasound in healthy volunteers**. J Cardiovasc Magn Reson 2004;6:777-783.

103. Nowosielski M, Schocke M, Mayr A et al. **Comparison of wall thickening and ejection fraction by cardiovascular magnetic resonance and echocardiography in acute myocardial infarction**. J Cardiovasc Magn Reson 2009;11:22.

104. Delfino JG, Johnson KR, Eisner RL, Eder S, Leon AR, Oshinski JN. **Three-directional myocardial phase-contrast tissue velocity MR imaging with navigator-echo gating: in vivo and in vitro study**. Radiology 2008;246:917-925.

105. Herold V, Morchel P, Faber C, Rommel E, Haase A, Jakob PM. **In vivo quantitative three-dimensional motion mapping of the murine myocardium with PC-MRI at 17.6 T**. Magn Reson Med 2006;55:1058-1064.

106. Steeden JA, Atkinson D, Taylor AM, Muthurangu V. **Assessing vascular response to exercise using a combination of real-time spiral phase contrast MR and noninvasive blood pressure measurements**. J Magn Reson Imaging 2010;31:997-1003.

107. Steeden JA, Atkinson D, Taylor AM, Muthurangu V. **Split-acquisition real-time CINE phase-contrast MR flow measurements**. Magn Reson Med 2010;64:1664-1670.

108. Schneider JE, Lanz T, Barnes H et al. **Accelerated cardiac magnetic resonance imaging in the mouse using an eight-channel array at 9.4 Tesla**. Magn Reson Med 2011;65:60-70.

109. Bauer S, Markl M, Foll D, Russe M, Stankovic Z, Jung B. **K-t GRAPPA accelerated phase contrast MRI: Improved assessment of blood flow and 3-directional myocardial motion during breath-hold**. J Magn Reson Imaging 2013;38:1054-1062.

110. Edvardsen T, Detrano R, Rosen BD et al. **Coronary artery atherosclerosis is related to reduced regional left ventricular function in individuals without history of clinical cardiovascular disease: the Multiethnic Study of Atherosclerosis**. Arterioscler Thromb Vasc Biol 2006;26:206-211.

111. Marcus JT, Gotte MJ, van Rossum AC et al. **Myocardial function in infarcted and remote regions early after infarction in man: assessment by magnetic resonance tagging and strain analysis**. Magn Reson Med 1997;38:803-810.

112. Foell D, Jung BA, Germann E et al. **Segmental myocardial velocities in dilated cardiomyopathy with and without left bundle branch block**. J Magn Reson Imaging 2013;37:119-126.

113. Nelson GS, Curry CW, Wyman BT et al. **Predictors of systolic augmentation from left ventricular preexcitation in patients with dilated cardiomyopathy and intraventricular conduction delay**. Circulation 2000;101:2703-2709.

114. Foell D, Jung B, Germann E, Staehle F, Bode C, Markl M. **Hypertensive heart disease: MR tissue phase mapping reveals altered left ventricular rotation and regional myocardial long-axis velocities**. Eur Radiol 2013;23:339-347.

115. Young AA, Kramer CM, Ferrari VA, Axel L, Reichek N. **Three-dimensional left ventricular deformation in hypertrophic cardiomyopathy**. Circulation 1994;90:854-867.

116. Edvardsen T, Rosen BD, Pan L et al. **Regional diastolic dysfunction in individuals with left ventricular hypertrophy measured by tagged magnetic resonance imaging--the Multi-Ethnic Study of Atherosclerosis (MESA)**. Am Heart J 2006;151:109-114.

117. Caudron J, Fares J, Bauer F, Dacher JN. **Evaluation of Left Ventricular Diastolic Function with Cardiac MR Imaging**. Radiographics 2011;31:239-259.

118. Nagel E, Lehmkuhl HB, Bocksch W et al. **Noninvasive diagnosis of ischemia-induced wall motion abnormalities with the use of high-dose dobutamine stress MRI: comparison with dobutamine stress echocardiography**. Circulation 1999;99:763-770.

119. Petersen SE, Jung BA, Wiesmann F et al. **Myocardial tissue phase mapping with cine phase-contrast mr imaging: regional wall motion analysis in healthy volunteers**. Radiology 2006;238:816-826.

120. Markl M, Schneider B, Hennig J. **Fast phase contrast cardiac magnetic resonance imaging: improved assessment and analysis of left ventricular wall motion**. J Magn Reson Imaging 2002;15:642-653.

121. Jung B, Markl M, Foll D, Hennig J. **Investigating myocardial motion by MRI using tissue phase mapping**. Eur J Cardiothorac Surg 2006;29 Suppl 1:S150-S157.

122. Reese TG, Feinberg DA, Dou J, Wedeen VJ. **Phase contrast MRI of myocardial 3D strain by encoding contiguous slices in a single shot**. Magn Reson Med 2002;47:665-676.

123. Cupps BP, Taggar AK, Reynolds LM, Lawton JS, Pasque MK. **Regional myocardial contractile function: multiparametric strain mapping**. Interact Cardiovasc Thorac Surg 2010;10:953-957.

124. Mangual JO, Foll D, Jung B, Pedrizzetti G, Kheradvar A. **Aging does not affect radial viscoelastic behavior of the left ventricle**. Cardiology 2013;125:38-49.

125. Haraldsson H, Wigstrom L, Lundberg M et al. **Improved estimation and visualization of two-dimensional myocardial strain rate using MR velocity mapping**. J Magn Reson Imaging 2008;28:604-611.

126. Schneider B, Markl M, Geiges C et al. **Cardiac phase contrast gradient echo MRI: characterization of abnormal left ventricular wall motion in patients with ischemic heart disease**. J Comput Assist Tomogr 2001;25:550-557.

127. Jung BA, Kreher BW, Markl M, Hennig J. **Visualization of tissue velocity data from cardiac wall motion measurements with myocardial fiber tracking: principles and implications for cardiac fiber structures**. Eur J Cardiothorac Surg 2006;29 Suppl 1:S158-S164.

128. Foll D, Jung B, Staehle F et al. **Visualization of multidirectional regional left ventricular dynamics by high-temporal-resolution tissue phase mapping**. J Magn Reson Imaging 2009;29:1043-1052.

129. Foll D, Jung B, Germann E, Hennig J, Bode C, Markl M. **Magnetic resonance tissue phase mapping: analysis of age-related and pathologically altered left ventricular radial and long-axis dyssynchrony**. J Magn Reson Imaging 2011;34:518-525.

130. Espe EK, Aronsen JM, Skardal K, Schneider JE, Zhang L, Sjaastad I. **Novel insight into the detailed myocardial motion and deformation of the rodent heart using high-resolution phase contrast cardiovascular magnetic resonance**. J Cardiovasc Magn Reson 2013;15:82.

131. Streif JU, Herold V, Szimtenings M et al. **In vivo time-resolved quantitative motion mapping of the murine myocardium with phase contrast MRI**. Magn Reson Med 2003;49:315-321.

132. Wiesmann F, Herold V, Streiff JU et al. **Novel insights into LV remodeling after murine myocardial infarction by in vivo magnetic resonance tissue velocity mapping**. Int J Cardiovasc Imaging 2004;20:289-291.

133. Dall'armellina E, Jung BA, Lygate CA, Neubauer S, Markl M, Schneider JE. **Improved method for quantification of regional cardiac function in mice using phase-contrast MRI**. Magn Reson Med 2012;67:541-551.

134. Wise RG, Al-Shafei AI, Carpenter TA, Hall LD, Huang CL. **Simultaneous measurement of blood and myocardial velocity in the rat heart by phase contrast MRI using sparse q-space sampling**. J Magn Reson Imaging 2005;22:614-627.

135. Vallee JP, Ivancevic MK, Nguyen D, Morel DR, Jaconi M. **Current status of cardiac MRI in small animals**. MAGMA 2004;17:149-156.

136. Shohet RV, Kisanuki YY, Zhao XS, Siddiquee Z, Franco F, Yanagisawa M. **Mice with cardiomyocyte-specific disruption of the endothelin-1 gene are resistant to hyperthyroid cardiac hypertrophy**. Proc Natl Acad Sci U S A 2004;101:2088-2093.

137. Franco F, Thomas GD, Giroir B et al. **Magnetic resonance imaging and invasive evaluation of development of heart failure in transgenic mice with myocardial expression of tumor necrosis factor-alpha**. Circulation 1999;99:448-454.

138. Siri FM, Jelicks LA, Leinwand LA, Gardin JM. **Gated magnetic resonance imaging of normal and hypertrophied murine hearts**. Am J Physiol 1997;272:H2394-H2402.

139. Slawson SE, Roman BB, Williams DS, Koretsky AP. **Cardiac MRI of the normal and hypertrophied mouse heart**. Magn Reson Med 1998;39:980-987.

140. Ruff J, Wiesmann F, Hiller KH et al. **Magnetic resonance microimaging for noninvasive quantification of myocardial function and mass in the mouse**. Magn Reson Med 1998;40:43-48.

141. Nahrendorf M, Wiesmann F, Hiller KH et al. **Serial cine-magnetic resonance imaging of left ventricular remodeling after myocardial infarction in rats**. J Magn Reson Imaging 2001;14:547-555.

142. Kohler S, Hiller KH, Waller C, Bauer WR, Haase A, Jakob PM. **Investigation of the microstructure of the isolated rat heart: a comparison between T*2- and diffusion-weighted MRI**. Magn Reson Med 2003;50:1144-1150.

143. Kohler S, Hiller KH, Griswold M, Bauer WR, Haase A, Jakob PM. **NMR-microscopy with TrueFISP at 11.75T**. J Magn Reson 2003;161:252-257.

144. Kohler S, Hiller KH, Waller C, Jakob PM, Bauer WR, Haase A. **Visualization of myocardial microstructure using high-resolution T*2 imaging at high magnetic field**. Magn Reson Med 2003;49:371-375.

145. Gilson WD, Epstein FH, Yang Z et al. **Borderzone contractile dysfunction is transiently attenuated and left ventricular structural remodeling is markedly reduced following reperfused myocardial infarction in inducible nitric oxide synthase knockout mice**. J Am Coll Cardiol 2007;50:1799-1807.

146. Vandsburger MH, French BA, Helm PA et al. **Multi-parameter in vivo cardiac magnetic resonance imaging demonstrates normal perfusion reserve despite severely attenuated beta-adrenergic functional response in neuronal nitric oxide synthase knockout mice**. Eur Heart J 2007;28:2792-2798.

147. Epstein FH, Yang Z, Gilson WD, Berr SS, Kramer CM, French BA. **MR tagging early after myocardial infarction in mice demonstrates contractile dysfunction in adjacent and remote regions**. Magn Reson Med 2002;48:399-403.

148. Young AA, French BA, Yang Z et al. **Reperfused myocardial infarction in mice: 3D mapping of late gadolinium enhancement and strain**. J Cardiovasc Magn Reson 2006;8:685-692.

149. Chuang JS, Zemljic-Harpf A, Ross RS, Frank LR, McCulloch AD, Omens JH. **Determination of three-dimensional ventricular strain distributions in gene-targeted mice using tagged MRI**. Magn Reson Med 2010;64:1281-1288.

150. Vandsburger MH, French BA, Kramer CM, Zhong X, Epstein FH. **Displacement-encoded and manganese-enhanced cardiac MRI reveal that nNOS, not eNOS, plays a dominant role in modulating contraction and calcium influx in the mammalian heart**. Am J Physiol Heart Circ Physiol 2012;302:H412-H419.

151. Nahrendorf M, Streif JU, Hiller KH et al. **Multimodal functional cardiac MRI in creatine kinase-deficient mice reveals subtle abnormalities in myocardial perfusion and mechanics**. Am J Physiol Heart Circ Physiol 2006;290:H2516-H2521.

152. Kilner PJ, Gatehouse PD, Firmin DN. **Flow measurement by magnetic resonance: a unique asset worth optimising**. J Cardiovasc Magn Reson 2007;9:723-728.

153. Gilman G, Khandheria BK, Hagen ME, Abraham TP, Seward JB, Belohlavek M. **Strain rate and strain: a step-by-step approach to image and data acquisition**. J Am Soc Echocardiogr 2004;17:1011-1020.

154. Hanson LG. **Is quantum mechanics necessary for understanding magnetic resonance?** Concepts Magn Reson 2008;32A:329-340.

155. Rabi II, Zacharias JR, Millman S, Kusch P. **A New Method of Measuring Nuclear Magnetic Moment**. Phys Rev 1938;53:318.

156. Bernstein MA, King KF, Zhou XJ. **Handbook of MRI Pulse Sequences**. Elsevier Academic Press; 2004.

157. Bryant DJ, Payne JA, Firmin DN, Longmore DB. **Measurement of flow with NMR imaging using a gradient pulse and phase difference technique**. J Comput Assist Tomogr 1984;8:588-593.

158. van DP. **Direct cardiac NMR imaging of heart wall and blood flow velocity**. J Comput Assist Tomogr 1984;8:429-436.

159. Gatehouse PD, Keegan J, Crowe LA et al. **Applications of phase-contrast flow and velocity imaging in cardiovascular MRI**. Eur Radiol 2005;15:2172-2184.

160. Morbiducci U, Ponzini R, Rizzo G et al. **Mechanistic insight into the physiological relevance of helical blood flow in the human aorta: an in vivo study**. Biomech Model Mechanobiol 2010.

161. Stalder AF, Frydrychowicz A, Russe MF et al. **Assessment of flow instabilities in the healthy aorta using flow-sensitive MRI**. J Magn Reson Imaging 2011;33:839-846.

162. Chernobelsky A, Shubayev O, Comeau CR, Wolff SD. **Baseline correction of phase contrast images improves quantification of blood flow in the great vessels**. J Cardiovasc Magn Reson 2007;9:681-685.

163. Hedstrom E, Bloch KM, Bergvall E, Stahlberg F, Arheden H. **Effects of gadolinium contrast agent on aortic blood flow and myocardial strain measurements by phase-contrast cardiovascular magnetic resonance**. J Cardiovasc Magn Reson 2010;12:70.

164. Vandsburger MH, Epstein FH. **Emerging MRI methods in translational cardiovascular research**. J Cardiovasc Transl Res 2011;4:477-492.

165. Gatehouse PD, Rolf MP, Graves MJ et al. **Flow measurement by cardiovascular magnetic resonance: a multi-centre multi-vendor study of background phase offset errors that can compromise the accuracy of derived regurgitant or shunt flow measurements**. J Cardiovasc Magn Reson 2010;12:5.

166. Pelc NJ. **Flow quantification and analysis methods**. Magn Reson Imaging Clin N Am 1995;3:413-424.

167. Sigfridsson A, Petersson S, Carlhall CJ, Ebbers T. **Four-dimensional flow MRI using spiral acquisition**. Magn Reson Med 2012;68:1065-1073.

168. Amirbekian S, Long RC, Jr., Consolini MA et al. **In vivo assessment of blood flow patterns in abdominal aorta of mice with MRI: implications for AAA localization**. Am J Physiol Heart Circ Physiol 2009;297:H1290-H1295.

169. Parzy E, Miraux S, Franconi JM, Thiaudiere E. **In vivo quantification of blood velocity in mouse carotid and pulmonary arteries by ECG-triggered 3D time-resolved magnetic resonance angiography**. NMR Biomed 2009;22:532-537.

170. Morbiducci U, Ponzini R, Rizzo G et al. **In vivo quantification of helical blood flow in human aorta by time-resolved three-dimensional cine phase contrast magnetic resonance imaging**. Ann Biomed Eng 2009;37:516-531.

171. Karwatowski SP, Brecker SJ, Yang GZ, Firmin DN, Sutton MS, Underwood SR. **Mitral valve flow measured with cine MR velocity mapping in patients with ischemic heart disease: comparison with Doppler echocardiography**. J Magn Reson Imaging 1995;5:89-92.

172. Gu T, Korosec FR, Block WF et al. **PC VIPR: a high-speed 3D phase-contrast method for flow quantification and high-resolution angiography**. AJNR Am J Neuroradiol 2005;26:743-749.

173. Stalder AF, Russe MF, Frydrychowicz A, Bock J, Hennig J, Markl M. **Quantitative 2D and 3D phase contrast MRI: optimized analysis of blood flow and vessel wall parameters**. Magn Reson Med 2008;60:1218-1231.

174. Codreanu I, Robson MD, Golding SJ, Jung BA, Clarke K, Holloway CJ. **Longitudinally and circumferentially directed movements of the left ventricle studied by cardiovascular magnetic resonance phase contrast velocity mapping**. J Cardiovasc Magn Reson 2010;12:48.

175. Pelc NJ, Bernstein MA, Shimakawa A, Glover GH. **Encoding strategies for three-direction phase-contrast MR imaging of flow**. J Magn Reson Imaging 1991;1:405-413.

176. Walker PG, Cranney GB, Grimes RY et al. **Three-dimensional reconstruction of the flow in a human left heart by using magnetic resonance phase velocity encoding**. Ann Biomed Eng 1996;24:139-147.

177. Johnson KM, Markl M. **Improved SNR in phase contrast velocimetry with five-point balanced flow encoding**. Magn Reson Med 2010;63:349-355.

178. Greville TNE. **The Pseudoinverse of A Rectangular Or Singular Matrix and Its Application to the Solution of Systems of Linear Equations**. Siam Review 1959;1:38-43.

179. Walker PG, Cranney GB, Scheidegger MB, Waseleski G, Pohost GM, Yoganathan AP. **Semiautomated method for noise reduction and background phase error correction in MR phase velocity data**. J Magn Reson Imaging 1993;3:521-530.

180. Morich MA, Lampman DA, Dannels WR, Goldie FD. **Exact temporal eddy current compensation in magnetic resonance imaging systems**. IEEE Trans Med Imaging 1988;7:247-254.

181. Rolf MP, Hofman MB, Gatehouse PD et al. **Sequence optimization to reduce velocity offsets in cardiovascular magnetic resonance volume flow quantification--a multi-vendor study**. J Cardiovasc Magn Reson 2011;13:18.

182. Holland BJ, Printz BF, Lai WW. **Baseline correction of phase-contrast images in congenital cardiovascular magnetic resonance**. J Cardiovasc Magn Reson 2010;12:11.

183. Boesch C, Gruetter R, Martin E. **Temporal and spatial analysis of fields generated by eddy currents in superconducting magnets: optimization of corrections and quantitative characterization of magnet/gradient systems**. Magn Reson Med 1991;20:268-284.

184. Giese D, Haeberlin M, Barmet C, Pruessmann KP, Schaeffter T, Kozerke S. **Analysis and correction of background velocity offsets in phase-contrast flow measurements using magnetic field monitoring**. Magn Reson Med 2011.

185. Ramsey JB. **Tests for Specification Errors in Classical Linear Least-Squares Regression Analysis**. Journal of the Royal Statistical Society Series B-Statistical Methodology 1969;31:350-&.

186. Drangova M, Zhu Y, Pelc NJ. **Effect of artifacts due to flowing blood on the reproducibility of phase-contrast measurements of myocardial motion**. J Magn Reson Imaging 1997;7:664-668.

187. Ferreira PF, Gatehouse PD, Mohiaddin RH, Firmin DN. **Cardiovascular magnetic resonance artefacts**. J Cardiovasc Magn Reson 2013;15:41.

188. Nishimura DG, Jackson JI, Pauly JM. **On the Nature and Reduction of the Displacement Artifact in Flow Images**. Magnetic Resonance in Medicine 1991;22:481-492.

189. Haacke EM, Lenz GW. **Improving MR image quality in the presence of motion by using rephasing gradients**. AJR Am J Roentgenol 1987;148:1251-1258.

190. Korin HW, Farzaneh F, Wright RC, Riederer SJ. **Compensation for Effects of Linear Motion in Mr Imaging**. Magnetic Resonance in Medicine 1989;12:99-113.

191. McVeigh ER. **MRI of myocardial function: motion tracking techniques**. Magn Reson Imaging 1996;14:137-150.

192. Hennig J, Schneider B, Peschl S, Markl M, Krause T, Laubenberger J. **Analysis of myocardial motion based on velocity measurements with a black blood prepared segmented gradient-echo sequence: methodology and applications to normal volunteers and patients**. J Magn Reson Imaging 1998;8:868-877.

193. Castillo E, Lima JA, Bluemke DA. **Regional myocardial function: advances in MR imaging and analysis**. Radiographics 2003;23 Spec No:S127-S140.

194. Garot J, Bluemke DA, Osman NF et al. **Fast determination of regional myocardial strain fields from tagged cardiac images using harmonic phase MRI**. Circulation 2000;101:981-988.

195. Ennis DB, Epstein FH, Kellman P, Fananapazir L, McVeigh ER, Arai AE. **Assessment of regional systolic and diastolic dysfunction in familial hypertrophic cardiomyopathy using MR tagging**. Magn Reson Med 2003;50:638-642.

196. Aletras AH, Ingkanisorn WP, Mancini C, Arai AE. **DENSE with SENSE**. J Magn Reson 2005;176:99-106.

197. Spottiswoode BS, Zhong X, Hess AT et al. **Tracking myocardial motion from cine DENSE images using spatiotemporal phase unwrapping and temporal fitting**. IEEE Trans Med Imaging 2007;26:15-30.

198. Cassidy PJ, Schneider JE, Grieve SM, Lygate C, Neubauer S, Clarke K. **Assessment of motion gating strategies for mouse magnetic resonance at high magnetic fields**. J Magn Reson Imaging 2004;19:229-237.

199. Janssen BJ, De CT, Debets JJ, Brouns AE, Callahan MF, Smith TL. **Effects of anesthetics on systemic hemodynamics in mice**. Am J Physiol Heart Circ Physiol 2004;287:H1618-H1624.

200. Zuurbier CJ, Emons VM, Ince C. **Hemodynamics of anesthetized ventilated mouse models: aspects of anesthetics, fluid support, and strain**. Am J Physiol Heart Circ Physiol 2002;282:H2099-H2105.

201. Kober F, Iltis I, Cozzone PJ, Bernard M. **Cine-MRI assessment of cardiac function in mice anesthetized with ketamine/xylazine and isoflurane**. MAGMA 2004;17:157-161.

202. Kober F, Iltis I, Cozzone PJ, Bernard M. **Myocardial blood flow mapping in mice using high-resolution spin labeling magnetic resonance imaging: influence of ketamine/xylazine and isoflurane anesthesia**. Magn Reson Med 2005;53:601-606.

203. Henkelman RM. **Measurement of signal intensities in the presence of noise in MR images**. Med Phys 1985;12:232-233.

204. Suga H. **Total mechanical energy of a ventricle model and cardiac oxygen consumption**. Am J Physiol 1979;236:H498-H505.

205. Takaoka H, Takeuchi M, Odake M, Yokoyama M. **Assessment of myocardial oxygen consumption (Vo2) and systolic pressure-volume area (PVA) in human hearts**. Eur Heart J 1992;13 Suppl E:85-90.

206. Hisano R, Cooper G. **Correlation of force-length area with oxygen consumption in ferret papillary muscle**. Circ Res 1987;61:318-328.

207. Simpson R, Keegan J, Firmin D. **Efficient and reproducible high resolution spiral myocardial phase velocity mapping of the entire cardiac cycle**. J Cardiovasc Magn Reson 2013;15:34.

208. Bernstein MA, Shimakawa A, Pelc NJ. **Minimizing TE in moment-nulled or flow-encoded two- and three-dimensional gradient-echo imaging**. J Magn Reson Imaging 1992;2:583-588.

209. Hamilton CA, Jordan JH, Kraft RA, Hundley WG. **Noninterleaved velocity encodings for improved temporal and spatial resolution in phase-contrast magnetic resonance imaging**. J Comput Assist Tomogr 2010;34:570-574.

210. Paschal CB, Morris HD. **K-space in the clinic**. J Magn Reson Imaging 2004;19:145-159.

211. Bernstein MA, Grgic M, Brosnan TJ, Pelc NJ. **Reconstructions of phase contrast, phased array multicoil data**. Magn Reson Med 1994;32:330-334.

212. Berr SS, Roy RJ, French BA et al. **Black blood gradient echo cine magnetic resonance imaging of the mouse heart**. Magn Reson Med 2005;53:1074-1079.

213. Liu W, Chen J, Ji S et al. **Harmonic phase MR tagging for direct quantification of Lagrangian strain in rat hearts after myocardial infarction**. Magn Reson Med 2004;52:1282-1290.

214. Bergvall E, Hedstrom E, Bloch KM, Arheden H, Sparr G. **Spline-based cardiac motion tracking using velocity-encoded magnetic resonance imaging**. IEEE Trans Med Imaging 2008;27:1045-1053.

215. Masood S, Gao J, Yang GZ. **Virtual tagging: numerical considerations and phantom validation**. IEEE Trans Med Imaging 2002;21:1123-1131.

216. Biswas M, Sudhakar S, Nanda NC et al. **Two- and three-dimensional speckle tracking echocardiography: clinical applications and future directions**. Echocardiography 2013;30:88-105.

217. Li Y, Garson CD, Xu Y et al. **Quantification and MRI validation of regional contractile dysfunction in mice post myocardial infarction using high resolution ultrasound**. Ultrasound Med Biol 2007;33:894-904.

218. Azam S, Desjardins CL, Schluchter M et al. **Comparison of velocity vector imaging echocardiography with magnetic resonance imaging in mouse models of cardiomyopathy**. Circ Cardiovasc Imaging 2012;5:776-781.

219. Daire JL, Jacob JP, Hyacinthe JN et al. **Cine and tagged cardiovascular magnetic resonance imaging in normal rat at 1.5 T: a rest and stress study**. J Cardiovasc Magn Reson 2008;10:48.

220. Hyacinthe JN, Ivancevic MK, Daire JL, Vallee JP. **Feasibility of complementary spatial modulation of magnetization tagging in the rat heart after manganese injection**. NMR Biomed 2008;21:15-21.

221. Kuijer JP, Marcus JT, Gotte MJ, van Rossum AC, Heethaar RM. **Three-dimensional myocardial strains at end-systole and during diastole in the left ventricle of normal humans**. J Cardiovasc Magn Reson 2002;4:341-351.

222. Zhong X, Helm PA, Epstein FH. **Balanced multipoint displacement encoding for DENSE MRI**. Magn Reson Med 2009;61:981-988.

223. Petitjean C, Rougon N, Cluzel P. **Assessment of myocardial function: a review of quantification methods and results using tagged MRI**. J Cardiovasc Magn Reson 2005;7:501-516.

224. Azhari H, Weiss JL, Shapiro EP. **In vivo assessment of regional myocardial work in normal canine hearts using 3D tagged MRI**. Adv Exp Med Biol 1997;430:241-248.

225. Zhu Y, Pelc NJ. **Three-dimensional motion tracking with volumetric phase contrast MR velocity imaging**. J Magn Reson Imaging 1999;9:111-118.

226. Johnson KM, Lum DP, Turski PA, Block WF, Mistretta CA, Wieben O. **Improved 3D phase contrast MRI with off-resonance corrected dual echo VIPR**. Magn Reson Med 2008;60:1329-1336.

227. Wigstrom L, Sjoqvist L, Wranne B. **Temporally resolved 3D phase-contrast imaging**. Magn Reson Med 1996;36:800-803.

I

II

III

Journal of Cardiovascular Magnetic Resonance

RESEARCH Open Access

Novel insight into the detailed myocardial motion and deformation of the rodent heart using high-resolution phase contrast cardiovascular magnetic resonance

Emil KS Espe[1,2*], Jan Magnus Aronsen[1,2,3], Kristine Skårdal[1,2], Jürgen E Schneider[4], Lili Zhang[1,2] and Ivar Sjaastad[1,2]

Abstract

Background: Phase contrast velocimetry cardiovascular magnetic resonance (PC-CMR) is a powerful and versatile tool allowing assessment of *in vivo* motion of the myocardium. However, PC-CMR is sensitive to motion related artifacts causing errors that are geometrically systematic, rendering regional analysis of myocardial function challenging. The objective of this study was to establish an optimized PC-CMR method able to provide novel insight in the complex regional motion and strain of the rodent myocardium, and provide a proof-of-concept in normal and diseased rat hearts with higher temporal and spatial resolution than previously reported.

Methods: A PC-CMR protocol optimized for assessing the motion and deformation of the myocardium in rats with high spatiotemporal resolution was established, and ten animals with different degree of cardiac dysfunction underwent examination and served as proof-of-concept. Global and regional myocardial velocities and circumferential strain were calculated, and the results were compared to five control animals. Furthermore, the global strain measurements were validated against speckle-tracking echocardiography, and inter- and intrastudy variability of the protocol were evaluated.

Results: The presented method allows assessment of regional myocardial function in rats with high level of detail; temporal resolution was 3.2 ms, and analysis was done using 32 circumferential segments. In the dysfunctional hearts, global and regional function were distinctly altered, including reduced global peak values, increased regional heterogeneity and increased index of dyssynchrony. Strain derived from the PC-CMR data was in excellent agreement with echocardiography ($r = 0.95$, $p < 0.001$; limits-of-agreement -0.02 ± 3.92%strain), and intra- and interstudy variability were low for both velocity and strain (limits-of-agreement, radial motion: 0.01 ± 0.32 cm/s and -0.06 ± 0.75 cm/s; circumferential strain: -0.16 ± 0.89%strain and -0.71 ± 1.67%strain, for intra- and interstudy, respectively).

Conclusion: We demonstrate, for the first time, that PC-CMR enables high-resolution evaluation of *in vivo* circumferential strain in addition to myocardial motion of the rat heart. In combination with the superior geometric robustness of CMR, this ultimately provides a tool for longitudinal studies of regional function in rodents with high level of detail.

Keywords: CMR, 3D phase contrast, Strain analysis, Tissue phase mapping, Myocardial motion, Myocardial strain, Motion artifacts

* Correspondence: ekespe@medisin.uio.no
[1]Institute for Experimental Medical Research, Oslo University Hospital and University of Oslo, Kirkeveien 166, N-0407 Oslo, Norway
[2]KG Jebsen Cardiac Research Center and Center for Heart Failure Research, University of Oslo, Oslo, Norway
Full list of author information is available at the end of the article

Background

The intricate motion and deformation of the heart can be assessed *in vivo* with varying degree of detail using several different techniques, including sonomicrometry, echocardiography employing Tissue Doppler Imaging or speckle-tracking strain analysis, as well as various cardiovascular magnetic resonance (CMR) techniques. Compared to other modalities, CMR offers measurements of true 3D function with practically no limitations in visualization geometry, and thus provides complete freedom in choosing regions for examination. Different techniques for the evaluation of myocardial function are available, including myocardial tagging [1], strain-encoded CMR (SENC) [2], displacement-encoded imaging with stimulated echoes (DENSE) [3] and phase contrast imaging (PC-CMR) [4]. The latter two offer pixel-wise measurement of displacement and velocity, respectively, allowing for high-resolution evaluation of tissue function. However, PC-CMR is the only CMR technique that been shown to allow assessment of velocity with high spatial and temporal resolution [5] and, subsequently, displacement [6], strain rate [7] and strain [8] concurrently, throughout the entire cardiac cycle. While PC-CMR velocimetry is emerging as a powerful and versatile tool for assessment of tissue motion both in humans and in rodents [5,9], it has only been reported so far for the assessment of average myocardial velocities within a slice, or in a few (<=8) circumferential segments. Also, it might be challenging to achieve the optimal temporal resolution to capture the fine details of cardiac motion in small animals. Thus, to accurately investigate the regional function e.g. in hearts with infarctions with various sizes, and in order to derive parameters such as subtle dyssynchrony, transmural functional gradients or longitudinal spread of dysfunction, data with higher spatial and temporal resolution along with appropriate post-processing procedures are essential.

In PC-CMR, the displacement of spins between the centers of the bipolar encoding gradient lobes is encoded into the phase of the MR signal, producing datasets with near-instantaneous velocities with temporal resolution equal to the TR [10,11]. Although PC-CMR is prone to errors from several sources, including concomitant gradient [12] and eddy-current induced [13] artifacts, several approaches has been proposed to minimize these errors [12,14,15]. However, PC-CMR encoded acquisitions are intrinsically non-motion compensated and thus particularly sensitive to flow- and motion related artifacts, such as ghosting due to beat-to-beat variation in blood flow [16,17]. In Cartesian imaging, motion-related artifacts manifest in the phase-encoding direction, and may (in a short-axis view) affect the measurements non-uniformly over the circumference of the myocardium. This could lead to systematic errors when regional myocardial function is to be assessed, reducing the effective level of detail available for analysis. Black-blood contrast is therefore essential in PC-CMR of the myocardium, reducing this effect [5]. In addition, the impact of directionally dependent artifacts in studies employing signal averaging can be reduced by an in-plane rotation of the field-of-view (FOV) between the acquisitions, referred to as rotating FOV (Figure 1).

In this study, we present a PC-CMR approach for assessing left ventricular (LV) myocardial motion in rats, employing a rotating FOV along with optimized acquisition parameters and post-processing protocols. We aim to demonstrate the feasibility of PC-CMR for accurately describing both myocardial motion and deformation in rodents by deriving global parameters such as peak velocities and maximum circumferential strain, as well as describing the spatial variability in essential parameters with higher resolution than have been previously reported. By applying this method on rats with myocardial infarction, we were able to describe distinct alterations in regional myocardial function, compared to sham-operated controls. These findings were validated against speckle-tracking echocardiography, confirming our protocol with PC-CMR as an accurate tool for investigating regional myocardial function in rats.

Methods

Experimental animals

Myocardial infarction was induced in male Wistar rats (10–12 weeks old, ~300 g) as described previously [18], where the left coronary artery was occluded by a silk suture. Six weeks later, cardiac imaging was performed. Inclusion criterion was visible myocardial infarction on echocardiography, and we selected both rats with small and large infarctions (infarct size range 21%-46%). Sham-operated rats went through the same procedure, except no coronary artery ligation was performed. Animals were 16–18 weeks old at the time of cardiac imaging.

The animal weights during examination were in the range 400–450 g. For evaluation of the PC-CMR method, the animals (total N = 15) were divided into two groups, one cohort to validate the method relative to echocardiography (post-MI (N = 6), sham (N = 3)), and one cohort to perform inter- and intrastudy variability analysis (post-MI (N = 4), sham (N = 2)). All animals were cared for according to the Norwegian Animal Welfare Act. The use of animals was approved by the Norwegian Animal Research Authority (ID 3284), and conformed to the *Guide for the Care and Use of Laboratory Animals* published by the US National Institutes of Health and the *European Convention for the Protection of Vertebrate Animals used for Experimental and Other Scientific Purposes* (ETS no. 123).

Anesthesia was induced in a chamber with a mixture of O_2 and 4.5% isoflurane, and maintained during experiments by administration of a mixture of O_2 and 1.5% isoflurane in freely breathing animals. During the CMR experiments,

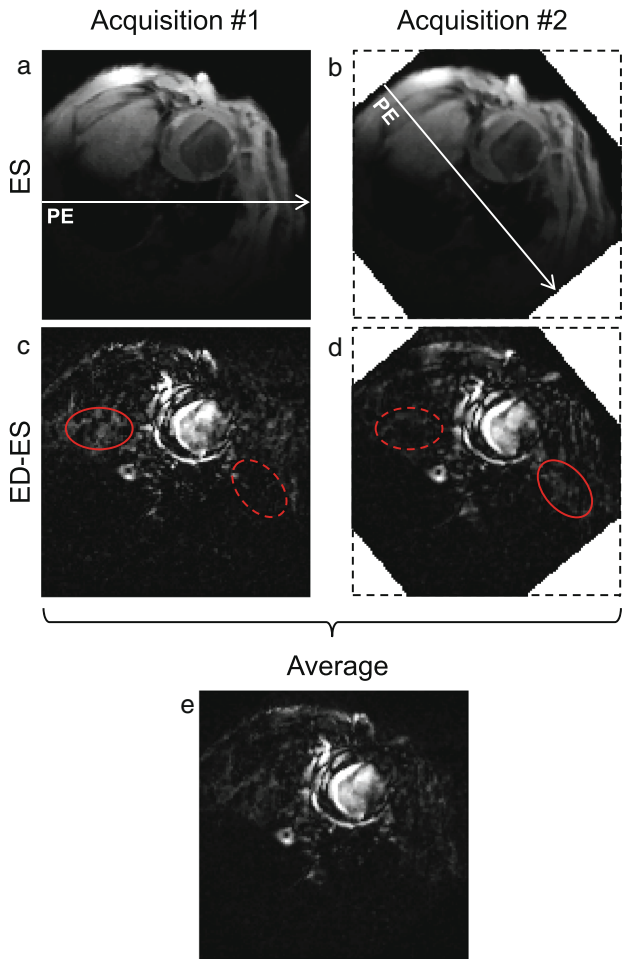

Figure 1 Geometrically systematic artifacts. Even after black-blood preparation, some flow artifacts remain. Although not obvious in the original end-systolic (ES) magnitude images **(a,b)**, the *difference* between the magnitude images of end-diastole (ED) and end-systole **(c,d)** reveal geometrically systematic artifacts. A rotation of the field-of-view alters the characteristics of these artifacts. Both acquisitions exhibit unique artifacts in the phase-encoding direction (solid ellipses), not present in the other (dashed ellipse). In the average image **(e)**, these artifacts are reduced. For illustrative purposes, a median filter has been applied for noise reduction in this figure. In **c**-**e** the grayscale has been exaggerated for clarity.

body temperature was maintained using heated air; and ECG, respiration rate and animal temperature were constantly monitored. Respiration was registered by an air cushion. The heart rate was kept as constant as practically possible during experiments by minor adjustments of the level of anesthesia.

Echocardiography

Echocardiography examinations were performed on a Vevo 2100 (Visual Sonics Inc., Ontario, Canada) scanner with a 24 MHz transducer approximately one day prior to CMR scan. For the animals included in the validation study, global circumferential strain was calculated off-line by 2D speckle-tracking [19] in mid-ventricular short-axis slices. The temporal resolution of the echocardiography data was 152 frames per second.

CMR hardware and acquisition

CMR experiments were performed on a 9.4 T/210 mm/ASR horizontal bore magnet (Agilent Technologies, Inc.,

USA) with a high-performance actively shielded gradient coil (inner diameter 120 mm, rise time 180 μs, max strength 600 mT/m). A quadrature volume transmit coil (inner diameter 72 mm) was used in combination with a four-channel surface receive coil array dedicated to rat heart imaging. Bipolar motion encoding gradients were incorporated into an RF-spoiled gradient echo cine sequence [9]. The acquisition employed a nine-point balanced scheme [15] encoding motion in three orthogonal directions, and was non-interleaved, that is, each encoding step was recorded separately with full temporal resolution [20]. Black-blood contrast was achieved by placing saturation slices above and below the imaging slice, applied at the end of the cine train [5]. To allow for some decay of eddy currents in the system, a short delay (τ = 250 μs) was introduced between the second encoding gradient lobe and the readout gradient.

In each animal, a mid-ventricular LV short-axis slice was planned as described by Schneider et al. [21]. Acquisition was prospectively triggered by ECG R-peak and gated for respiration by pausing acquisition during respiratory motion. 70-80 time frames were recorded covering >130% of the r-r-interval, with a temporal resolution of 3.2 ms. Overshooting the r-r-interval permitted complete coverage of the diastole in combination with black-blood saturation; and provided time for decay of gradient-induced disturbances in the ECG signal.

To reduce the impact of directional-dependent artifacts, each slice was acquired twice (corresponding to 2x signal averaging), where the second acquisition was rotated (in-plane) at least 30 degrees with respect to the first.

Key imaging parameters were as follows: TE/TR = 2.2/3.2 ms; FOV = 50x50 mm; matrix 128x128, slice thickness 1.5 mm, flip angle 7°, receiver bandwidth = 156.25 kHz; *venc* = 13.9 cm/s. Acquisition time for a complete slice was 10-15 minutes, depending on heart rate.

CMR post-processing

The phase contrast data was extracted from the multi-receiver array coil data as described by Bernstein et al. [22], including complex-conjugated multiplication of the encoded scans with the reference scans individually for each coil element. Spatially-specific ECC was performed as previously described [13], excluding areas in the FOV subject to fold-over artifacts from analysis [15].

The data sets were subsequently semi-automatically segmented and analyzed using a purpose-written Matlab software (The MathWorks, Natick, USA). The only human inputs required during post-processing were 1) tracking of subendo- and subepicardial border at key time frames (segmentation of intermediate time frames were automatically interpolated), 2) definition of position of papillary muscles in the images, 3) definition of regions in the image subject to fold-over artifacts and 4) definition of the last diastolic time-point. Bulk cardiac motion was corrected for by subtraction of the average in-plane motion. Data points outside the myocardial mask were discarded, and the accepted data points were automatically divided into 32 segments [15]. Both the myocardial mask and segments followed the motion of the LV throughout the cycle. Finally, the velocity vector in each pixel was decomposed into a cardiopolar coordinate system, constituting of in-plane radial and tangential components and a through-plane longitudinal component [5]. The time points corresponding to peak and end-systole was automatically determined from peak global radial motion and minimum LV lumen area, respectively.

The data from the two individual acquisitions were independently processed, including division into segments using the papillary muscles as reference points, and segment-wise averaged as the last step of post-processing. To reduce low-pass filtering of the velocities following signal averaging (due to potential slight variation in heart rate), the data was normalized prior to combination. This was done by temporal stretching the data (using cubic spline interpolation) from one acquisition to the point where maximum correlation in global radial velocity between the acquisitions was achieved.

Myocardial trajectories and strain calculations

Pixel-by-pixel motion paths were calculated from the velocity data through forward-backward-integration-based Fourier tracking [6,23], with nearest-neighbor interpolation estimating velocities at non-grid locations. Trajectories travelling out of the user-defined myocardial mask were automatically discarded, but no other signal filtering was employed. To include more data points into the analysis (since the in-slice myocardial area is larger in end-systole), the motion tracking was performed twice. This was done by extending the forward-backward motion tracking protocol to calculate motion paths with temporal origin of integration in both end-diastole and end-systole, resulting in two separate descriptions of the displacement field of the myocardium. In both datasets, circumferential strain was calculated in each of the 32 myocardial segments from the trajectories of the two adjacent segments, before the strain waveforms from the two individual trajectory tracings were averaged segment-wise.

The circumferential (Lagrangian) strain in segment s at time t was given by [24]

$$Sc_s(t) = \frac{|\boldsymbol{x}_{s-1}(t) - \boldsymbol{x}_{s+1}(t)|}{|\boldsymbol{x}_{s-1}(1) - \boldsymbol{x}_{s+1}(1)|} - 1 \qquad (1)$$

where $\boldsymbol{x}_s(t)$ is the mean in-plane position vector for all pixels in segment s at time t, and *s-1* and *s+1* refer to the two adjacent segments. As the motion paths were closed,

it follows from Eq. 1 that $Sc_s(1) = Sc_s(t_{ED}) = 0$, where t_{ED} is the time point corresponding to end-diastole.

Evaluation of global and regional cardiac function

To investigate global function, peak global radial velocities and circumferential strain (*Sc*) were calculated in each animal. Furthermore, in order to evaluate regional function, the following parameters were determined:

- *Dispersion of peak motion*; the in-slice standard deviation over the 32 segments of the regional radial velocities at peak systole.
- *Dispersion of peak strain*; the segment-wise standard deviation of the regional *Sc* at end-systole.
- *Coherence of motion waveforms*: the mean temporal correlation coefficient of regional vs. global radial velocity tracings (as described by Markl et al. [25]).
- *Dispersion of motion waveforms*: the standard deviation of the above, over the 32 segments.
- *Index of dyssynchrony*: evaluated from cross-correlation delay analysis where the temporal shift in the regional velocity waveforms that maximized the correlation relative to the global motion was calculated (as described by Delfino et al. [26]). The standard deviation of the 32 delays in each animal was used as a single index of myocardial dyssynchrony.

Validation of strain calculations

In order to validate the PC-CMR-derived circumferential strain, the global *Sc* was compared to echocardiography-derived global *Sc*. The number of temporal sampling points for a complete cardiac cycle varied between the data sets, due to differences between the techniques and animal heart rate. The dataset with lowest number of sampling points had 23 data points covering the cardiac cycle. To allow temporal paired analysis between the methods, all datasets were re-sampled using cubic spline interpolation to 23 equally spaced time points, and synchronized to peak global *Sc*.

In addition, as an internal control, the PC-CMR-derived *Sc* was compared with *Sc* estimated directly from the segmentation polygons following the borders of the subepi- and subendocardium. Here, the mean global *Sc* was estimated from

$$Sc_g(t) = \frac{1}{2}\left(\frac{L_{\mathrm{epi}}(t) - L_{\mathrm{epi}}(1)}{L_{\mathrm{epi}}(1)} + \frac{L_{\mathrm{endo}}(t) - L_{\mathrm{endo}}(1)}{L_{\mathrm{endo}}(1)}\right) \quad (2)$$

where $L_{\mathrm{epi}}(t)$ and $L_{\mathrm{endo}}(t)$ are the lengths, at time t, of the polygons delineating the subepi- and subendocardium, respectively.

Inter- and intrastudy variability

To evaluate inter- and intrastudy variability of the protocol, six animals underwent two PC-CMR examinations on separate days, one of which included two full acquisitions of the same mid-ventricular short-axis slice. Inter- and intrastudy variability in global myocardial velocities and *Sc* were analyzed using limits-of-agreement. To avoid temporal jitter, all data sets were normalized to end-systole [27].

Statistical analysis

Student's t-test was used for statistical analysis when comparing the dysfunctional heart to the controls, and p-values < =0.05 were considered statistically significant. Statistical analysis was performed using Matlab. Measurements are presented as mean with standard deviation in parentheses, and correlation coefficients are Pearson's *r*.

Results

Animal characteristics

Animal characteristics for the rats included in the validation study are listed in Table 1. During echocardiography, the mean heart rate for the 9 animals in the validation study was 354 (35) bpm. Mean heart rate in all 15 animals during CMR experiments was 371 (31) bmp. Heart rate was not significantly different between groups. On average, the standard deviation of the heart rate in individual animals throughout the CMR examination was 10 bpm.

Analysis of myocardial motion

Examples of radial velocities in a representative post-MI heart are shown in Figure 2, and compared to a representative control heart. Distinct alterations in both global (Figure 2a) and regional (Figure 2b-c) motion are evident in the images. The latter also demonstrate the spatiotemporal resolution of the data. Likewise, global and regional Sc are depicted in Figure 3, comparing the same post-MI and control hearts. In Figure 3c and e, the dispersions of regional *Sc* at peak global *Sc* are illustrated, that is, the profile of the line marked in Figure 3b and d. In both hearts heterogeneity in regional *Sc* is evident; however major alterations in the post-MI hearts are clearly visible.

Central parameters on myocardial function are listed in Table 2. Peak systolic radial velocity was reduced in the post-MI animals compared to the control ($p < 0.001$), as was global *Sc* ($p < 0.001$). Intragroup variation in peak

Table 1 Body and organ weights for the animals included in the validation study

	Sham (N = 3)	Post-MI (N = 6)	t-test p-value
Body weight (g)	431 (25)	406 (37)	NS
Heart weight (g)	1.19 (0.19)	2.20 (0.45)	0.008
Lung weight (g)	1.36 (0.13)	3.83 (1.24)	0.013

NS = not significant. Values are mean (SD).

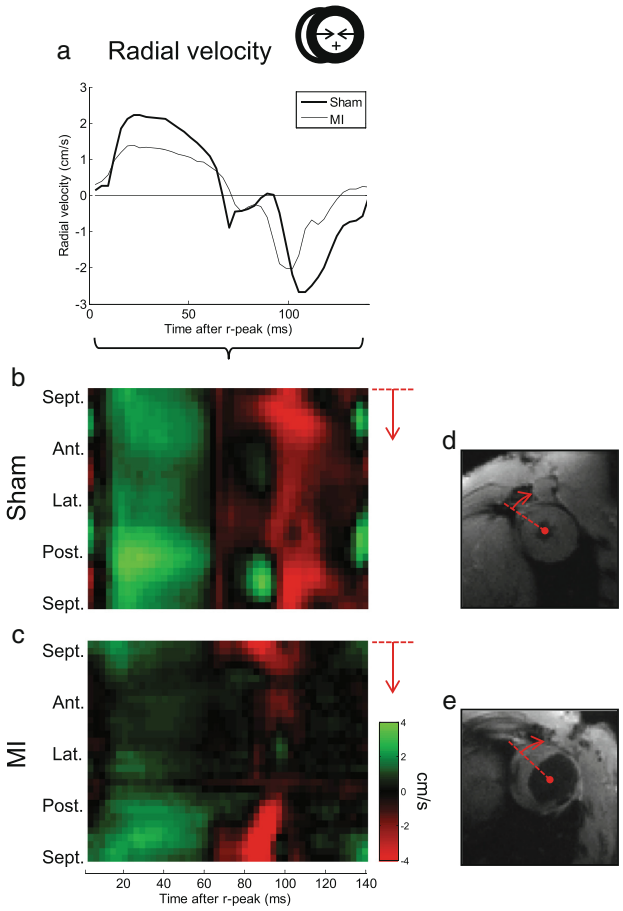

Figure 2 Example of radial motion waveforms. The global radial **(a)** in-slice velocities for two representative animals are shown, one post-MI and one sham. Note the distinct reduction in peak velocities in the diseased heart. Also, spatiotemporally resolved motion maps are displayed as colored plots **(b**-**c)** where the y-axis is circumferential position (i.e. segment; direction anteroseptal-anterior-lateral-posterior-posterioseptal), and x-axis is time after r-peak. Green color is positive radial motion (i.e. contraction), red is negative. The altered motion, especially in the anterolateral wall where the infarction is located, is clearly visible. Corresponding CMR magnitude images are shown **(d**,**e)**, illustrating the location of myocardial thinning in the infarcted heart. The line denotes the first segment and counting direction.

diastolic radial velocity was larger in the post-MI animals compared to controls, but the mean value was not significantly different between the groups. The dispersion (i.e., the standard deviation over the segments) of regional velocities and *Sc* in peak systole and end-systole, respectively, was increased in the post-MI animals ($p = 0.02$ and < 0.001). The regional radial velocity waveforms in the post-MI hearts exhibited lower correlation to the respective global velocities than in the control hearts, and the standard deviation (the spread) of the correlation coefficients was likewise increased in the post-MI hearts (both $p < 0.001$). The post-MI hearts also exhibited increased index of dyssynchrony, identified from the spread of cross-correlation delays over the circumference ($p = 0.006$).

Validation of strain calculations

Analysis of temporally resolved global *Sc* demonstrated excellent correlation between PC-CMR and echocardiography data ($r = 0.95$, $p < 0.001$; $N = 207$). A linear fit revealed a close relationship between temporally resolved CMR- and echocardiography-derived data, with a slope not significantly different from 1.00 (95% confidence bounds:

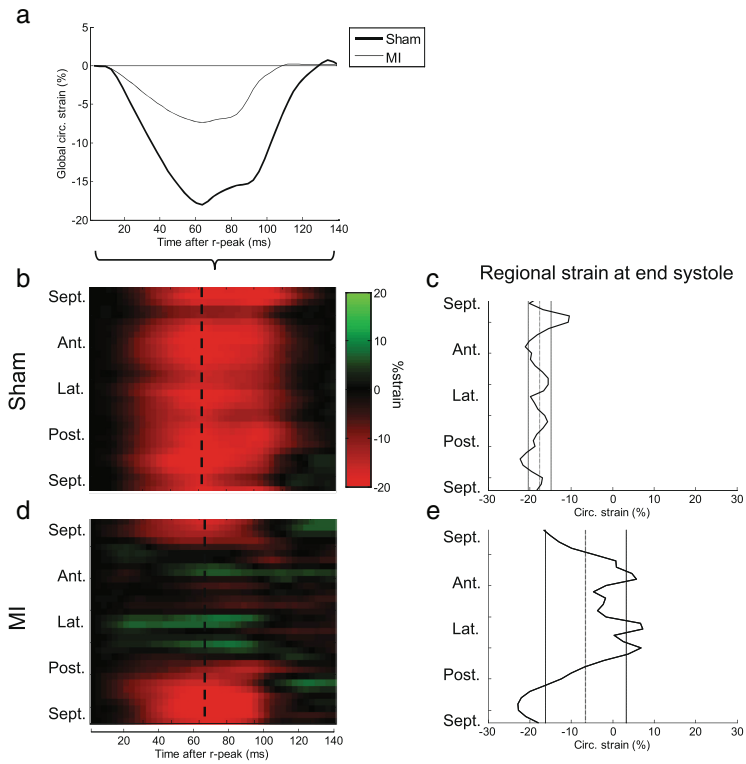

Figure 3 Global and regional circumferential strain. For the same animals shown in Figure 2, the global circumferential strain (*Sc*) is shown here as a function of time **(a)**. Furthermore, regional variation in temporally-resolved *Sc* is illustrated as color plots **(b**,**d)** where y-axis is circumferential position and x-axis is time after r-peak. Finally, the dispersion of *Sc* at end-systole (peak global *Sc*) is shown as a function of circumferential position **(c**,**e)**. Mean and standard deviation of the global *Sc* at that time point is shown as vertical lines.

[0.97, 1.07], $R^2 = 0.90$), see Figure 4a. Bland-Altman limits-of-agreement was −0.02 ± 3.92%strain (Figure 4b). Intra-animal analysis exhibited likewise strong correlation in all animals (mean r = 0.94 (0.08), p < 0.001 and N = 23 in all nine animals).

The PC-CMR-derived *Sc* also correlated well with *Sc* estimated directly from the segmentation polygons (r = 0.95, p < 0.001; N = 207), with limits-of-agreement −1.4 ± 4.8%. However, linear fit revealed a relationship whose slope significantly different from 1.00 (95% confidence bounds:

Table 2 Selected parameters from PC-CMR acquisition

		Sham (N = 5)	MI (N = 10)	t-test p value
Peak global radial velocity (cm/s)	Max.	2.22 (0.14)	1.41 (0.37)	<0.001
	Min.	−2.68 (0.38)	−2.64 (1.03)	NS
Peak global *Sc* (% strain)		−19.87 (2.28)	−6.98 (2.34)	<0.001
Dispersion of peak motion (cm/s)		0.58 (0.17)	0.91 (0.24)	0.02
Dispersion of peak strain (% strain)		5.91 (2.12)	10.40 (1.26)	<0.001
Coherence of motion waveforms		0.95 (0.02)	0.74 (0.09)	<0.001
Dispersion of motion waveforms		0.03 (0.01)	0.24 (0.10)	<0.001
Index of dyssynchrony (ms)		1.44 (0.37)	12.60 (7.37)	0.006

Sc = Circumferential strain. NS = not significant. Values are mean (SD).

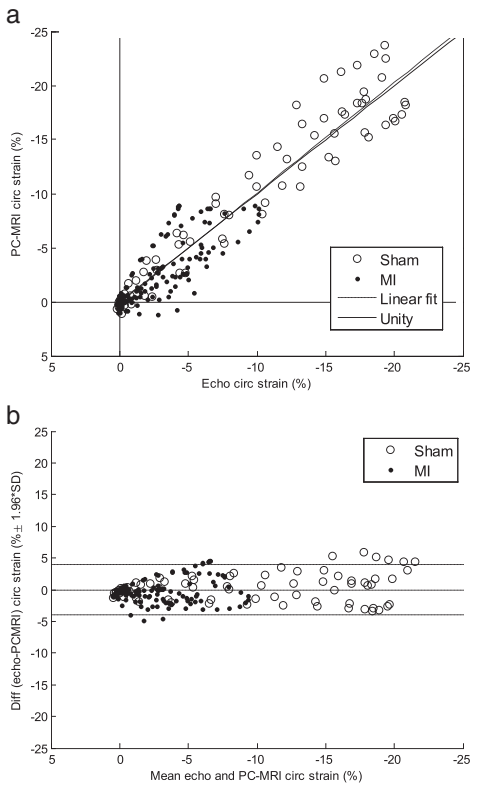

Figure 4 Comparison of circumferential strain measurements from CMR and echocardiography. Scatterplot **(a)** and Bland-Altman plot **(b)** of the data from the validation of PC-CMR-derived global *Sc* against 2D speckle-tracking echocardiography. Each animal (N = 9) had 23 equally spaced time points covering the complete cardiac cycle, producing a total of N = 207 data points. The data demonstrate small limits-of-agreement with no significant bias.

[0.76,0.82]). Intra-animal analysis also demonstrated good correlation (mean r = 0.95 (0.05), $p < 0.001$ and N = 23 in all nine animals).

Intra- and interstudy variability

The resulting intra- and interstudy limits-of-agreement are listed in Table 3. Intra- and interstudy variability in the actual velocity and *Sc* waveforms from a single animal are illustrated in Figure 5.

Discussion

In this study, we have presented a PC-CMR protocol for assessing myocardial motion in rats. Several steps were introduced in data acquisition and post-processing to optimize the protocol. PC-CMR-derived circumferential strain was validated against echocardiography, and we demonstrated that PC-CMR is capable of capturing fine details in the intricate motion of the rodent heart. The velocity and strain data exhibited distinct alterations, both globally and regionally, in the post-MI hearts vs. sham.

Our findings on global *Sc* agree well with an MR tagging study by Liu and colleagues [28], which reported mid-ventricular *Sc* in the normal rat heart as −19 (1)%. A study by the same group based on harmonic phase MR tagging [29] investigated the reduction in strain in infarcted hearts. Both studies had 15 temporal frames per cardiac cycle. In a study employing displacement-encoded CMR of infarcted mouse hearts, the circumferential strain one day post-surgery was found to be reduced from −16.4 (1.3)% in controls to −11.6 (1.8) and +4.2 (2.4)% in non-infarcted and infarcted regions, respectively [30]. They also demonstrated good correlation with MR tagging.

Distinct regional alterations in infarcted rat hearts have previously been demonstrated using speckle-tracking echocardiography [31], and our results agree well with their reported circumferential strain. That study also reported, in accordance with our findings, prominent heterogeneity in the *Sc* in healthy rat hearts. Our results are also in excellent agreement with other studies on global myocardial *Sc* in rat hearts [32,33].

A recent study by Dall'Armellina et al. [5] employed PC-CMR in studying myocardial velocities in mice, reporting corresponding findings on myocardial motion. The waveform of the global mid-ventricular radial motion is very similar between the species; however we found peak radial velocities (both in systole and diastole) in normal rats to be roughly the double of what they found in mice. Also, the regional heterogeneity of the motion around the circumference seems more pronounced in normal rats compared to mice. While this might reflect an actual variance between the species, differences could also be attributed to a fewer number of circumferential segments employed in [5].

Validation

PC-CMR has been previously validated as a technique capable of accurately measuring velocity [4,15], displacement [16,34] and the deformation gradient of the myocardium [8]. It has been used for calculation of myocardial strain [4,7] and has been compared to MR tagging (by use of "virtual tagging") [35]. In our study, two-dimensional speckle-tracking echocardiography (2D-STE) serves as a method for comparison. 2D-STE has been validated against tagged CMR, sonomicrometry and tissue Doppler echocardiography [36], and previously compared to DENSE CMR in mice [37,38]. Our findings demonstrate that global *Sc* in a mid-ventricular slice derived from PC-CMR

Table 3 Intra- and interstudy limits-of-agreement

	Intrastudy variability		Interstudy variability	
Radial velocity	0.01 ± 0.32 cm/s	0.07 ± 2.30%venc	−0.06 ± 0.75 cm/s	−0.43 ± 5.40%venc
Circ. velocity	0.10 ± 0.35 cm/s	0.72 ± 2.52%venc	0.06 ± 0.94 cm/s	0.43 ± 6.76%venc
Long. velocity	0.13 ± 0.51 cm/s	0.94 ± 3.67%venc	0.12 ± 1.15 cm/s	0.86 ± 8.27%venc
Sc	−0.16 ± 0.89%		−0.71 ± 1.67%	
Sc (single motion tracking)*	−0.15 ± 0.96%		−0.78 ± 2.31%	

Velocity variability shown in absolute values (cm/s) and percentage of the applied *venc*. Strain variability is reported in absolute values (%strain). *Sc* = Circumferential strain. N = 43x6 = 258. Values are mean ± 1.96*SD.
*: *Sc* was also calculated from motion paths using only end-diastole as temporal origin, as described in [23], without our proposed extension of also including end-systole as temporal origin.

correlates well with echocardiography-derived *Sc*, with narrow limits-of-agreement.

When comparing to mask-derived *Sc*, both PC-CMR and echo yielded a linear slope significantly different from 1.00, both results suggesting that the mask-derived *Sc* systematically overestimated the strain (this is also supported by the fact that the 95% confidence bounds for the linear slope of mask vs. PC-CMR and mask vs echo overlapped (data not shown), suggesting that their slopes were not significantly different). This is not surprising, as the circumferential change-of-length of the subendo- and subepicardium of the LV is expected to be a result of a combination of actual shortening of the LV both circumferentially and longitudinally, which both echo and PC-CMR would account for while the masks would not. Also, the blood volume in the myocardium itself varies throughout the cardiac cycle, contributing to the change in in-slice area of the short-axis LV images, thus not to be attributed to the actual deformation of the cardiomyocytes.

Inter- and intrastudy variability

We found that both intra- and interstudy variability were low, the latter being comparable to previously reported values for human myocardial PC-CMR [39,40]. A source

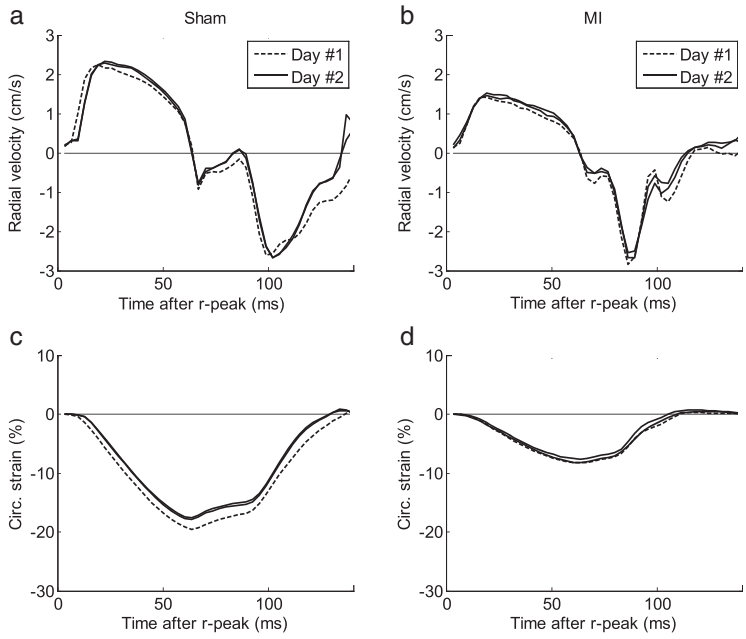

Figure 5 Inter- and intrastudy variability. Inter- and intrastudy variability in two animals (one post-MI and one sham) are shown, illustrating the correspondence between velocity waveforms and magnitude **(a**,**b)**, and *Sc* **(c**,**d)**. All slices consisted of two rotations, and for intrastudy analysis the two individual acquisitions of the two slices were interleaved, attempting to reduce any physiological effects of different time spent under anesthesia.

of variation in our data is suspected to be instability of animal physiology, as the data sets were acquired at different times after induction of anesthesia. Although all datasets were temporally normalized to account for varying lengths of the cardiac cycle, the actual velocities and peak *Sc* are not independent on heart rate and thus remain uncorrected.

Limitations

Geometrically systematic artifacts as they appear in this study, along with the rotating FOV approach, only apply to Cartesian imaging.

The choice to cover more than one r-r-interval doubles the scanning time since only every second r-peak was used as trigger point. However, this allowed complete coverage of the diastolic phase in combination with black-blood preparation, and improved the reliability of the triggering by allowing decay of currents in the ECG wires. Although the acquisition time per slice in our study was quite long, it is comparable to previous reports on MR-based strain assessment [29,30]. Compared to echocardiography, the MR examination is considerably more time-consuming. Depending on study design and needs, the trade-off between data yield and acquisition time must be considered.

Although beyond the scope of this study, a direct comparison of PC-CMR-derived strain with MR tagging should be considered, the latter usually being considered as the reference standard for measurement of myocardial strain. While our study validated global strain measurements, future studies should also address comparison of evaluation of regional strain from different methods.

The algorithm for calculating circumferential strain from myocardial trajectories in this paper (Eq. 1) is rather simple compared to more complex approaches, such as spline-based deformation analysis [41]. However, the presented results suggest that our approach is appropriate, yielding accurate and reproducible results.

Since slice selection was done in the laboratory system and the heart moves longitudinally during contraction, slightly different parts of the myocardium may be imaged in different time points throughout the cardiac cycle. This motivated the choice of including end-systole as a temporal origin for estimating tissue trajectories. Compared to conventional forward-backward motion tracking, intra- and interstudy limits-of-agreements were reduced using this extension (Table 3). However, to accurately capture complex three-directional motion and thus true 3D strain, volumetric data is required [42], and should be addressed by future studies. Volumetric PC-CMR might be achieved by embedding velocity encoding gradients into conventional or accelerated 3D imaging protocols, and has been demonstrated to allow comprehensive evaluation of both blood flow and myocardial motion in humans [43-45], but not, to our knowledge, in small animals.

Conclusion

In this study, we have presented an optimized PC-CMR protocol allowing assessment of the motion of the myocardium in rats with high detail, and provided a robust method for calculation of regional circumferential strain from the velocity data. By combining optimized slice planning, acquisition parameters and post-processing, exploration of the complex spatiotemporal pattern of *in vivo* motion and circumferential strain in the healthy and dysfunctional rat heart is feasible. We present, to our knowledge, the first study in small animals using PC-CMR to calculate strain.

Abbreviations

2D-STE: Two-dimensional speckle tracking echocardiography; DENSE: Displacement encoded imaging with stimulated echoes; FOV: Field-of-view; LV: Left ventricle; MI: Myocardial infarction; PC-CMR: Phase contrast cardiovascular magnetic resonance; Sc: Circumferential strain; SENC: Strain-encoded CMR.

Competing interests

The authors declare that they have no competing interests.

Authors' contributions

EKSE was involved in designing the study, collected, analyzed and interpreted CMR data, analyzed and interpreted echocardiography data and drafted the manuscript; JMA was involved in designing the study, provided and performed surgery on experimental animals, collected, analyzed and interpreted echocardiography data and provided critical review of the manuscript; KS and LZ were involved in designing the study, assisted in collection of CMR data, interpreted CMR data and provided critical review of the manuscript; JES was involved in designing the study, interpreted CMR data, and provided critical review of the manuscript; IS conceived and designed the study, collected, analyzed and interpreted echocardiography data, interpreted CMR data, and provided critical review of the manuscript. All authors have read and approved the final manuscript.

Acknowledgements

This work was supported by the South-Eastern Norway Regional Health Authority, Anders Jahre's fund for the Promotion of Science and Familien Blix' Fond Til Fremme Av Medisinsk Forskning. JES is a Senior British Heart Foundation Basic Science Research Fellow.

Author details

[1]Institute for Experimental Medical Research, Oslo University Hospital and University of Oslo, Kirkeveien 166, N-0407 Oslo, Norway. [2]KG Jebsen Cardiac Research Center and Center for Heart Failure Research, University of Oslo, Oslo, Norway. [3]Bjørknes College, Oslo, Norway. [4]Department of Cardiovascular Medicine, University of Oxford, Oxford, UK.

Received: 21 May 2013 Accepted: 3 September 2013
Published: 14 September 2013

References

1. Shehata ML, Cheng S, Osman NF, Bluemke DA, Lima JA. **Myocardial tissue tagging with cardiovascular magnetic resonance.** *J Cardiovasc Magn Reson.* 2009; **11:**55.
2. Osman NF, Sampath S, Atalar E, Prince JL. **Imaging longitudinal cardiac strain on short-axis images using strain-encoded MRI.** *Magn Reson Med.* 2001; **46:**324–34.
3. Aletras AH, Ding S, Balaban RS, Wen H. **DENSE: displacement encoding with stimulated echoes in cardiac functional MRI.** *J Magn Reson.* 1999; **137:**247–52.
4. Arai AE, Gaither CC III, Epstein FH, Balaban RS, Wolff SD. **Myocardial velocity gradient imaging by phase contrast MRI with application to regional function in myocardial ischemia.** *Magn Reson Med.* 1999; **42:**98–109.

5. Dall'armellina E, Jung BA, Lygate CA, Neubauer S, Markl M, Schneider JE. **Improved method for quantification of regional cardiac function in mice using phase-contrast MRI.** *Magn Reson Med.* 2012; **67:**541–51.
6. Zhu Y, Drangova M, Pelc NJ. **Fourier tracking of myocardial motion using cine-PC data.** *Magn Reson Med.* 1996; **35:**471–80.
7. Delfino JG, Fornwalt BK, Eisner RL, Leon AR, Oshinski JN. **Determination of transmural, endocardial, and epicardial radial strain and strain rate from phase contrast MR velocity data.** *J Magn Reson Imaging.* 2008; **27:**522–8.
8. Zhu Y, Drangova M, Pelc NJ. **Estimation of deformation gradient and strain from cine-PC velocity data.** *IEEE Trans Med Imaging.* 1997; **16:**840–51.
9. Herold V, Morchel P, Faber C, Rommel E, Haase A, Jakob PM. **In vivo quantitative three-dimensional motion mapping of the murine myocardium with PC-MRI at 17.6 T.** *Magn Reson Med.* 2006; **55:**1058–64.
10. Pelc NJ, Bernstein MA, Shimakawa A, Glover GH. **Encoding strategies for three-direction phase-contrast MR imaging of flow.** *J Magn Reson Imaging.* 1991; **1:**405–13.
11. Johnson KM, Markl M. **Improved SNR in phase contrast velocimetry with five-point balanced flow encoding.** *Magn Reson Med.* 2010; **63:**349–55.
12. Bernstein MA, Zhou XJ, Polzin JA, King KF, Ganin A, Pelc NJ, Glover GH. **Concomitant gradient terms in phase contrast MR: analysis and correction.** *Magn Reson Med.* 1998; **39:**300–8.
13. Walker PG, Cranney GB, Scheidegger MB, Waseleski G, Pohost GM, Yoganathan AP. **Semiautomated method for noise reduction and background phase error correction in MR phase velocity data.** *J Magn Reson Imaging.* 1993; **3:**521–30.
14. Rolf MP, Hofman MB, Gatehouse PD, Markenroth-Bloch K, Heymans MW, Ebbers T, Graves MJ, Totman JJ, Werner B, van Rossum AC, et al. **Sequence optimization to reduce velocity offsets in cardiovascular magnetic resonance volume flow quantification–a multi-vendor study.** *J Cardiovasc Magn Reson.* 2011; **13:**18.
15. Espe EK, Aronsen JM, Skrbic B, Skulberg VM, Schneider JE, Sejersted OM, Zhang L, Sjaastad I. **Improved MR phase-contrast velocimetry using a novel nine-point balanced motion-encoding scheme with increased robustness to eddy current effects.** *Magn Reson Med.* 2013; **69:**48–61.
16. Lingamneni A, Hardy PA, Powell KA, Pelc NJ, White RD. **Validation of cine phase-contrast MR imaging for motion analysis.** *J Magn Reson Imaging.* 1995; **5:**331–8.
17. McVeigh ER. **MRI of myocardial function: motion tracking techniques.** *Magn Reson Imaging.* 1996; **14:**137–50.
18. Sjaastad I, Sejersted OM, Ilebekk A, Bjornerheim R. **Echocardiographic criteria for detection of postinfarction congestive heart failure in rats.** *J Appl Physiol.* 2000; **89:**1445–54.
19. Bauer M, Cheng S, Jain M, Ngoy S, Theodoropoulos C, Trujillo A, Lin FC, Liao R. **Echocardiographic speckle-tracking based strain imaging for rapid cardiovascular phenotyping in mice.** *Circ Res.* 2011; **108:**908–16.
20. Hamilton CA, Jordan JH, Kraft RA, Hundley WG. **Noninterleaved velocity encodings for improved temporal and spatial resolution in phase-contrast magnetic resonance imaging.** *J Comput Assist Tomogr.* 2010; **34:**570–4.
21. Schneider JE, Wiesmann F, Lygate CA, Neubauer S. **How to perform an accurate assessment of cardiac function in mice using high-resolution magnetic resonance imaging.** *J Cardiovasc Magn Reson.* 2006; **8:**693–701.
22. Bernstein MA, Grgic M, Brosnan TJ, Pelc NJ. **Reconstructions of phase contrast, phased array multicoil data.** *Magn Reson Med.* 1994; **32:**330–4.
23. Pelc NJ, Drangova M, Pelc LR, Zhu Y, Noll DC, Bowman BS, Herfkens RJ. **Tracking of cyclic motion with phase-contrast cine MR velocity data.** *J Magn Reson Imaging.* 1995; **5:**339–45.
24. Simpson RM, Keegan J, Firmin DN. **MR assessment of regional myocardial mechanics.** *J Magn Reson Imaging.* 2012; **37(3):**576–99.
25. Markl M, Schneider B, Hennig J. **Fast phase contrast cardiac magnetic resonance imaging: improved assessment and analysis of left ventricular wall motion.** *J Magn Reson Imaging.* 2002; **15:**642–53.
26. Delfino JG, Fornwalt BK, Eisner RL, Leon AR, Oshinski JN. **Cross-correlation delay to quantify myocardial dyssynchrony from phase contrast magnetic resonance (PCMR) velocity data.** *J Magn Reson Imaging.* 2008; **28:**1086–91.
27. Jung B, Foll D, Bottler P, Petersen S, Hennig J, Markl M. **Detailed analysis of myocardial motion in volunteers and patients using high-temporal-resolution MR tissue phase mapping.** *J Magn Reson Imaging.* 2006; **24:**1033–9.
28. Liu W, Ashford MW, Chen J, Watkins MP, Williams TA, Wickline SA, Yu X. **MR tagging demonstrates quantitative differences in regional ventricular wall motion in mice, rats, and men.** *Am J Physiol Heart Circ Physiol.* 2006; **291:**H2515–21.
29. Liu W, Chen J, Ji S, Allen JS, Bayly PV, Wickline SA, Yu X. **Harmonic phase MR tagging for direct quantification of Lagrangian strain in rat hearts after myocardial infarction.** *Magn Reson Med.* 2004; **52:**1282–90.
30. Gilson WD, Yang Z, French BA, Epstein FH. **Complementary displacement-encoded MRI for contrast-enhanced infarct detection and quantification of myocardial function in mice.** *Magn Reson Med.* 2004; **51:**744–52.
31. Popovic ZB, Benejam C, Bian J, Mal N, Drinko J, Lee K, Forudi F, Reeg R, Greenberg NL, Thomas JD, et al. **Speckle-tracking echocardiography correctly identifies segmental left ventricular dysfunction induced by scarring in a rat model of myocardial infarction.** *Am J Physiol Heart Circ Physiol.* 2007; **292:**H2809–16.
32. Daire JL, Jacob JP, Hyacinthe JN, Croisille P, Montet-Abou K, Richter S, Botsikas D, Lepetit-Coiffe M, Morel D, Vallee JP. **Cine and tagged cardiovascular magnetic resonance imaging in normal rat at 1.5 T: a rest and stress study.** *J Cardiovasc Magn Reson.* 2008; **10:**48.
33. Hyacinthe JN, Ivancevic MK, Daire JL, Vallee JP. **Feasibility of complementary spatial modulation of magnetization tagging in the rat heart after manganese injection.** *NMR Biomed.* 2008; **21:**15–21.
34. Drangova M, Zhu Y, Bowman B, Pelc NJ. **In vitro verification of myocardial motion tracking from phase-contrast velocity data.** *Magn Reson Imaging.* 1998; **16:**863–70.
35. Masood S, Gao J, Yang GZ. **Virtual tagging: numerical considerations and phantom validation.** *IEEE Trans Med Imaging.* 2002; **21:**1123–31.
36. Biswas M, Sudhakar S, Nanda NC, Buckberg G, Pradhan M, Roomi AU, Gorissen W, Houle H. **Two- and three-dimensional speckle tracking echocardiography: clinical applications and future directions.** *Echocardiography.* 2013; **30:**88–105.
37. Li Y, Garson CD, Xu Y, Beyers RJ, Epstein FH, French BA, Hossack JA. **Quantification and MRI validation of regional contractile dysfunction in mice post myocardial infarction using high resolution ultrasound.** *Ultrasound Med Biol.* 2007; **33:**894–904.
38. Azam S, Desjardins CL, Schluchter M, Liner A, Stelzer JE, Yu X, Hoit BD. **Comparison of velocity vector imaging echocardiography with magnetic resonance imaging in mouse models of cardiomyopathy.** *Circ Cardiovasc Imaging.* 2012; **5:**776–81.
39. Petersen SE, Jung BA, Wiesmann F, Selvanayagam JB, Francis JM, Hennig J, Neubauer S, Robson MD. **Myocardial tissue phase mapping with cine phase-contrast mr imaging: regional wall motion analysis in healthy volunteers.** *Radiology.* 2006; **238:**816–26.
40. Simpson R, Keegan J, Firmin D. **Efficient and reproducible high resolution spiral myocardial phase velocity mapping of the entire cardiac cycle.** *J Cardiovasc Magn Reson.* 2013; **15:**34.
41. Bergvall E, Hedstrom E, Bloch KM, Arheden H, Sparr G. **Spline-based cardiac motion tracking using velocity-encoded magnetic resonance imaging.** *IEEE Trans Med Imaging.* 2008; **27:**1045–53.
42. Zhu Y, Pelc NJ. **Three-dimensional motion tracking with volumetric phase contrast MR velocity imaging.** *J Magn Reson Imaging.* 1999; **9:**111–8.
43. Wigstrom L, Sjoqvist L, Wranne B. **Temporally resolved 3D phase-contrast imaging.** *Magn Reson Med.* 1996; **36:**800–3.
44. Johnson KM, Lum DP, Turski PA, Block WF, Mistretta CA, Wieben O. **Improved 3D phase contrast MRI with off-resonance corrected dual echo VIPR.** *Magn Reson Med.* 2008; **60:**1329–36.
45. Kvitting JP, Ebbers T, Engvall J, Sutherland GR, Wranne B, Wigstrom L. **Three-directional myocardial motion assessed using 3D phase contrast MRI.** *J Cardiovasc Magn Reson.* 2004; **6:**627–36.

doi:10.1186/1532-429X-15-82
Cite this article as: Espe *et al.*: Novel insight into the detailed myocardial motion and deformation of the rodent heart using high-resolution phase contrast cardiovascular magnetic resonance. *Journal of Cardiovascular Magnetic Resonance* 2013 **15**:82.

IV